Modeling of Solar Cell Efficiency Improvement Using Optical Gratings and Intermediate Absorption Band

by

Albert S. Lin

A dissertation submitted in partial fulfillment
of the requirements for the degree of
Doctor of Philosophy
(Electrical Engineering)
in The University of Michigan
2010

Doctoral Committee:

Associate Professor Jamie D. Phillips, Chair

Professor Rachel S. Goldman

Professor Jasprit Singh

Assistant Professor Pei-Cheng Ku

Table of Contents

List of Figures

List of Tables

Abstract

This dissertation is a summary of the research effort for the theoretical study, modeling, design, and optimization of solid state photovoltaic devices. Efficiency improvements may be gained in solar cells through engineering of optical properties and electronic structure of materials. The first part of the dissertation is focused on the optimization of metal back reflectors of thin-film solar cells. The light trapping property of thin-film solar cell is improved through optical modeling and a randomized back reflector structures is proposed for broad band solar spectrum application. The second part of the dissertation is the theoretical study of intermediate band solar cells where the conversion efficiency is improved through the insertion of intermediate energy band in the fundamental energy gap. The theoretical aspect of intermediate band photovoltaic devices is investigated and the predicted high efficiency is confirmed by drift-diffusion modeling. A practical way to spectrally decoupling absorption spectrum is proposed, and the practicability of intermediate band concept is assessed and compared to experimental work.

The effect of grating structures on the back reflector is studied using electromagnetic modeling and an optimized structure is proposed to enhance the optical absorbance of these devices. The specific thin film solar cell studied is based on an amorphous silicon structure, though qualitative findings are applicable to any thin film solar cell technology. The goal is to find an optimal diffraction grating structure that is capable of exceeding solar cell efficiency for 1-D periodic grating couplers. A genetic algorithm (GA) is employed for this purpose. Solar cells with optimized arbitrarily shaped gratings exhibit a 29% improvement over planar cells and 9.0% improvement over the optimal cell with periodic gratings.

A new model incorporating carrier transport and recombination is proposed and simulation result shows the significance of this model in the modeling of intermediate

band solar cell. The material ZnTeO is used as a numerical example for the intermediate band solar cell model. The optimal impurity concentration is determined to be 10^{18} cm^{-3} for an optical absorption cross section of 10^{-14} cm^2. The conversion efficiency of a ZnTe solar cell with a total recombination lifetime of 10 ns is calculated to increase from 14.39 % to 26.87 % with the incorporation of oxygen. A spectrally decoupled scheme for subbandgap photovolatics is proposed in which, device structures with non-uniform occupation of intermediate electronic states are employed to reduce the dependence of conversion efficiency on spectral overlap. Solar cell conversion efficiencies are calculated for structures where absorption bands are spatially decoupled due to defined occupation of intermediate states. The spectrally-decoupled device provides a means to achieve high theoretical efficiency independent of spectral overlap that approaches the detailed balance efficiency limit of 63.2 % for intermediate state devices without spectral overlap. Fully coupled solution to partial differential equations provides insight into the operation of intermediate band solar cell. A doping compensation scheme is proposed to mitigate the space charge effects, and the device achieves conversion efficiencies of approximately 40%, similar to the maximum expected values from prior 0-D models. The analysis of experimental work using the model developed for intermediate band solar cell is conducted and ZnTeO alloy is chosen to be the material for intermediate band solar cell, where oxygen states are served as intermediate sites in the fundamental bandgap.

Chapter I Introduction

1.1 The Importance of Solar Energy

As greenhouse effect becomes more and more pronounced and fossil fuel resource will reach its limit in near future, the need for clean alternative energy emerges as an urgent issue in recent years. Utilization of solar energy has been one of the potential candidates for this, and is a technology that has been developed for many years. The use of solar photons to generate energy is undoubtedly a clean process, having minimal impact on the environment and ecology.

1.2 Photovoltaic Effect and Its Limitation

The photovoltaic effect is the phenomenon of generating electrical potential difference by light. The incident photons induce the transition of electrons from lower energy to higher energy states, and thus separate electron and hole quasi-Fermi levels. In the practical design of solar cells, the electric field in the depletion region of a p-n junction diode is utilized to separate excited electron-hole pairs, which are then collected by ohmic contacts.

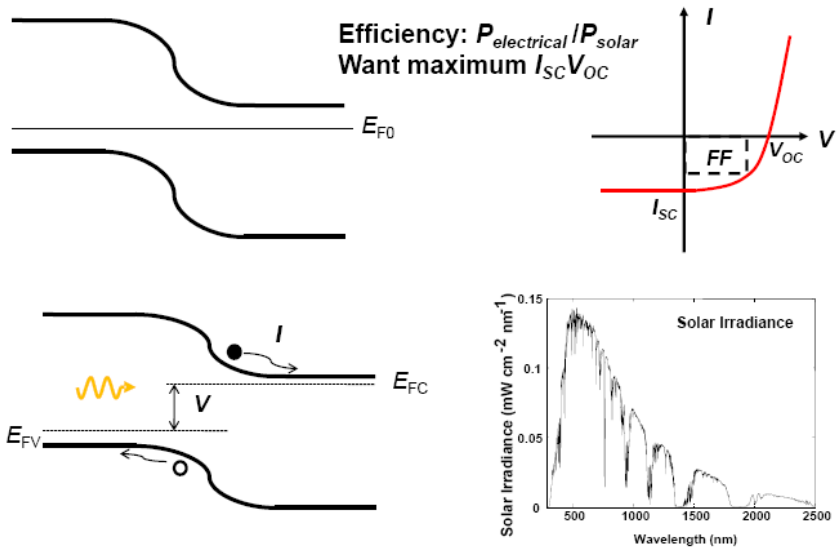

Figure 1.1 illustration of photovoltaic effect

The bandgap of semiconductor is an important consideration for solar cells, where large bandgap material is preferred for higher open circuit voltage, due to less recombination and higher potential barrier, while small bandgap material is preferred for higher short circuit current, due to more absorption. There is clearly a tradeoff where the optimal bandgap is near 1.1 eV [1]. For a given semiconductor, increasing optical absorbance is another consideration since it is related to the short circuit current. In practice, a thicker active region is preferred for higher optical absorbance, although this is accompanied by lower charge collection efficiency and elevated cost.

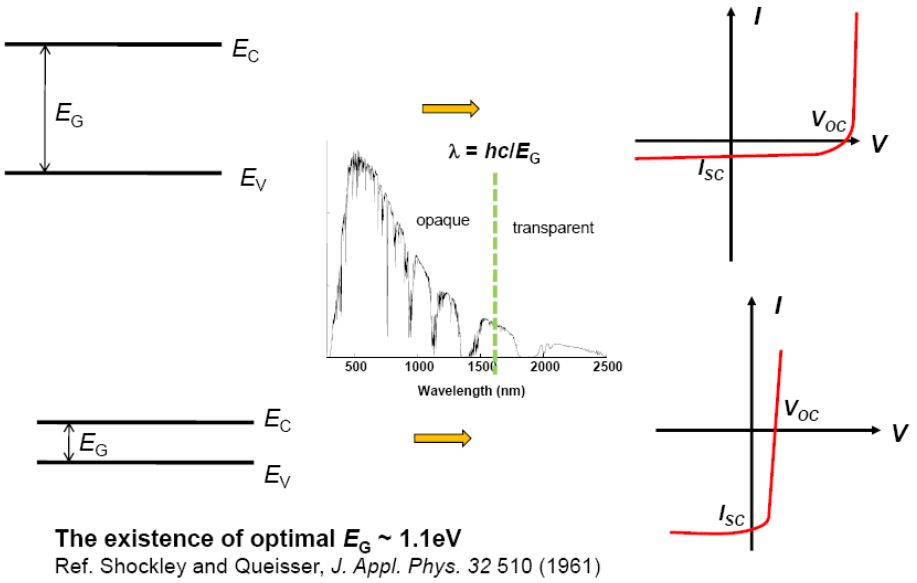

Figure 1.2 Illustration of the tradeoff between open circuit voltage and short circuit current and the existence of Shockley and Queisser limit.

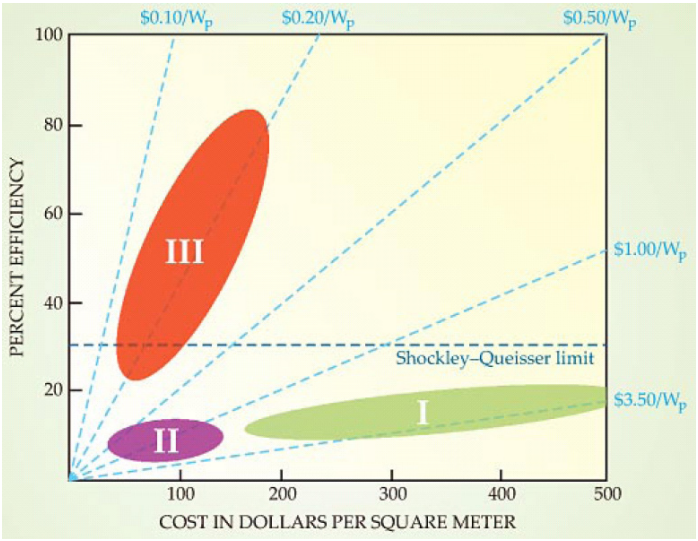

Figure 1.3 Solar cell efficiency vs. cost. M.A Green, *Progress in Photovoltaics* **9**, 123 (2000) [2]

Figure 1.3 illustrates the solar cell efficiency vs. cost. First generation cells generally consume more materials and thus are higher cost devices. Second generation thin film technology reduces the cost by using thin-film structures but light trapping is important especially for long wavelength photons. In chapter 2, the efficiency for thin-film cells is

increased by properly designed back reflectors. Third generation cells increase the efficiency by eliminating thermalization loss with multiple transitions or energy gaps and thus can be more cost-effective technology. In chapter 3-6, the theoretical aspects of intermediate band solar cells are examined and its practicability is assessed. Traditionally, bulk crystalline silicon solar cells dominate solar energy technology and single crystalline silicon wafers are used to fabricate devices which can achieve conversion efficiency around 20 %. The fundamental problem with this kind of device is electron (and hole) thermalization in which high energy photons dissipate excess energy as heat. Materials with large bandgap alleviate this phenomenon but also lead to lower short circuit current due to no absorption below the fundamental bandgap. Tandem cells are proposed as a solution. In this scenario, two or more junctions with different bandgaps are connected in series as in Figure 1.5 and light incident from the larger bandgap side of the device. Common material systems include silicon/germanium and III-V semiconductors. Recently, II-VI semiconductors have also attracted significant attention. The currently achieved highest efficiency is around 40% [3]. Nonetheless, the fabrication process is complex for multi-junction cells and current matching between different subcells has to be ensured in order to achieve high efficiency. In the more advanced form/next generation of tandem cell, states are inserted into the bandgap of the materials, where a single junction device may provide a broadband absorption spectrum while maintaining a large open circuit voltage. This is the concept of the intermediate band solar cell. It is promising in the aspect that it avoids the complicated design and fabrication process of multi-junction cells and can potentially achieve even higher efficiency.

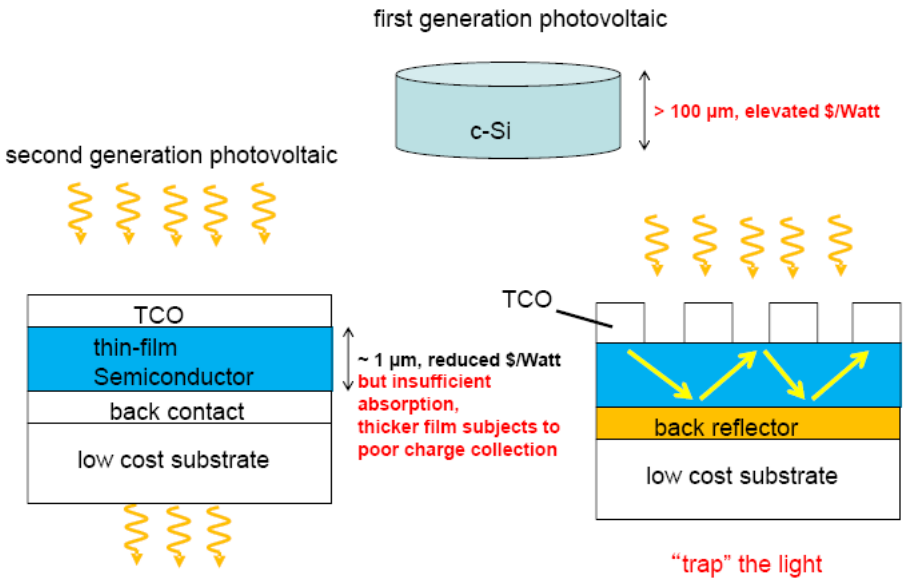

Figure 1.4 Illustration of thin-film solar cell and the need of light trapping

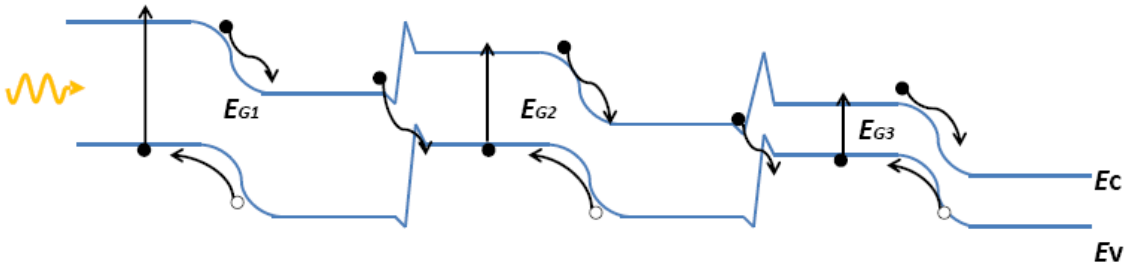

Figure 1.5 Illustration of a multi-junction cell

To date, crystalline silicon solar cells have demonstrated efficiency near 25%. Notice that the silicon bandgap is close to optimal value of single junction conventional photovoltaic cell. GaAs based devices can achieve efficiency around 26%. The bandgap of GaAs is not optimal, though the higher mobility and longer recombination lifetime provides an advantage over silicon technology. The multi-junction cell base on III-V materials can achieve efficiency near 32%. Nevertheless, this kind of device is expensive and thus limited to space application. For low cost and large area, terrestrial application, thin-film amorphous/nano-cystalline silicon cell can be promising and currently achieve efficiency around 10%. Nonetheless, device degradation is still a concern. Thin-film CIGS or CdTe cell have emerged in recent year and can achieve efficiency as high as

20%, though cadmium and its compounds are carcinogens. While tremendous amount of effort is spent on the technology side of conventional devices, it is clear that the third-generation photovoltaics are an important subject since it boosts the efficiency, and reduces the cost of power generation [4].

1.3 Efficiency Enhancement Techniques: Optical Aspect

Solar cells based on single crystal silicon or epitaxial III-V compound semiconductors continue to provide the highest conversion efficiency. However, single crystal solar cells and associated concentrator cells are still higher in cost than desired for generalized commercial use. Thin-film solar cells provide a lower cost alternative to bulk and epitaxial single-crystalline solar cells[5]. Several thin film materials are currently under extensive study including copper indium gallium selenide (CIGS), CdTe, organic materials, amorphous silicon, microcrystalline silicon, and thin film silicon alloys [6]. The minority carrier diffusion lengths are generally small in these polycrystalline or amorphous thin films, requiring thin layers to maximize charge collection efficiency. The requirement for thin layers for maximum charge collection efficiency, however, is contradictory for the requirement to maximize solar energy absorption. Optical absorption in thin films is particularly small at longer wavelengths near the bandedge of the thin film material, where the absorption coefficient is low. As a result, the optical design or equivalently, increasing solar cell's light trapping capability is very important. Randomly textured surfaces have been used and investigated for both bulk crystalline and thin-film solar cell for many years [7-13]. These randomly textured surfaces are generally achieved through specialized etching techniques, where light can be reflected and "trapped" in a thin film structure by total internal reflection. Small pyramid structures have also been used on the front side of silicon solar cells in order to increase solar transmission and light trapping [14, 15]. Lithographically defined 1-D periodic gratings have also been investigated [7, 16-19] as an alternative to randomly textured surfaces. The randomly textured back reflector, however, typically shows superior performance experimentally when compared to lithographically defined gratings. The typical superiority of random gratings is generally attributable to the diffractive characteristics of light and the need to optimize the optical design across the broad solar spectrum. Despite

many past research efforts on thin film solar cells, the question may still be asked: what is the optimal design for light coupling and trapping in thin film solar cells? In the effort to work towards an answer to this important question, detailed studies of the optical characteristics and optimization of reflectors for thin film solar cells are described in this work.

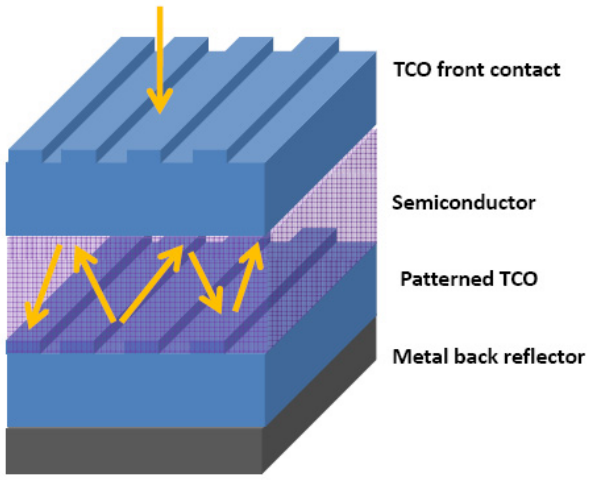

Figure 1.6 The concept of light trapping

1.4 Efficiency Enhancement Techniques: Intermediate Band Concept

Single-junction photovoltaic solar cells have demonstrated the ability to achieve power conversion efficiency values near the maximum theoretical limit [1, 4]. However, the maximum power conversion limitation for single-junction solar cells is lower than desired, due to energy loss for solar photons with energy exceeding the bandgap energy and absence of solar cell response to solar photons with energy below the bandgap energy. Power conversion efficiency has been improved for tandem and multi-junction solar cells, but these devices are more complex and are accompanied by higher manufacturing costs. In recent years, intermediate-band solar cells (IBSC) have been proposed to exceed efficiency limitations of conventional single-junction cells [1, 20]. In these devices, electron states are introduced in the forbidden bandgap of a conventional semiconductor to provide three optical absorption bands to respond to incident solar energy. Previous calculations have suggested a theoretical 63.2% efficiency limitation[20] for single-junction intermediate band solar cells, motivating experimental efforts to realize these

promising photovoltaic devices. Several approaches have been proposed to practically realize an intermediate band solar cell (IBSC), including quantum dots [21-26], dopant impurities (often termed impurity-band photovoltaics) [27, 28], and dilute semiconductor alloys [29-38].

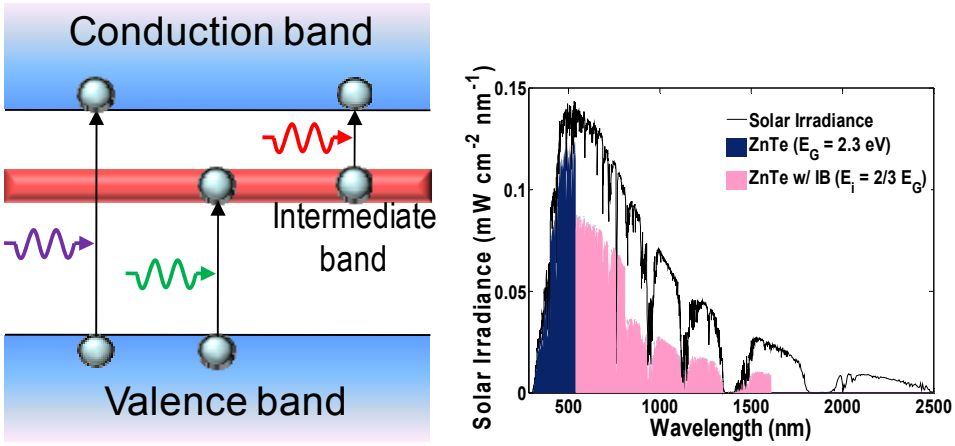

Figure 1.7 Illustration of the concept of intermediate band photovoltaics

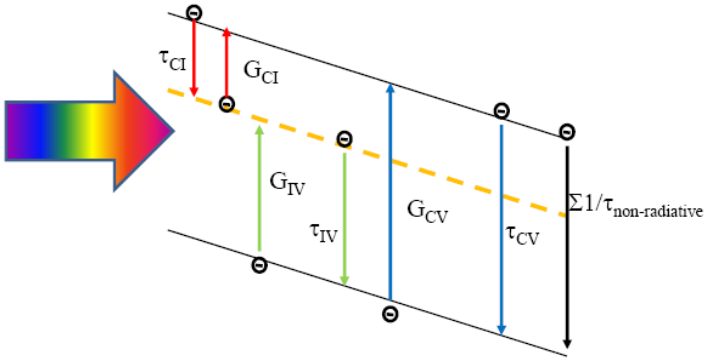

Figure 1.8 Illustration of intermediate band operation principle

1.5 Outline of the Dissertation

The first chapter is the introduction for the solar cell technology. Conventional technology and the current status of conversion efficiency achieved is described and compared. The concept of light trapping and intermediate band and their use and importance in the solar cell operation/technology is presented.

The second chapter is devoted to the electromagnetic modeling of photovoltaic devices. The effect of grating structure on the back reflector is studied and an optimization scheme and optimized structure is proposed to enhance the optical absorbance of these devices. Solar cells with optimized multi-level rectangular gratings exhibit a 23% improvement over planar cells and 3.8% improvement over the optimal cell with periodic gratings. Solar cells with optimized arbitrarily shaped gratings exhibit a 29% improvement over planar cells and 9.0% improvement over the optimal cell with periodic gratings. The third chapter is devoted to the 0-dimensional, semi-analytical modeling of intermediate band solar cell. The previous work of detailed balance efficiency limit is reviewed and studied. A new model incorporating carrier transport and recombination is proposed and simulation result shows the significance of this model in the modeling of intermediate band solar cell. The material ZnTeO (E_G = 2.3 eV, E_I = 1.8 eV) is used as a numerical example for the intermediate band solar cell model, where conversion efficiency drops from 30.36 % to 19.4 % for a 10 μm long device for a recombination lifetime decrease from 1μs to 5 ns. The optimal impurity concentration is determined to be 10^{18} cm^{-3} for an optical absorption cross section of 10^{-14} cm^2. The conversion efficiency of a ZnTe solar cell with a total recombination lifetime of 10 ns is calculated to increase from 14.39 % to 26.87 % with the incorporation of oxygen.

The fourth chapter is spectrally decoupled scheme for subbandgap photovolatics in which, device structures with non-uniform occupation of intermediate electronic states are proposed to reduce the dependence of conversion efficiency on spectral overlap. Solar cell conversion efficiencies are calculated for structures where absorption bands are spatially decoupled due to defined occupation of intermediate states. Conversion efficiencies for a two section and three section device with spectral overlap of 4 eV are determined to be 52.8 % and 61.5 %, respectively, and are significantly larger than the calculated efficiency of 35.1% for the case of a standard multi-photon cell with uniform half-filled intermediate states The spectrally-decoupled device provides a means to achieve high theoretical efficiency independent of spectral overlap that approaches the detailed balance efficiency limit of 63.2 % for intermediate state devices without spectral overlap and 63.8 % for unconstrained triple-junction tandem cells.

The fifth chapter is the drift-diffusion modeling of intermediate band solar cell. Fully coupled solution to partial differential equations provides insight into the operation of intermediate band solar cell. Physical phenomenon including carrier transport, generation, intermediate band filling, and radiative/non-radiative recombination are all explicitly modeled under the framework of drift-diffusion model. The band diagram of intermediate band device is first time presented here, and its implication on device operation is discussion. The model is applied to a prototypical solar cell device, where strong space-charge effects and reduced conversion efficiency are identified for the case of lightly-doped absorption regions. A doping compensation scheme is proposed to mitigate the space charge effects, with optimal doping corresponding to one-half the concentration of intermediate band states. The compensated doping device design provides calculated conversion efficiencies of approximately 40%, similar to the maximum expected values from prior 0-D models.

The sixth chapter is the analysis of experimental work using the model developed for intermediate band solar cell. The ZnTeO alloy is chosen to be the material for intermediate band solar cell, where oxygen states are served as intermediate sites in the fundamental bandgap and provide transitions in addition to conduction to valence band transitions. Absorption spectrum measurement shows significant sub-bandgap absorption with increased oxygen concentration. n-GaAs/p-ZnTeO diode is fabricated and spectral response shows enhanced long-wavelength response attributed to oxygen incorporation. The ZnTeO diode J-V under illumination shows higher short circuit current compared to ZnTe baseline devices. The theoretical calculation is conducted for both absorption spectrum and current voltage characteristics and result is compared to experiment data. Time-resolved photoluminescence measurements are used to infer carrier relaxation lifetimes, where time constants of > 1 μs and < 100 ps are measured for optical transitions at oxygen states and the conduction band, respectively. Rate equation analysis suggests excitation dependence for the lifetime of conduction band electrons, where an increase of carrier lifetime due to increased occupation of oxygen states is believed to be critical in achieving high conversion efficiency for solar cells based on multi-photon processes in these materials. In the last chapter, the direction for future research effort is pinpointed.

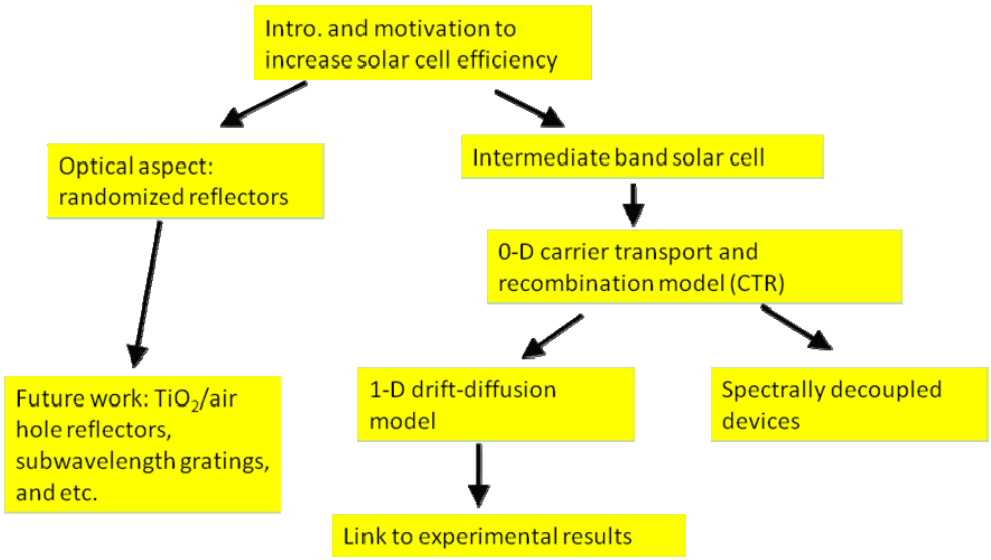

Figure 1.9 The flow of this dissertation

Chapter II Light Trapping in Thin Film Solar Cell

2.1 Introduction

Thin-film solar cells provide a lower cost alternative to bulk and epitaxial single-crystalline solar cells. Several thin film materials are currently under extensive study including copper indium gallium selenide (CIGS), CdTe, organic materials, amorphous silicon, microcrystalline silicon, and thin film silicon alloys. The minority carrier diffusion lengths are generally small in these polycrystalline or amorphous thin films, requiring thin layers to maximize charge collection efficiency. The requirement for thin layers for maximum charge collection efficiency, however, is contradictory for the requirement to maximize solar energy absorption. Optical absorption in thin films is particularly small at longer wavelengths near the bandedge of the thin film material, where the absorption coefficient is low. As a result, the optical design or equivalently, increasing solar cell's light trapping capability is very important.

The specific thin film solar cell studied is based on an amorphous silicon structure, though qualitative findings are applicable to any thin film solar cell technology. The goal is to find an optimal diffraction grating structure that is capable of exceeding solar cell efficiency for 1-D periodic grating couplers. A genetic algorithm (GA) is employed for this purpose. In this approach, two different structures are proposed: multi-level rectangular gratings and arbitrarily shaped diffraction gratings. The former is experimentally feasible since multi-levels can be achieved by separate lithography and etch steps. The latter is somewhat difficult to realize experimentally but it mimics a randomly textured surface, and would indicate the morphological characteristics desired for optimal solar cell efficiency.

2.2 Thin Film Solar Cell Structures and Optical Modeling

In order to study light trapping in thin film solar cells, the amorphous silicon thin-film solar cell structure is used as the prototype structure in this study. The baseline thin film solar cell structure consists of an amorphous silicon junction with top and bottom transparent ZnO contacts, and a back metallic reflector. The solar cell structure is shown in Figure 2.1 for the case of a flat cell and cell with a periodic grating. The amorphous silicon thickness is assumed to be 1 μm and conformal coverage is assumed for cells with periodic gratings. Material parameters used for a-Si and ZnO are taken from literature [39-42]. As a result, flat cells and cells with periodic gratings have the same amount of amorphous silicon material, and comparison of quantum efficiency reflects the light trapping capability of the structure. The ZnO front contact thickness is 100 nm and the thickness of the ZnO bottom layer varies with reflector geometry with groove height (h_g) ranging between 0 and 800 nm. The groove period (P) ranges from 0.5 μm to 5 μm. Two proposed structures are shown in Figure 2.6 with potential to exceed periodic rectangular gratings through optimization. The first structure is a multi-level rectangular grating, which represents an option that may be fabricated lithographically. In the multi-level rectangular grating, adjacent groove height may be changed and adjusted independently between predefined levels. The number of predefined levels is chosen to be four in our simulation to represent a reasonable number for fabrication. The arbitrarily shaped diffraction grating structure can essentially have any shape down to the spatial resolution in the simulation, which is 0.0125 μm in the lateral x-direction and 6.25 nm in the vertical y-direction. Higher resolution in the y-direction can be realized by specifying higher precision for the variables in GA, but this also requires more generations to locate the maxima

Solar cell efficiencies are calculated using finite element methods for Maxwell's equations using the software COMSOL. Solar radiation is assumed to be at normal incidence, where a scattering boundary condition is used for the top surface and perfect electric conductor boundary condition for the bottom metallic reflector. For left and right boundaries, periodic boundary conditions are applied. One period of gratings is therefore sufficient to represent infinitely many periods of gratings. For multi-level rectangular and

arbitrarily shaped gratings, a device length of 5 μm is assumed. The device length of 5 μm was chosen based on a series of simulations, where no apparent improvement was observed for larger devices lengths. The incident wave is assumed to have TE polarization, while TM or hybrid simulation can be easily implemented with same approach. Due to the assumption of TE polarization and two-dimensional device geometry, only one component of electric field needs to be solved, E_z. The electric field may be obtained by the solution of Helmholtz equation Eq. 2.1[43]

$$\nabla^2 E_z(\vec{r}) + \omega^2 \mu \varepsilon E_z(\vec{r}) = 0 \qquad 2.1$$

where μ, ε are the permeability and permittivity of the materials, respectively.

The time averaged power loss (or equivalently, absorbance) is Eq. 2.2 [44, 45]

$$Q_{av}(\vec{r}) = \frac{1}{2}\sigma\left|E_z(\vec{r})\right|^2 \qquad 2.2$$

and the quantum efficiency (*Q.E.*) for monochromatic light is calculated by

$$Q.E.(\lambda) = \frac{\int Q_{av}(\vec{r})d\vec{r}}{\vec{P}_{av,incident}} \qquad 2.3$$

where $P_{\text{av, incident}}$ is the time-averaged pointing vector of the monochromatic incident field. Eq. 2.3 is under the assumption that all of the photo-generated electron-hole pairs are collected by the electrodes and contribute electrical current. In other words, the carrier recombination time in amorphous silicon is assumed to be much longer than the transit time in the intrinsic region of p-i-n diode. The integrated quantum efficiency is then calculated by integrating over wavelength using [46, 47]

$$Int.QE = \frac{\int \frac{\lambda}{hc} S(\lambda) I(\lambda) d\lambda}{\int \frac{\lambda}{hc} I(\lambda) d\lambda} \qquad 2.4$$

where $S(\lambda)$ is the spectral response of the solar cell, which equals to $QE(\lambda)$, and $I(\lambda)$ is AM 1.5 solar spectrum [48]

2.3 Electromagnetic Modeling Numerical Approaches and Finite Element Method

Transfer or scattering matrix is the method based on matching the boundary condition for incoming and reflecting plane waves at different layers for a one dimensional structure. The scattering matrix in general has better numerical stability compared to the transfer matrix approach. While they are very easy to implement, their use may be limited to solving 1-D structures such as distributed Brag reflector (DBR). Effective index or other approximation may be applied to 2-D structures, though the result has to be verified with more accurate numerical methods.

The rigorous coupled wave approach is based on a series expansion and can solve two dimensional periodic structures. It has been applied to solve diffraction gratings of various shapes, polarizers, and reflectors. The truncated series is used as an approximation to the solution, and the trade off is made between the accuracy, convergence and computational complexity.

Finite difference time domain is a differential equation based numerical approach. Finite difference discretization is used to construct difference equations of Maxwell's equations. It is very suitable for transient problems, and even for harmonic steady state problems, where the transient solution is still computed, and the convergence is achieved when the error between the solution at the current instant of time and the solution at the previous instant of time becomes negligible. Practically, FDTD is easy to implement using C/C++ or Matlab. Nonetheless, the geometry might be limited to rectangular shaped structures. The grid has to be very dense, normally a tenth to twentieth of the wavelength in the dielectric materials, and grid spacing should be uniform or quasi-uniform in order to have accurate results.

The finite element method is in general more difficult to implement due to the complexity of the formulation and coding. The convergence is not as clear as the finite difference method. The advantage is that it is not restricted to rectangular structures, and triangular mesh can conform to irregular geometry.

Ray tracing techniques are widely used to estimate the enhancement of optical path length for solar cells. Nonetheless, the wave characteristics are lost and interference is not taken into account. While it provides insight into the optical path length inside the device to some extent, the dependence of response on wavelength may not be accurate. Wave optics is recently employed to investigate the optical property of solar cell structures since the diffraction of back reflectors is a complex phenomenon and requires full wave simulation. Potential techniques for EMW simulation include T-matrix or S-matrix, RCW, and beam propagation. Here we choose the most accurate and computational demanding ones, i.e., FDTD and FEM, to have the most accurate and reliable result. FDTD method is implemented with Sentaurus Device EMW and the FEM is implemented with Comsol Multiphysics RF module.

2.4 Design of Zno/Ag Back Reflector

2.4.1 Flat Cell and Periodic Gratings

It is illustrative to first compare the characteristics of planar solar cells and solar cells with periodic gratings. For periodic gratings, optical coupling and trapping will depend on the relationship of groove height and groove period, which will have strong optical interaction with specific wavelengths in the solar spectrum. The calculated QE for varying groove height and a fixed groove period of 1 μm are shown in Figure 2.2 for λ = 1000 nm. and λ = 400 nm. For the planar solar cell, the groove height equals the total bottom ZnO thickness in excess of 200 nm. In these plots, the planar cell shows impedance matching characteristics where periodic maxima and minima in QE correspond to optical interference in the structure. Clear resonant peaks are observed for cells with periodic gratings at λ = 1000 nm corresponding to the Bragg condition in the cell at this wavelength. The observation of strong resonance in the QE versus groove height is due to weak absorption in a-Si at this near infrared wavelength. At λ = 400 nm, cells with periodic gratings show significant performance improvement over flat cells for groove height exceeding ~100 nm. The enhancement of QE for cells with periodic gratings at λ=1000 nm can be qualitatively understood by the following argument. Incoming solar radiation will experience reflection at the solar cell surface, ZnO/a-Si

interfaces, and back reflector. For flat cells, light that is coupled into the cell, but not absorbed in the a-Si, will reflect from the backside and escape from the top surface. The periodic grating on the backside will diffract the light at an angle, with potential for multiple internal reflections, leading to a longer optical path length and increased probability for absorption. At shorter wavelengths, optical absorption is high, leading to rapid decay of the incoming wave, as illustrated in Figure 2.3. The enhancement observed at λ=400 nm for QE of cells with periodic gratings is then primarily related to improved transmission of the front side in solar cell structure. The grating structure on the top side therefore acts as an anti-reflection layer.

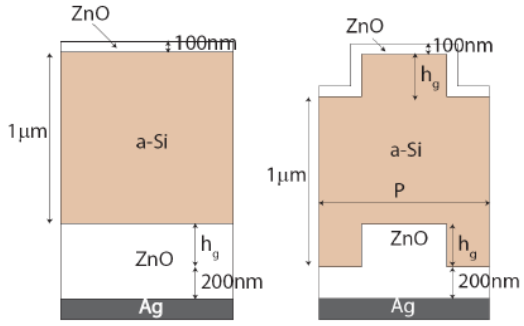

Figure 2.1 Device structures of flat cell and cell with periodic grating couplers. The cells with periodic grating couplers are of substrate type

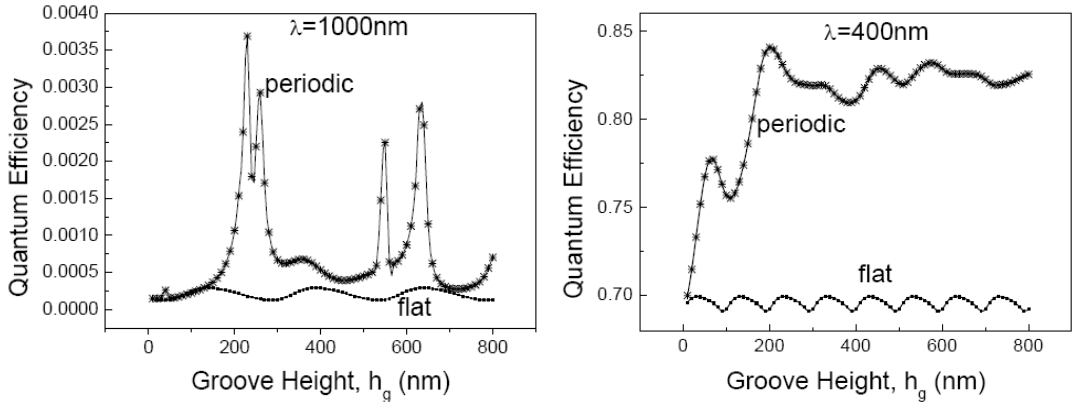

Figure 2.2 Quantum efficiency versus groove height for flat cells and cells with periodic grating couplersat λ=1000nm and 400nm.

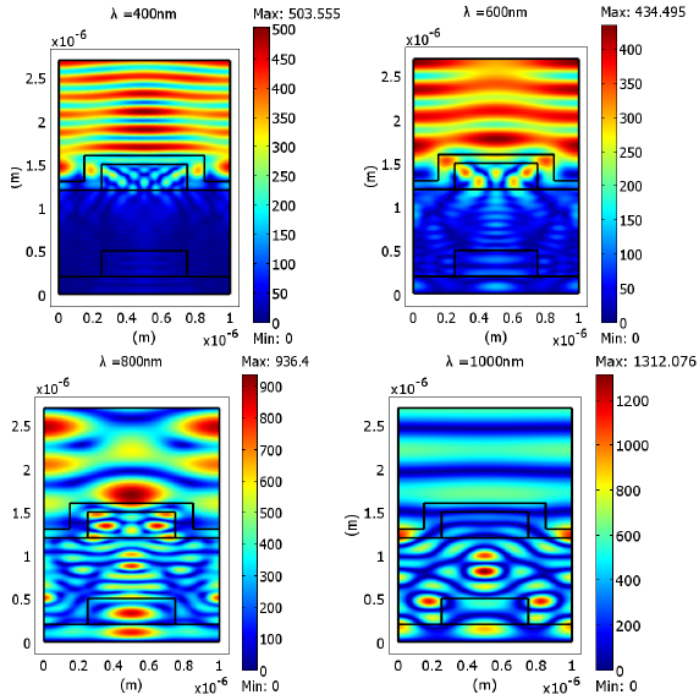

Figure 2.3 Electric field profile for cells with periodic grating couplers for λ=400 nm (upper left), λ=600 nm (upper right), λ=800 nm (lower left), and λ=1000 nm (lower right). hg=300 nm and P=1 um.

The comparison of solar cells with periodic gratings of varying groove height illustrates the complex dependence of QE on grating geometry. For shorter wavelength, QE is generally strong for groove height exceeding a particular value. For longer wavelengths, QE will be optimal for particular geometry at a particular wavelength due to resonant behavior. The resonant behavior, however, will not correspond to other wavelengths in the solar spectrum, and may not provide the optimal overall solar cell efficiency. Integrated quantum efficiency, therefore, should be calculated and used to assess and optimize periodic diffractive grating performance. The dependence of integrated QE on the groove height and groove period of solar cells with periodic gratings is plotted in Figure 2.4. From this plot, the optimal groove height and groove period are h_g=325 nm and P=1.4μm respectively, with an integrated QE of 0.579. This maximum integrated QE may then be defined as the optimal solar cell with a periodic grating, to be compared to random grating structures later. Qualitative dependencies of integrated QE on periodic grating geometry are discussed in the following. For groove periods that are

too large, there is insufficient interaction with the incoming radiation at short wavelengths, reducing the effectiveness of the grating to act as an anti-reflection layer. Similarly, groove periods that are too small (less than ~1 μm) result in decreased integrated QE, likely due to weak interaction between the electromagnetic wave and the small feature size. Similar to groove period, small groove height results in a decrease in integrated efficiency due to insufficient interaction with the optical wave. The integrated QE is relatively insensitive to groove height at larger dimensions. This insensitivity is related to the broad band nature of the solar spectrum, where a given groove height only results in resonant behavior for particular wavelengths.

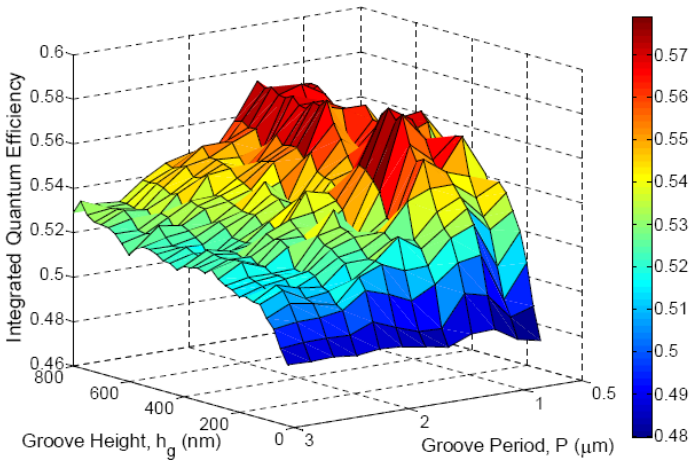

Figure 2.4 Integrated quantum efficiency versus groove period (P) and groove height (hg). AM 1.5 solar spectrum is assumed

2.4.2 Genetic Algorithm

A genetic algorithm (GA) or evolutionary algorithm is a stochastic global search method that mimics the metaphor of natural biological evolution [49]. The principle of survival of the fittest is applied to a population of individuals, which are potential solutions to the problem. Individuals with higher fitness in the problem domain have a better chance to be selected and to reproduce their own offspring. This results in individuals who are better suited to the environment tend to have more children and higher fitness as the evolution process proceeds, just as in natural adaptation. Genetic algorithms are particularly suited for search in very large or unbounded sample spaces, and it has been proven useful in many different fields [50-53]. In the case of light

coupling and trapping in solar cells, the complexity associated with the wave nature of light and broad solar spectrum results in a similarly large samples space for possible grating structures for optimization of solar cell efficiency.

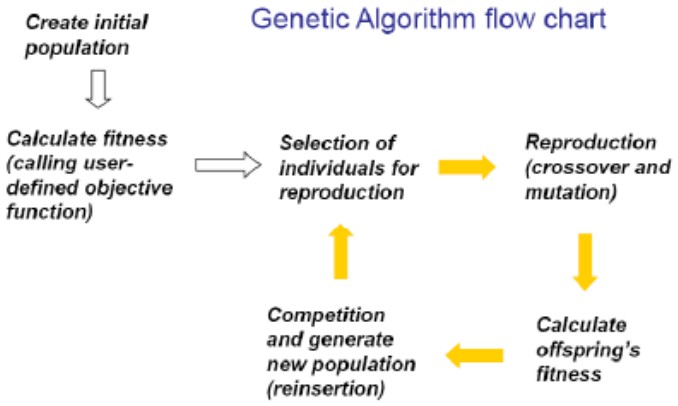

Figure 2.5 Genetic algorithm flow chart

The specifics of the GA employed in this study are detailed below. Binary coding is employed for chromosome representation, where randomly generated bit strings are used to initialize the population. Population size ranges from 10-50 individuals were used in this study. For selection, stochastic universal sampling (SUS) is employed, which is a single-phase sampling algorithm with minimum spread and zero bias. Instead of the single selection pointer employed in traditional methods (e.g. roulette wheel methods), SUS uses N equally spaced pointers, where N is the number of selections required. The population is shuffled randomly and a single random number, *ptr,* in the range [0 Sum/N] is generated, where *Sum* is the summation of all individuals' fitness value. The N individuals are then chosen by generating the N pointers spaced by [1, *ptr*, *ptr*+1, ... , *ptr*+N-1], and the individuals whose fitness span the positions of the pointers are selected. Single point crossover is used for recombination. Randomly determined position in the chromosome (binary bit strings) is set as the crossover point. The portion of the chromosome after the crossover point is substituted with the chromosome of the other parent, and thus two parents reproduce two new individuals. For mutation, each bit in the chromosome has small probability to change its parity, as mimics natural evolution. Finally, uniformly random reinsertion is used to form new populations. When deciding which members in the old population should be replaced by new individuals, the most

straightforward strategy will be replacing the least fit ones. Nonetheless, many other schemes are proposed and it has been shown there is not much difference in their convergence behavior. In addition, it is advocated that replacing the least fit individuals during reinsertion equivalently implements elitist strategy. Here, uniformly random scheme is used and thus the replacement of the old individuals in a population is determined randomly.

2.4.3 Genetic Algorithm Optimized Grating for Solar Cell Application

The definition of the device structure using the GA approach is described in the following, and illustrated in Figure 2.7. For a four-level rectangular grating, the variables in the GA are $h_g(i)$ and P. The variable $h_g(i)$, $i=1, 2, \ldots, 10$ is the groove height for each index point in the grating, and P is the groove width. Four-level grating can give larger searching space (or equivalently randomness) in the optimization process and thus higher efficiency can be achieved compared to two-level gratins. For arbitrarily shaped gratings, 401 vertices, $(x(i), y(i))$, $i=1,2, \ldots, 401$ are utilized to "draw" the device structure. The values for $x(i)=0, 0.0125\ \mu m, 0.025\ \mu m, \ldots, 5\ \mu m$ are fixed with a total device length of 5 μm. Although the vertices define the shape of the gratings, the slopes between vertices are used as the variables in the GA to define the shape of the structure. The values for the vertices are then given by $y(i) = y(i-1)+s(i-1)\Delta x$, where Δx=0.0125 μm is the x-spacing and $s(i)$ is the slope. Specifying the slope of the structure turns out to be an effective way to "draw" the device geometry since by limiting the slope, GA gives gradually changed profile, which is a more realistic picture of a randomly textured surface. The optimal shape may then be generated as the result of evolution. Diffraction gratings defined in this way can have virtually any shape within the resolution and slope limitation. Genetic algorithm is an excellent method for this kind of problem because of its ability to find maxima of irregularly behaved functions. Due to the fact that the optimal geometry cannot be known from simple analysis or analytical solutions and sweeping entire parameter space is computationally impossible, genetic algorithm have to be utilized to find local or even global maxima of objective function. Here the objective function is the efficiency of solar cells. Other techniques such as Fourier analysis may be applied afterward to analyze the optimized gratings.

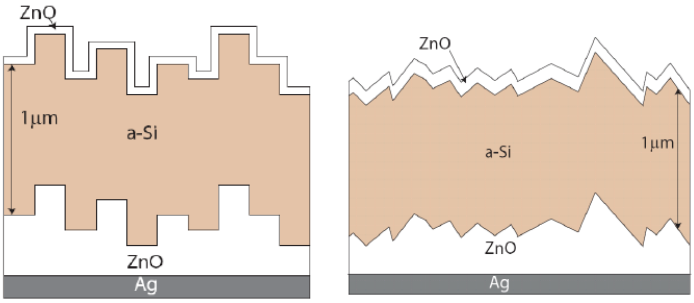

Figure 2.6 Device structures of multi-level rectangular gratings and arbitrarily shaped gratings.

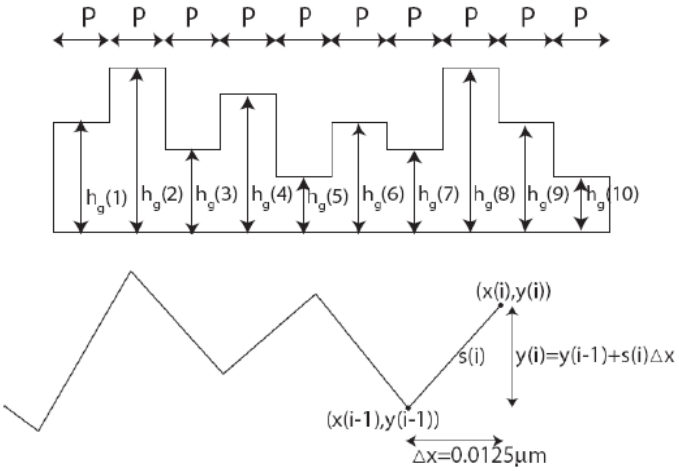

Figure 2.7 Illustration of the genetic algorithm scheme for multi-level rectangular gratings (top) and arbitrarily shaped gratings (bottom)

A random square grating may then be considered to improve integrated QE in comparison to a periodic grating. The advantage of a non-periodic geometry is that the diffractive behavior of a more randomized grating will be distributed over a wider range of the solar spectrum. The optimization of these structures cannot be performed directly as in the case of periodic structures, due to the much larger number of possible geometries. To further examine potential improvements over periodic gratings, a multi-level randomized rectangular grating is studied. The four level grating may be fabricated using three photolithography and etch steps. Rectangular gratings of more levels may be capable of providing even better performance due to a larger search space, but the four-level system is chosen for practicality. The groove height (or etch depth) was varied to

have four levels in the range of 0-800 nm, and groove width varying between 0.4 μm and 0.8 μm. These values were chosen to correspond to dimensions examined in the study of periodic gratings as shown in Figure 2.2. The statistics using the genetic algorithm methodology are shown in Figure 2.8 for one run, where the mean is the average of integrated quantum efficiency among all individuals of a certain generation. The mean shows an initial increase and then convergence to a maximum of the objective function. Standard deviation quantifies the diversity within a population, which should decrease since the fittest individuals tend to dominate in the evolution. The final structure obtained in one run is shown in Figure 2.8, with corresponding electric field profile at λ=1000nm and λ=400nm shown in Figure 2.9. The GA optimized four-level rectangular grating structure is capable of achieving integrated QE of 0.6010, in comparison to 0.5790 (3.8% improvement) for the optimal periodic grating and 0.4873 (23.3% improvement) for a planar solar cell.

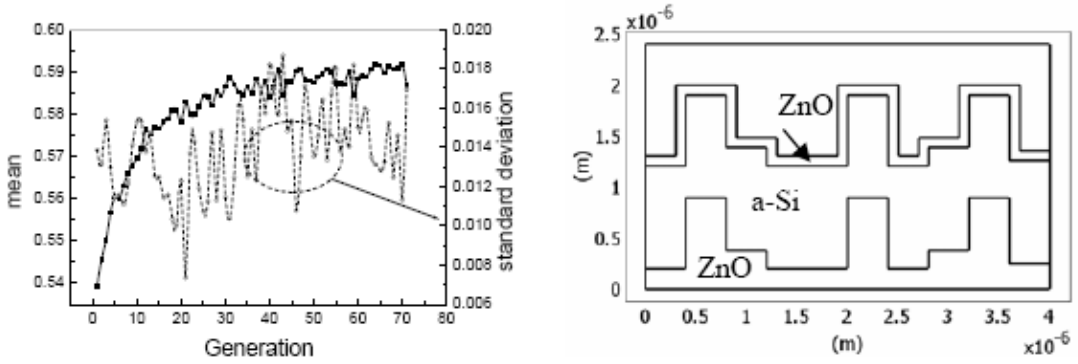

Figure 2.8 Genetic algorithm statistics (left) and optimized structure for multi-level rectangular gratings.

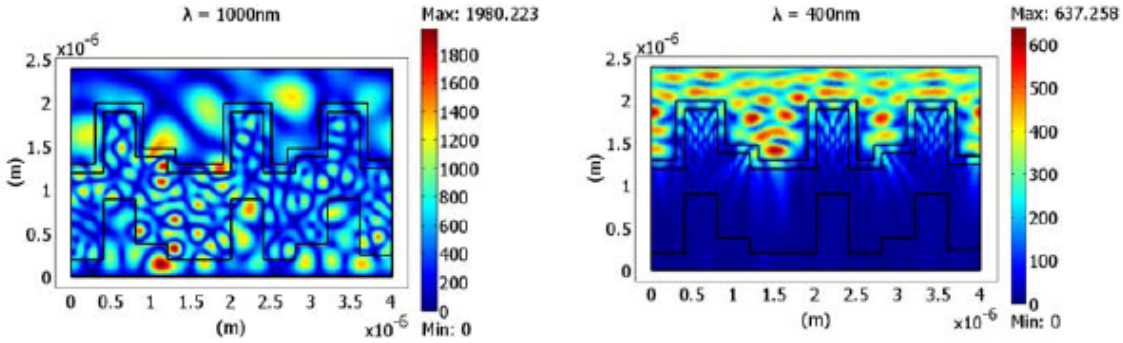

Figure 2.9 (Left) electric field profile at λ=1000nm. (right) electric field profile at

λ=400nm for multi-level rectangular gratings.

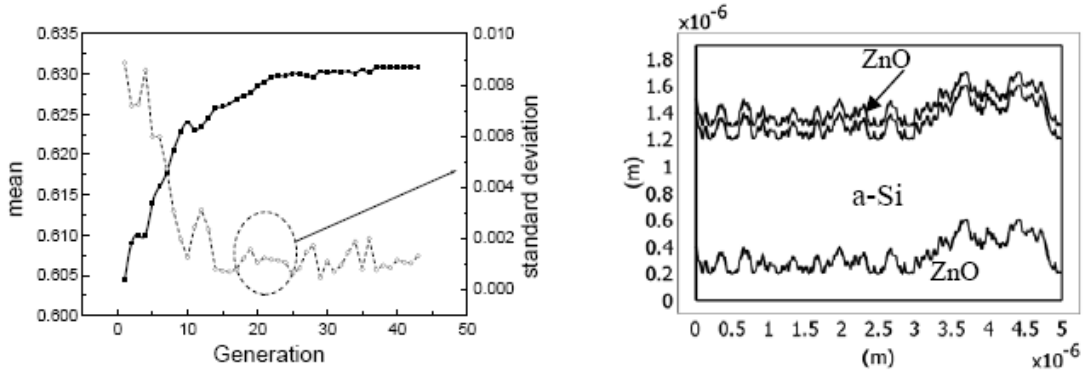

Figure 2.10 Genetic algorithm statistics (left) and optimized structure for multi-level rectangular gratings.

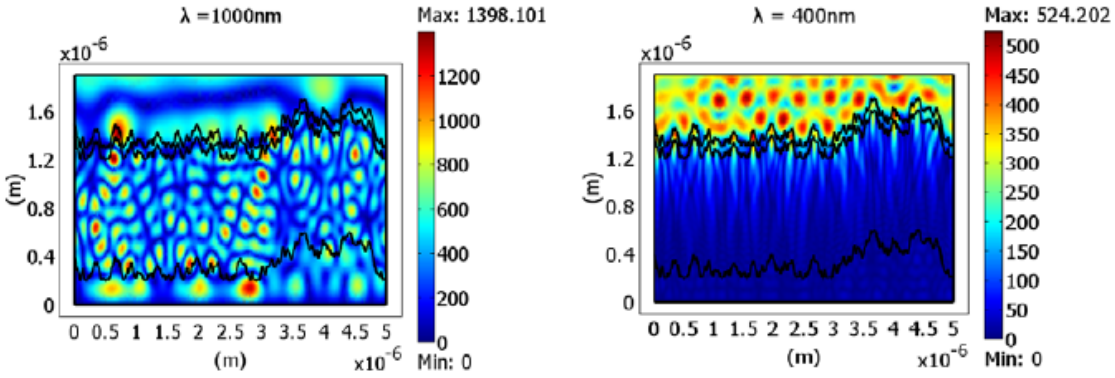

Figure 2.11 (Left) electric field profile at λ=1000nm. (right) electric field profile at λ=400nm for arbitrarily-shaped rectangular gratings.

The four-level rectangular grating demonstrates an appreciable increase in efficiency over the periodic grating, though it is not clear that this geometry is the ***optimal*** grating, based on the practical constraints defined for rectangular geometry and four level limitation. Experimentally, randomly textured ZnO/Ag back reflectors have always demonstrated high performance, but the underlying reason is still not very clear. The use of the GA approach to examine an arbitrary reflector geometry may provide insight to the optimal geometry and high performance of solar cells using textured surfaces. Initializing a random structure for the GA optimization resulted in high integrated QE before

optimization, indicating the high performance achievable for randomized patterns in comparison to well-defined grating structures. The final structure of a GA optimized structure is shown in Figure 2.10, with electric field profiles at λ=1000 nm and λ=400 nm shown in Figure 2.11. The GA optimized arbitrarily shaped grating is capable of achieving an integrated QE of 0.6313, an improvement of 9.04% over the best cell with periodic gratings and 29.6% over a planar solar cell.

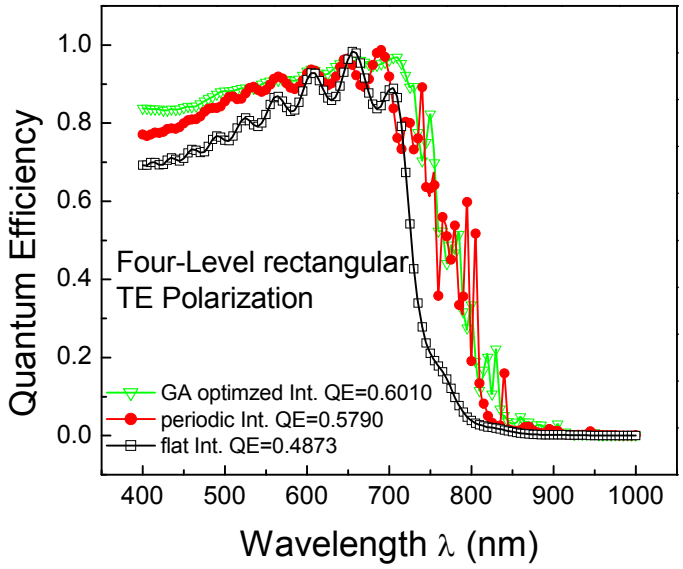

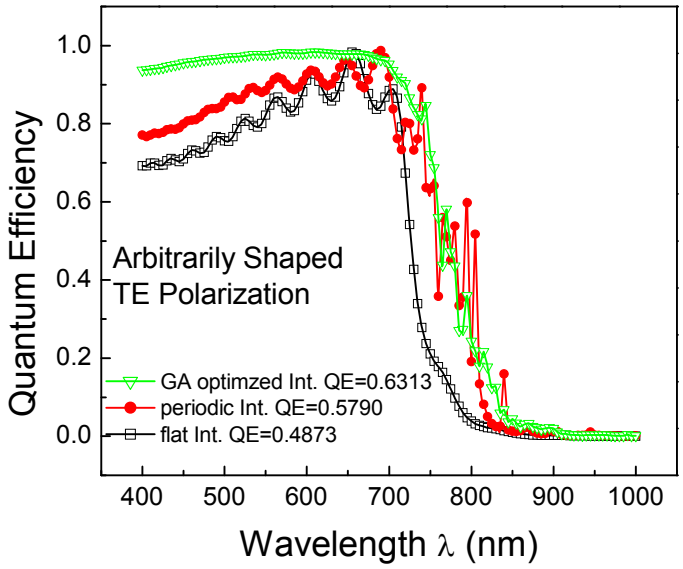

Figure 2.12 The spectral response of flat cell for TE polarization, cell with the most efficient periodic grating couplers, and GA optimized gratings.

It is instructive to examine the spectral response of the various grating structures, in addition to the integrated QE, as shown in Figure 2.12. Flat cells and periodic gratings show impedance matching characteristics, which can be easily observed at short wavelength (λ=400 nm-600 nm). The GA optimized structure demonstrates a relatively flat response at these wavelengths, which is a primary source for overall solar cell efficiency improvement. Since optical absorption is strong at these short wavelengths, the flat response may be attributed to improved optical coupling (i.e. broadband anti-reflection) rather than light trapping. At longer wavelengths, absorption in the cell is weaker, where cell efficiency will depend on the ability to diffract and trap light in the cell. Light diffraction and trapping in periodic cells only occurs strongly at defined resonance peaks, where optical interactions are weak for the remaining solar spectrum. In the arbitrary grating structure, there is significant light trapping across a broad range of the solar spectrum, leading to increased efficiency. This point is reinforced by the comparison between the spectral response of multi-level rectangular grating and arbitrarily shaped gratings where the latter has much higher integrated quantum

efficiency. Although not as strong as in periodic gratings, some resonance is still observed for the four-level rectangular gratings, while there is almost no resonance peak for the arbitrarily shaped gratings. From these results, it is clear that a flat response is a desirable characteristic for diffraction gratings in the solar cell.

It is also illustrative to exam the polarization dependence of optimized structure. Figure 2.13 shows the spectral response and resultant integrated quantum efficiency for the case of TM polarized light. Notice that the efficiency is higher for the randomized 4-level or arbitrarily shaped structure, compared to optimal cell with periodic gratings. This finding further pinpoints the superiority of the random reflector over a well-defined structure as far as the broad-band solar spectrum is concerned. For a random structure, the polarization preference is much weaker, though on the contrary, periodic structures normally lead to strong polarization dependence due to its well-defined geometry that can only respond well to certain wavelengths at one polarization. Periodic 2-D gratings might eliminate the polarization dependence, though stronger resonance peaks are expected and overall integrated quantum efficiency might not be improved to noticeable extent. Polarization dependence can be completely removed in 2-D randomized gratings. In addition, it might also be capable of achieving weak angle dependence structure where the change in cell absorbance is minimal with respect to varying incidence angles.

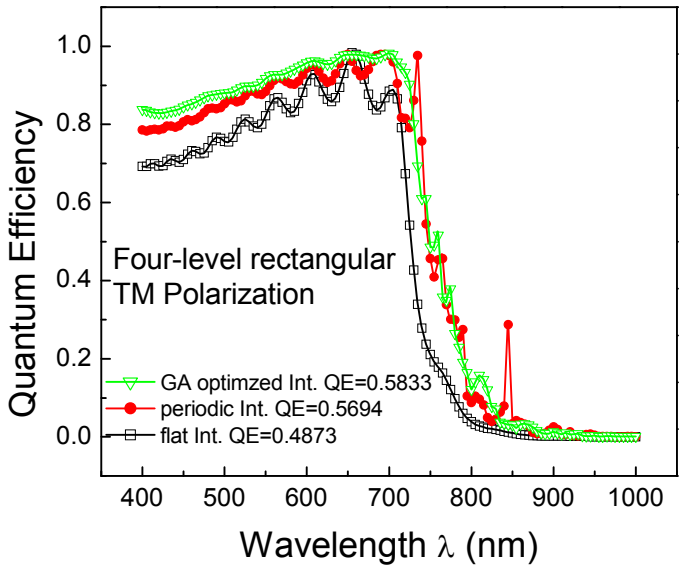

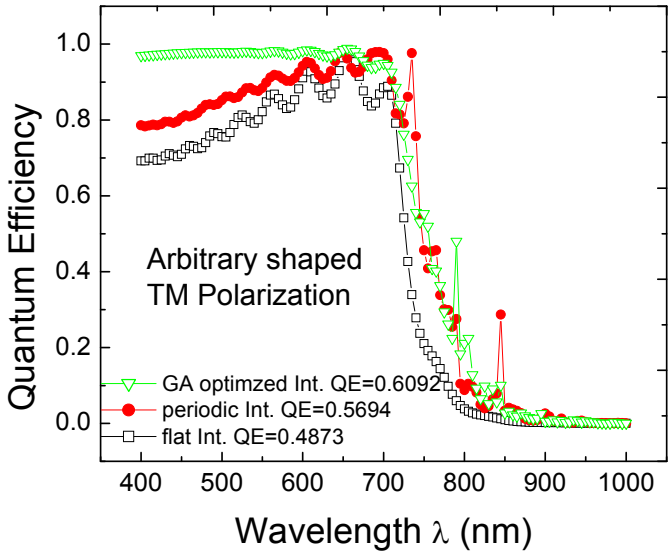

Figure 2.13 The spectral response of flat cell for TM polarization, cell with the most efficient periodic grating couplers, and GA optimized gratings.

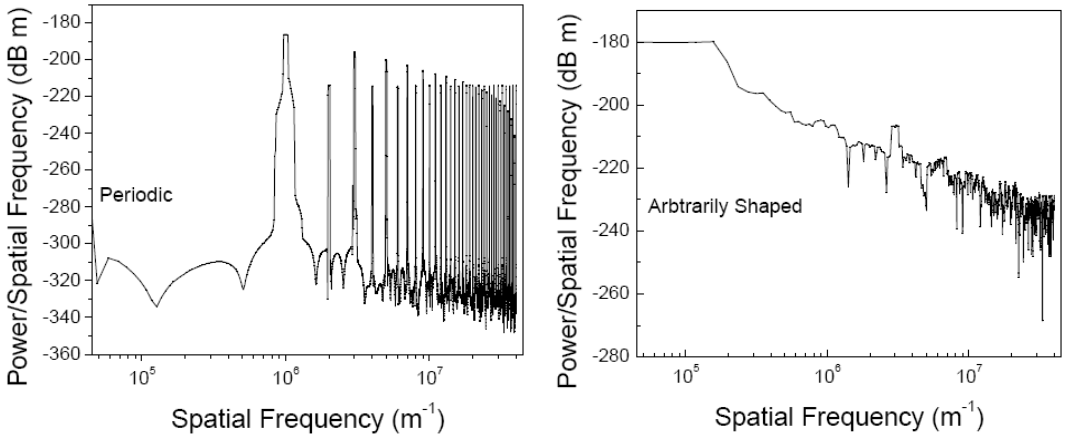

Figure 2.14 The power spectral density (PSD) of flat cell, cell with the most efficient periodic grating couplers, and GA optimized gratings.

The surface texture of the GA optimized structure may be further analyzed to gain insight to the high QE observed. Fourier analysis of the rectangular periodic grating and arbitrarily shaped GA optimized grating are shown in Figure 2.14. Here we utilize the Power Spectral Density (PSD) to characterize our proposed ZnO/Ag back reflectors structure [54, 55]. PSD is a spectral analysis method based on FFT (Fast Fourier

Transform) and our calculation of PSD is done with the help of Matlab signal processing toolbox using the Multitaper method. Detailed mathematics background can be found in [56]. The PSD provides a means of illustrating the spatial frequency components of the surface texture, and hence facilitates the analysis of the interaction between the surface microstructures and light. PSD is a valuable analysis tool particularly when regularity of the surface needs to be minimized. A standard technique of characterizing surface roughness is through simply providing a value for rms roughness, however this does not provide information on the spatial dimensions of the roughness. In fact, it is possible for both a virtually random and an extremely regular surface to produce the same rms roughness value. However, a random surface will have essentially no peaks in the PSD plot, while a very regular surface will show strong peaks[57]. By placing limits on the power measured in the PSD, a desired level of randomness in the surface can be ensured. The PSD for periodic and GA optimized random gratings are shown in Figure 2.14. The PSD for the periodic grating shows strong peaks at several spatial frequencies corresponding to the periodicity in the structure, while other frequencies have a relatively weak spectral power. The vertical scale is from -360 to -170 dBm and the variation of the power spectrum is very significant. The sharp features in the PSD would be undesirable for a solar cell grating, where sharp resonance will be observed, but only at narrow bands within the solar spectrum. It should be noted that these preferential frequencies may not directly coincide with the resonance frequency observed in the solar cell spectral response since detailed analysis (e.g. Maxwell's equations) has to be done in order to know the interaction between the optical wave and spatial dimensions of the grating. For GA-optimized arbitrarily shaped gratings, no strong peak is observed in its PSD plot while the power spectrum has spatial frequency components at almost every frequency. The power decreases by several orders of magnitude with increased spatial frequency, similar to experimentally measured PSD of textured ZnO surface. Note the vertical scale is from -280 to -170 dBm and the variation of the spectral density is relatively small compared to periodic gratings indicating GA-optimized arbitrarily shaped gratings' random nature. The PSD is consistent with its spectral response where there are no strong resonant peaks. The optimal grating will therefore provide the maximum optical coupling and trapping when considering the full solar spectrum, generally resulting in a flat PSD

across spatial frequencies. Some shape of the PSD spectrum might be expected for the optimal diffraction grating to match the shape of the solar spectrum, though we observe little, if any, shape for the GA optimized structures studied.

2.5 Conclusion

Optical aspect of photovoltaic devices is studied and conversion efficiency is calculated for thin film solar cells with varying diffraction grating geometry assuming ideal collection efficiency and using rigorous solutions of Maxwell's equations. Planar cells show QE fluctuations with the thickness of the individual layers or wavelength, attributed to impedance matching and wavelength dependent absorption coefficient. Cells with periodic grating couplers show higher QE at short wavelength in comparison to planar cells as a result of higher transmission introduced by the grating structure on the front contact. At longer wavelength, resonance peaks are observed at specific wavelengths corresponding to the geometry of the grating. The resonant behavior provides an overall higher QE for cells with periodic gratings in comparison to planar cells, attributed to light trapping. GA optimized multilevel-rectangular gratings provide a 23% improvement over flat cells and 3.8% improvement over the best cell with periodic gratings. The improved behavior is believed to be the result of light coupling and trapping effects for a broad range of the solar spectrum. GA optimized arbitrarily shaped gratings further enhance this effect, where a 29% improvement over flat cells and 9% improvement over the best periodic gratings are observed. Arbitrarily shaped grating demonstrate a very flat spectral response and uniform PSD. Analysis of the PSD on experimental solar cell diffraction gratings would provide a useful tool in the optimization of these structures. This work further confirms the value of utilizing randomly textured surfaces for optimal efficiency of thin film solar cells.

Chapter III 0-Dimensional Semi-Analytical Modeling of Intermediate Band Solar Cell

3.1 Introduction

Single-junction photovoltaic solar cells have demonstrated the ability to achieve power conversion efficiency values near the maximum theoretical limit [1, 4]. However, the maximum power conversion limitation for single-junction solar cells is lower than desired, due to energy loss for solar photons with energy exceeding the bandgap energy and absence of solar cell response to solar photons with energy below the bandgap energy. Power conversion efficiency has been improved for tandem and multi-junction solar cells, but these devices are more complex and are accompanied by higher manufacturing costs. In recent years, intermediate-band solar cells (IBSC) have been proposed to exceed efficiency limitations of conventional single-junction cells [1, 20]. Since the original IBSC model by Luque and Marti in 1997 [20], there have been several continued efforts similar to this detailed balance approach [58-67]. Nevertheless, the effect of carrier transport and recombination has not been adequately incorporated in these models despite the major impact of these processes on the solar cell conversion efficiency. The neglect of carrier transport and recombination in IBSC models ignores important physical characteristics of the devices, where proposed approaches of realizing an intermediate band are well known to strongly influence carrier transport and recombination properties in the material and ultimate solar cell conversion efficiency. The incorporation of impurities or introduction of a dilute alloy (e.g. N in III-N_x-V_{1-x} or O in II-O_x-VI_{1-x}) will significantly alter carrier transport and will typical decrease the minority carrier lifetime [31, 35, 36, 38]. Techniques of synthesizing quantum dots may also increase non-radiative or interface recombination rates, while the radiative recombination lifetimes

may be inherently short in the range of nanoseconds [38, 68-72]. It is therefore highly important to include the effects of carrier transport and recombination for IBSC models to ensure that calculated power conversion efficiency values are not significantly over-estimated. The incorporation of carrier transport and recombination also provides a means of investigating the impact of important material parameters such as carrier mobility and minority carrier recombination lifetime on solar cell operation to properly guide the design and analysis of these devices. In this study, we assess the performance of IBSC via a semi-analytical model that incorporates the influence of finite carrier mobility and carrier recombination mechanisms to highlight the influence of these non-ideal properties and their influence on conversion efficiency. The IBSC model presented is further applied to determine the optimal concentration of intermediate band states and energetic position of these states for an IBSC.

3.2 Detailed Balance Efficiency Limit for Intermediate Band Solar Cell

The derivation of detailed balance efficiency limit is under the assumption that only radiative recombination exists in semiconductor [20]. Starting from photon rate equation, the spontaneous emission, absorption, and stimulated emission are three mechanism that transfer the electrons from one band to the other.

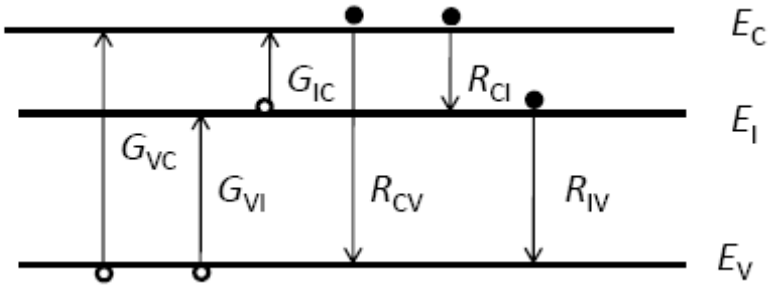

Figure 3.1 Illustration of different transition mechanism in IBSC

The existence of intermediate band provides two additional paths for generation and recombination processes to occur, which corresponds to the second and third summation in Eq. 3.1

$$\frac{d\nu}{dx} = \frac{n}{c}\sum_{i,j}[h_{\mathrm{Ci,Vj}}(\nu+1)f_{\mathrm{Ci}}(1-f_{\mathrm{Vj}}) - h_{\mathrm{Vj,Ci}}\nu(1-f_{\mathrm{Ci}})f_{\mathrm{Vj}}]$$
$$+\frac{n}{c}\sum_{i,j}[h_{\mathrm{Ci,Ij}}(\nu+1)f_{\mathrm{Ci}}(1-f_{\mathrm{Ij}}) - h_{\mathrm{Ij,Ci}}\nu(1-f_{\mathrm{Ci}})f_{\mathrm{Ij}}] \qquad 3.1$$
$$+\frac{n}{c}\sum_{i,j}[h_{\mathrm{Ii,Vj}}(\nu+1)f_{\mathrm{Ii}}(1-f_{\mathrm{Vj}}) - h_{\mathrm{Vj,Ii}}\nu(1-f_{\mathrm{Ii}})f_{\mathrm{Vj}}]$$

n is refractive index of the semiconductor, c is the speed of the light. h is the coefficient relates to oscillator strength of radiative transition, f is the occupation factor of the electronic states. Subscript is of the form Xy (X = C, V, I, y = i, j). X represents CB, VB, or IB. y is the state index, representing initial or final state. υ is the photon number in the mode. x is space coordinate.

Eq. 3.1 can be arranged into the form [20]

$$\frac{d\nu}{dx} = -\alpha_{\mathrm{VC}}(\nu-\nu_{\mathrm{CV}}) - \alpha_{\mathrm{IC}}(\nu-\nu_{\mathrm{CI}}) - \alpha_{\mathrm{VI}}(\nu-\nu_{\mathrm{IV}}) \qquad 3.2$$

where α_{VC}, α_{IC}, α_{VI} are the absorption coefficient for VB to CB, IB to CB and VB to IB transitions respectively. The values of ν_{XY} (X, Y = C, I , or V) are given by

$$\nu_{\mathrm{XY}} = \frac{1}{1+\exp(\frac{E_{\mathrm{XY}}-\mu_{\mathrm{XY}}}{kT})} \qquad 3.3$$

where E is energy and $\mu_{\mathrm{XY}} = E_{\mathrm{FX}}$-$E_{\mathrm{FY}}$ is the separation between quasi-Fermi levels. It should be noted that $\mu_{\mathrm{CV}} = E_{\mathrm{FC}}$-$E_{\mathrm{FV}} = V_{\mathrm{A}}$ is the applied bias of the diode. The efficiency then can be calculated by integration over photons of different energy. The details for the calculation can be found in literature [59, 60, 62].

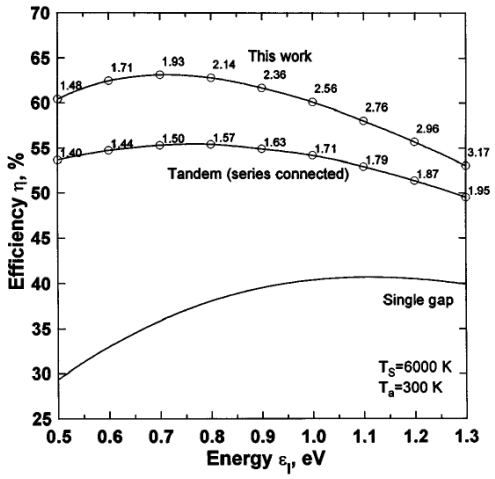

Figure 3.2 Comparison of intermediate band solar cells and single and multi-junction cells. Reference A. Luque and A. Marti, Phys. Rev. Lett. Vol. 78, pp. 5014, (1997) [20]

The detailed balance model predict an ideal efficiency of 63.2% [20, 59, 60, 62] though it doesn't include the effect of finite mobility and realistic lifetime which might be much shorter than radiative lifetime predicted by black body radiation. In the following section, carrier transport and recombination model is presented to provide deeper insight into the operation of intermediate band solar cell.

3.3 Carrier Transport and Recombination Model

3.3.1 Theoretical Background and Formulation

The neglect of carrier transport and recombination in IBSC models ignores important physical characteristics of the devices, where proposed approaches of realizing an intermediate band are well known to strongly influence carrier transport and recombination properties in the material and ultimate solar cell conversion efficiency. It is therefore highly important to include the effects of carrier transport and recombination for IBSC models to ensure that calculated power conversion efficiency values are not significantly over-estimated.

A common photovoltaic solar cell device structure proposed for the IBSC is the p-i-n (or p-υ-n and p-π-n) configuration [21, 22, 24-26, 73-75], which will also be used in this

study (Figure 3.3). This device structure incorporates a lightly doped absorber region and highly doped p- and n-type layers that clamp the built-in potential to maintain a large open circuit voltage [73].

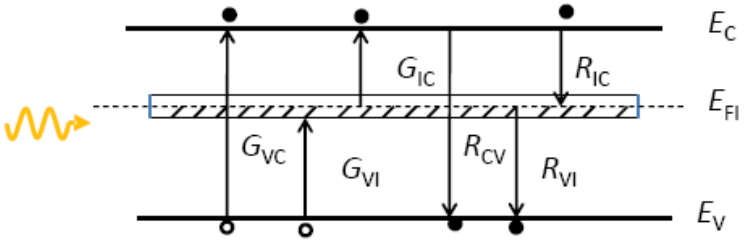

Figure 3.3 Illustration of device structure and generation-recombination mechanisms in the IBSC model.

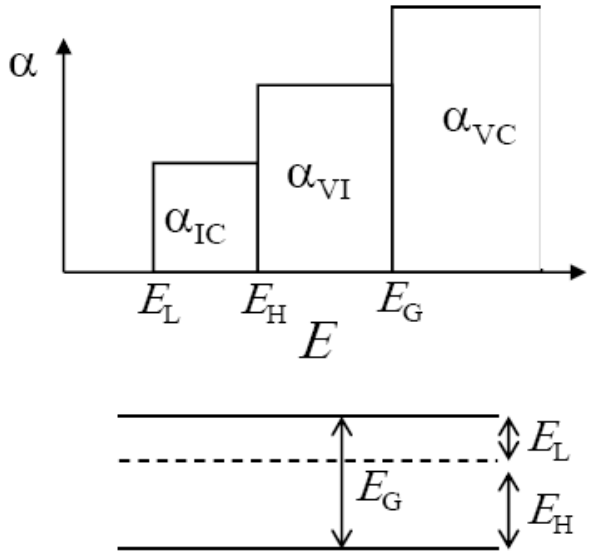

Figure 3.4 Illustration of absorption coefficient v.s. photon energy (top) and E_L, E_H, E_G (Bottom).

The baseline photocurrent density due to valence to conduction band optical transitions for this device structure may be expressed as [76-78]

$$J_{\text{ph, baseline}} = J_{L0} D\left[1 - \exp\left(-1/D\right)\right] \qquad 3.4.a.$$

$$D = l_c\left(1-\frac{V_A}{V_{bi}}\right)/W \qquad 3.4.b.$$

where W is the width of absorber, J_{L0} is the photocurrent density at large reverse bias [77], μ_n and μ_p are the electron and hole mobilities, $\tau_{n,tot}$ and $\tau_{p,tot}$ are the total recombination lifetime values for electrons and holes, F is the electric field, l_n and l_p are the electron and hole drift length, and l_C is the collection length defined by $l_C = l_n + l_p = \mu_n F \tau_{n,tot} + \mu_p F \tau_{p,tot}$. The ratio of $W/[\, l_C(1\text{-}V_A/V_{bi})]$ determines the charge collection efficiency, where the case of large W with respect to drift length would result in low charge collection efficiency due to carrier recombination prior to collection at the p- and n-type emitters.

The intermediate band provides an additional generation-recombination path represented by

$$G_{IC}(x) = \int_{E_L}^{E_H} \alpha_{IC}(E) I_0(E) \exp(-\alpha_{tot}(E)x) dE \qquad 3.5.a.$$

$$G_{VI}(x) = \int_{E_H}^{E_G} \alpha_{VI}(E) I_0(E) \exp(-\alpha_{tot}(E)x) dE \qquad 3.5.b.$$

where G_{IC} is the generation rate from intermediate to conduction band and G_{VI} is the generation rate from valence to intermediate band, $I_0(E)$ is the incident light from the solar spectrum, E represents energy, and α_{IC} and α_{VI} is the absorption coefficient for IB to CB and VB to IB transition respectively. The solar spectrum can be given as

$$I_0(E) = f_s X \frac{2\pi}{h^3 c^2} \frac{E^2}{exp\left(\frac{E}{kT_{sun}}\right)-1} \qquad 3.6$$

where f_s = 1/46050 is the solid angle subtended by the sun, X is the solar concentration, and T_{sun} = 5963 K is the temperature of sun, k is the Boltzmann constant, c is the speed of light, and h is the Plank constant. In this study, X=1 (one sun condition) is assumed unless otherwise noted. The absorption coefficient for the optical transitions is dependent on carrier occupation in the intermediate electronic states, represented by [23]:

$$\alpha_{IC} = \alpha_{IC0} f, \;\; \alpha_{VI} = \alpha_{VI0}(1-f) \qquad 3.7$$

where α_{IC} and α_{VI} are the absorption coefficients for IB to conduction band (CB) and valence band (VB) to IB transitions, respectively (Figure 3.4), and f characterizes the filling of IB. This formulation accounts for the effect of IB electron state filling on the

absorption process, where the presence of an electron (hole) is required for for IB (VB) to CB (IB) transitions. The absorption coefficient constants α_{IC0} and α_{VI0} represent the oscillator strength of the transitions and density of states in the energy bands.

The net photocurrent density due to photo-generated carriers via the intermediate band may then be calculated by substituting the generation rates above into the continuity equation for photo-generated excess carriers, as described in the following. The uniform field approximation is used [76], assuming that the electric field does not significantly vary across the lightly doped or intrinsic region. The electric field may deviate from this assumption near the edge of the depletion region, but is not expected to significantly alter charge collection. The diffusion current is assumed to be negligible for this device, where the i (υ, π) region will be fully depleted and the drift field will be responsible for electron-hole pair separation for photo-generated carriers. The continuity equation for excess electron concentration can then be written as

$$v_n \frac{d\Delta n(x)}{dx} + \frac{\Delta n(x)}{\tau_{n,\,tot}} = G_{IC}(x) \quad B.C. \quad \Delta n(0) = 0 \qquad 3.8$$

where $v_n = \mu_n F$, $F = V_{bi}/W$, μ_n is electron mobility, V_{bi} is the built-in potential, W is the absorber basewidth, and $\tau_{n,tot}$ is the net recombination lifetime for electrons in the conduction band. The boundary condition for this device defines that the excess carrier concentration vanishes at the depletion region edge under short circuit conditions [73, 74, 76]. The net recombination lifetime, including non-radiative processes, may be described by

$$1/\tau_{n,tot} = 1/\tau_{CI} + 1/\tau_{CV} + 1/\tau_{n,int} + 1/\tau_{nr} \qquad 3.9.a.$$

Similarly for holes, the net recombination lifetime may be described by

$$1/\tau_{p,tot} = 1/\tau_{IV} + 1/\tau_{CV} + 1/\tau_{p,int} + 1/\tau_{nr} \qquad 3.9.b.$$

where τ_{CV}, τ_{CI}, and τ_{IV} are radiative recombination lifetime for CB to VB, CB to IB and IB to VB transitions respectively. The variable τ_{int} is the internal recombination lifetime, which represents recombination associated with the overlap between optical absorption spectra for the three transisitions in the IBSC [60]. Non-radiative recombination is represented by the lifetime parameter τ_{nr}. The radiative carrier lifetimes associated with IB transitions, τ_{CI} and τ_{IV}, may be described as [61]

$$\tau_{\mathrm{CI}} = \left[\frac{1}{n_0} \frac{2\pi}{h^3 c^2} \int_{E_{\mathrm{L}}}^{E_{\mathrm{H}}} \alpha_{\mathrm{IC}} \exp\left(-\frac{E}{kT} \right) E^2 dE \right]^{-1} \qquad 3.10.a.$$

$$\tau_{\mathrm{IV}} = \left[\frac{1}{p_0} \frac{2\pi}{h^3 c^2} \int_{E_{\mathrm{H}}}^{E_{\mathrm{G}}} \alpha_{\mathrm{VI}} \exp\left(-\frac{E}{kT} \right) E^2 dE \right]^{-1} \qquad 3.10.b.$$

where n_0 and p_0 are electron and hole equilibrium carrier concentrations. The energy values E_{L}, E_{H} and E_{G} represent the edge of the absorption transitions, as shown in Fig. 2. The calculated values of τ_{CI} and τ_{IV} using Eq. 3.10.a and Eq. 3.10.b are in the range of μs. Overlap between the absorption spectra of the optical transitions is assumed to be negligible in this analysis (neglect τ_{int}). Non-radiative recombination processes are lumped in the constant τ_{nr}, including Shockley-Read-Hall and other non-radiative processes.

The solution to the continuity equation (Eq. 3.8) is

$$\Delta n(x) = \int_0^x G_{\mathrm{IC}}(x') / v_n \exp\left(\frac{x' - W}{l_{\mathrm{n}}} \right) dx' \qquad 3.11$$

where $l_{\mathrm{n}} = v_{\mathrm{n}} \tau_{\mathrm{n\_tot}}$ is the electron drift length. The electron photocurrent density due to optical generation via the intermediate band can then be determined by

$$J_{\mathrm{ph,\ IB,\ n}} = q v_{\mathrm{n}} \Delta n(W) = q \int_0^W G_{\mathrm{IC}}(x) \exp\left(\frac{x - W}{l_{\mathrm{n}}} \right) dx \qquad 3.12.a.$$

Similarly, the hole photocurrent density due to optical generation via the intermediate band can be determined by

$$J_{\mathrm{ph,\ IB,\ p}} = q v_{\mathrm{p}} \Delta p(0) = q \int_0^W G_{\mathrm{VI}}(x) \exp\left(\frac{-x}{l_{\mathrm{p}}} \right) dx \qquad 3.12.b.$$

Substituting G_{IC} and G_{VI} (Eq. 3.5.a and Eq. 3.5.b) into the electron and hole current density equations (Eq. 3.12.a and Eq. 3.12.b), the intermediate band occupation factor f may be solved by matching electron and hole photocurrent density

$$J_{\text{ph, IB, n}}(f) = q\int G_{\text{IC}}(x,f)\exp\left(\frac{x-W}{l_{\text{n}}}\right)dx$$

$$= \qquad 3.13$$

$$J_{\text{ph, IB, p}}(f) = q\int G_{\text{VI}}(x,f)\exp(\frac{-x}{l_{\text{p}}})dx$$

The constraint to match electron and hole photocurrent density via the intermediate band is based on the requirement that the net generation and recombination rate in the absorber are balanced to maintain charge neutrality. The intermediate band occupation factor, *f*, may have a spatial dependence, but is assumed to be a constant for the intrinsic or lightly doped absorber region [20, 59, 60].

The diode dark current density may be expressed as

$$J_{\text{D}} = J_{\text{diff}} + J_{\text{r,CV}} + J_{\text{r,CI}} + J_{\text{nr}} \qquad 3.14.\text{a.}$$

The first term J_{diff} is the diffusion current represented by

$$J_{\text{diff}} = \left(\frac{qn_{\text{i}}^2 D_{\text{n}}}{N_{\text{D}}W_{\text{p}}} + \frac{qn_{\text{i}}^2 D_{\text{p}}}{N_{\text{A}}W_{\text{n}}}\right)\times\left[\exp\left(\frac{qV_{\text{A}}}{kT}\right)-1\right] \qquad 3.14.\text{b.}$$

where V_{A} is the applied bias, W_{p} and W_{n} are the width of the p- and n-type emitter layers, N_{A} and N_{D} are the acceptor and donor concentration in the p- and n-type emitter layers, n_{i} is the intrinsic carrier concentration, and D_{n} and D_{p} are electron and hole diffusion coefficients. In this study, the device parameters for the heavily-doped p- and n-type layers are assumed to be $W_{\text{p}} = W_{\text{n}} = 0.1$ μm, $N_{\text{A}} = N_{\text{D}} = 10^{19}$ cm^{-3}. The values of D_{n} and D_{p} are determined by the Einstein relation using the mobility values defined. The term $J_{\text{r,CV}}$ is the radiative band to band recombination current density given by[20, 58, 59]

$$J_{\text{r,CV}} = q\frac{2\pi}{h^3c^2}\int_{E_{\text{G}}}^{\infty} e^{-\frac{E}{KT}}E^2\left(1-e^{\alpha_{\text{VC}}W}\right)dE\times\left[\exp\left(\frac{qV_{\text{A}}}{kT}\right)-1\right] \qquad 3.14.\text{c.}$$

The radiative recombination current density due to the IB can be described by [20, 58, 59, 62]

$$J_{\mathrm{r,CI}} = J_{0,\mathrm{r,CI}}\left[\exp\left(\frac{q\mu_{\mathrm{CI}}}{kT}\right)-1\right] = J_{0,\mathrm{r,CI}}\left[\exp\left(\frac{qV_{\mathrm{A}}(1-\xi)}{kT}\right)-1\right] \quad \text{3.14.d.}$$

where $\mu_{\mathrm{CI}} = E_{\mathrm{FC}} - E_{\mathrm{FI}}$ represents the splitting of Fermi level between CB and IB.

The value of μ_{CI} is a fraction of V_{A} related by (1-ξ) V_{A} , where ξ is a value between 0 and 1 under dark conditions. The parameter ξ is determined by matching the electron and hole recombination current density via the intermediate band in the dark

$$\begin{aligned} J_{\mathrm{r,CI}} &= J_{0,\mathrm{r,CI}}\left[\exp\left(\frac{qV_{\mathrm{A}}(1-\xi)}{kT}\right)-1\right] \\ &= J_{0,\mathrm{r,IV}}\left[\exp\left(\frac{q\mu_{\mathrm{IV}}}{kT}\right)-1\right] = J_{0,\mathrm{r,IV}}\left[\exp\left(\frac{qV_{\mathrm{A}}\xi}{kT}\right)-1\right] \\ &= J_{\mathrm{r,IV}} \end{aligned} \quad \text{3.14.e.}$$

Where

$$J_{0,\mathrm{r,CI}} = q\frac{2\pi}{h^3c^2}\int_{E_{\mathrm{L}}}^{E_{\mathrm{H}}} e^{-\frac{E}{KT}}E^2\left(1-e^{\alpha_{\mathrm{IC}}W}\right)dE \quad \text{3.14.f.}$$

$$J_{0,\mathrm{r,IV}} = q\frac{2\pi}{h^3c^2}\int_{E_{\mathrm{H}}}^{E_{\mathrm{G}}} e^{-\frac{E}{KT}}E^2\left(1-e^{\alpha_{\mathrm{VI}}W}\right)dE \quad \text{3.14.g.}$$

The parameter $\mu_{\mathrm{IV}} = E_{\mathrm{FI}} - E_{\mathrm{FV}}$ can be represented as ξV_{A} due to the relation $\mu_{\mathrm{CI}} + \mu_{\mathrm{IV}} = (1-\xi)\ V_{\mathrm{A}} + \xi\ V_{\mathrm{A}} = V_{\mathrm{A}}$ [20]. The final term for nonradiative recombination current density J_{nr} can be given as

$$J_{\mathrm{nr}} = \frac{qn_{\mathrm{i}}W}{2\tau_{\mathrm{tot}}\gamma}\left[\exp\left(\frac{qV_{\mathrm{A}}}{2kT}\right)-1\right] \quad \text{3.14.h.}$$

where $\gamma = 1 + \tau_{\mathrm{nr}}/\tau_{\mathrm{r}}$. In this study, γ is generally assigned a value of 10 corresponding to a radiative efficiency of 90%, which is a typical value for a high quality direct bandgap semiconductor material such as GaAs. Finally, the total diode current density is determined by the sum of dark current, photocurrent due to valence- to conduction-band and intermediate-band radiative transitions

$$J = J_{\mathrm{D}} - \left(J_{\mathrm{ph,\,baseline}} + J_{\mathrm{ph,\,IB}}\right) \tag{3.15}$$

The power conversion efficiency of the solar cell is calculated as

$$\eta = \frac{J_{\mathrm{sc}} \times V_{\mathrm{oc}} \times FF}{I_{\mathrm{sun}}} \tag{3.16}$$

where J_{sc} is the short circuit current density, V_{oc} is the open circuit voltage, $FF = J_{\mathrm{m}}V_{\mathrm{m}}/J_{\mathrm{sc}}V_{\mathrm{oc}}$ is the fill factor, and I_{sun} is the solar irradiace under one sun condition [58]. The values J_{m} and V_{m} are the current density and voltage at the operating point where the power output from the solar cell is maximum. Similar to the original detailed balance model [20], the analytical model here does not incorporate transport properties within the intermediate band. The carrier transport in the intermediate band may help to balance the charge distribution in the intermediate band, and thus analytical models may be applied more appropriately to the case of efficient IB transport since in these models [20, 58-60, 62, 65, 68], constant absorption coefficient or uniform state filling is assumed. Nonetheless, the true effect of IB transport on solar cell operation has not been clear to date.

The physical processes associated with the intermediate band will depend on the nature and density of the intermediate band electronic states, and will be material and process specific. As a first order approximation, the dependence of optical absorption and carrier lifetime will be related to the concentration of intermediate band states (N_I) according to the following description. Optical absorption coefficients and net recombination lifetime are assumed to have the following linear relationships [23, 27, 28]

$$\alpha_{\mathrm{IC}}(N_{\mathrm{I}}) = \alpha_{\mathrm{IC0}} f = \sigma_{\mathrm{opt,n}} N_{\mathrm{I}} f \tag{3.17.a}$$

$$\alpha_{\mathrm{VI}}(N_{\mathrm{I}}) = \alpha_{\mathrm{VI0}}(1-f) = \sigma_{\mathrm{opt,p}} N_{\mathrm{I}}(1-f) \tag{3.17.b}$$

$$\tau_{\mathrm{tot}}(N_{\mathrm{I}}) = \frac{1}{CN_{\mathrm{I}}} \tag{3.18}$$

where $\sigma_{\mathrm{opt,n}}$ and $\sigma_{\mathrm{opt,p}}$ are electron and hole optical absorption cross sections, and C is the capture coefficient. The expressions in Eq. 3.17.a and Eq. 3.17.b follow the formulation for Shockley-Read-Hall recombination and optical generation from localized donor or acceptor states [27, 28] and has been recently used in the context

of IBSC to explain experimental observations [23]. The recombination lifetime in Eq. 3.18 simply assumes that the recombination lifetime is inversely proportional to the concentration of intermediate band states, similar to SRH lifetime where the lifetime is inversely proportional to trap density. The absorption coefficient α_{VC} and the prefactors α_{IC0} and α_{VI0} are defined in each simulation. Selected simulations define the optical absorption cross section, rather than α_{IC0} and $\alpha_{V\,0}$, in order to study the effect of N_I on IBSC characteristics.

3.3.2 The Numerical Result and Discussion

The model defined for IBSC devices in this work is applicable for any semiconductor material of interest. Material parameters for ZnTe are chosen in this analysis as a prototypical material for IBSC due to recent interest in oxygen-doped ZnTe as an active region for IBSC devices [33, 79]. Two sets of device parameters are used in these simulations to investigate the influence of electron transport and carrier recombination: (1) $W = 1$ μm with $\alpha_{IC0} = \alpha_{VI0} = 10^3$ cm^{-1}, $\alpha_{VC} = 10^4$ cm^{-1} and (2) $W = 10$ μm with $\alpha_{IC0} = \alpha_{VI0} = 10^4$ cm^{-1}, $\alpha_{VC} = 10^4$ cm^{-1}. The parameters for device (1) represent the case of a realistic thin-film IBSC where the absorber region thickness is near 1 μm and the intermediate band optical transition is an order of magnitude weaker than the valence- to conduction-band optical transition. The parameters for device (2) represent the case of a nearly ideal IBSC with a long absorption region and strong intermediate-band optical absorption. Detailed simulation parameters are indicated in the figure caption for each figure. The net electron and hole carrier lifetime values are assumed to be equivalent in these calculations for simplicity.

The current-voltage characteristics for an IBSC with varying absorption coefficients for the IB are shown in Figure 3.5(a), where the short circuit current density J_{sc} clearly increases with increasing α_{IC0} and α_{VI0} while the open circuit voltage V_{oc} does not change significantly. The increase in J_{sc} over the baseline cell (the case of $\alpha_{IC0} = \alpha_{VI0} = 0$ cm^{-1}) is due to subbandgap photon absorption. The higher J_{sc} while maintaining nearly the same V_{oc} is the key aspect of intermediate band photovoltaics. The slight decrease of V_{oc} in the case of $\alpha_{IC0} = \alpha_{VI0} = 10^4$ cm^{-1} is due to the increase of radiative recombination current via the intermediate band. The current-voltage characteristics calculated for the transport and

recombination model (CTR) are compared to prior IBSC calculations that do not account for carrier transport and recombination, as shown in Figure 3.5 (b). Curves (1)-(2) are calculated using the model presented by Luque [20, 60] while curve (3) is the result of the model presented here (CTR). Curve (1) is for an ideal IBSC with full absorption, fully concentrated sunlight, and infinite mobility. Curve (2) assumes a finite base width (W = 1 μm) and no solar concentration (X = 1). The material and device parameters (i.e. W, X, α, E_G, E_I) are the same for curve (2) and curve (3), where differences are the direct result of accounting for carrier transport and recombination. Differences in curves (2) and (3) from curve (1) are primarily related to the effect of assuming full absorption and fully concentrated sunlight. For curve (3), V_{oc}= 1.80 V and J_{sc} /X = 18.30 mA/cm^2 while for the ideal IBSC in curve (1), V_{oc}= 2.28 V and J_{sc} /X = 30.88 mA/cm^2. The reduced V_{oc} is primarily the result of assuming one sun condition (X=1) in comparison to fully concentrated sunlight assumed in previous studies [20, 60]. Solar concentration effectively multiplies the short circuit current J_{sc} by the solar concentration factor X, while also significantly increasing V_{oc}. The increase in V_{oc} is the result of increased generation rate, which increases the energy separation between the electron and hole quasi Fermi levels. The smaller J_{sc} /X predicted in the CTR model is a result of finite device length and consequent incomplete absorption.

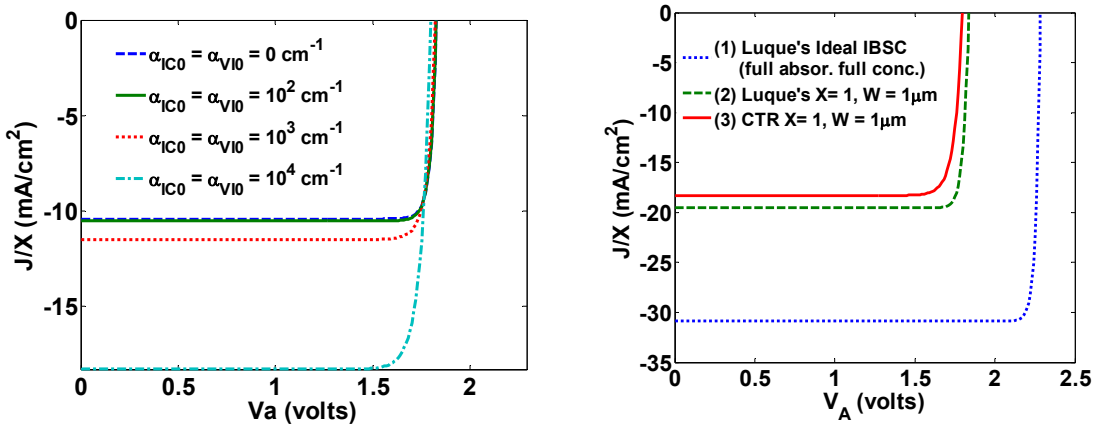

Figure 3.5 Current density versus voltage curves (a) comparing different absorption coefficients for intermediate band transitions with W= 1 μm, τ_{tot}=1 μs, α_{VC} = 10^4 cm^{-1}, E_G = 2.3 eV, E_I = 1.8 eV, μ_n = μ_h = 100 cm^2/Vs and (b) comparing the CTR model of

this work to an ideal IBSC model (Ref. 3) with $\alpha_{VC} = 10^4$ cm^{-1}, $\alpha_{IC0} = \alpha_{VI0} = 10^4$ cm^{-1}, E_G = 2.3 eV, E_I = 1.8 eV, and (for curve (3)) $\mu_n = \mu_h$ = 100 cm^2/Vs and τ_{tot}=1 μs.

Carrier recombination lifetime has a major influence on conversion efficiency, where the mitigation of non-radiative processes is highly important. The dependence of IBSC conversion efficiency on minority carrier lifetime and intermediate band position is depicted in Figure 3.6. In the case of τ_{tot} = 1 μs, the calculated efficiency provides similar results to previous models for an IBSC [60], where maximum efficiency occurs when E_I is symmetrically at one-third and two-thirds of E_G. A decrease in τ_{tot}, which may result from the incorporation of impurities or quantum dots, non-radiative recombination, or lower and more realistic values for carrier lifetime, leads to lower conversion efficiency. In addition to the decrease in conversion efficiency with lower carrier lifetime, the peak conversion efficiency occurs with E_I nearer to the mid-gap for the case of $E_I < E_G/2$, or nearer to the conduction band for the case of $E_I > E_G/2$. The shift of the peak conversion efficiency to different E_I values is a result of the optical absorption characteristic proportional to $\exp(-\alpha x)$ along the device. The overall collection efficiency will therefore be much higher for photo-generated holes than electrons for light incident from the p-side of the diode due to the higher optical generation rate near the p-side and shorter transport length for these excited holes. The maximum conversion efficiency will occur when the electron and hole photocurrent generated by the IB are both at a maximum [20, 60]. Shorter carrier lifetime will result in more charge collection efficiency reduction in electrons then holes, and the shift in IB toward the conduction band edge will provide an increased absorption and corresponding photogeneration rate associated with the IB to CB transition to compensate for this. As a result, the peak efficiency will occur at an E_I value nearer to the conduction bandedge for shorter carrier lifetime. The optimal position for the intermediate band will therefore have a dependence on the carrier lifetime value. It should be noted that the lifetime-dependent optimal position for E_I is a unique outcome of the CTR model employed in this work, a conclusion that is not found in previous models that neglect CTR.

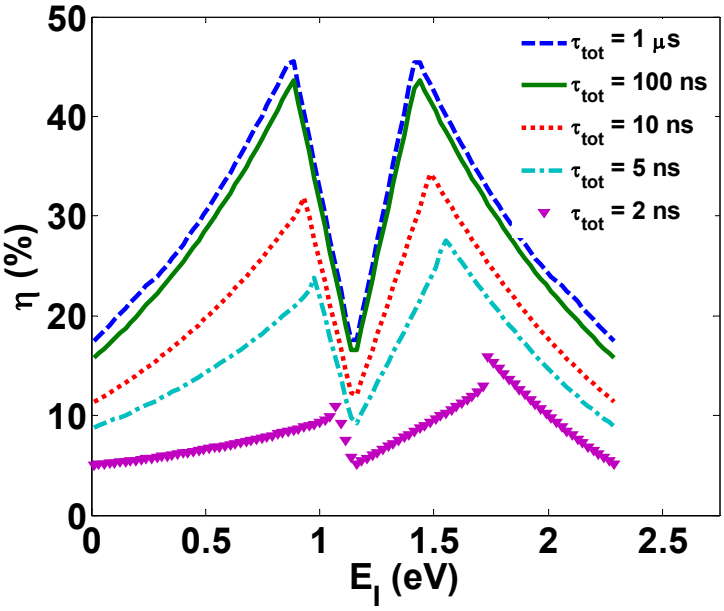

Figure 3.6 Efficiency versus intermediate band energy level (E_I) for varying recombination lifetime values with $\alpha_{VC} = 10^4$ cm^{-1}, $E_G = 2.3$ eV, $\mu_n = \mu_h = 100$ cm^2/Vs, $W = 10$ μm, and $\alpha_{IC0} = \alpha_{VI0} = 10^4$ cm^{-1}.

The energetic position of the intermediate band will strongly influence the power conversion efficiency of the solar cell. Calculations of the efficiency versus energetic position of intermediate band electronic states with respect to the valence band edge (E_I) are shown in Figure 3.7(a), along with the occupation of electronic states in the intermediate band. The occupation of IB electronic states is determined by the balance between generation-recombination mechanisms and carrier transport in the CB and VB. The occupation of IB states will affect optical transitions via the IB and resulting IBSC efficiency. It is generally believed that a half-filled intermediate band is optimal, though it has not been clear how the occupation of intermediate-band states affects the efficiency since occupation is not accounted for in previous IBSC device models [20, 58, 60, 61, 68]. In these simulations, optimal efficiency is confirmed to be near 50% occupation, as shown in Figure 3.7(b). Two curves appear in Figure 3.7(b), corresponding to two possible efficiency values for a given value of IB occupation, depending on the position of E_I.

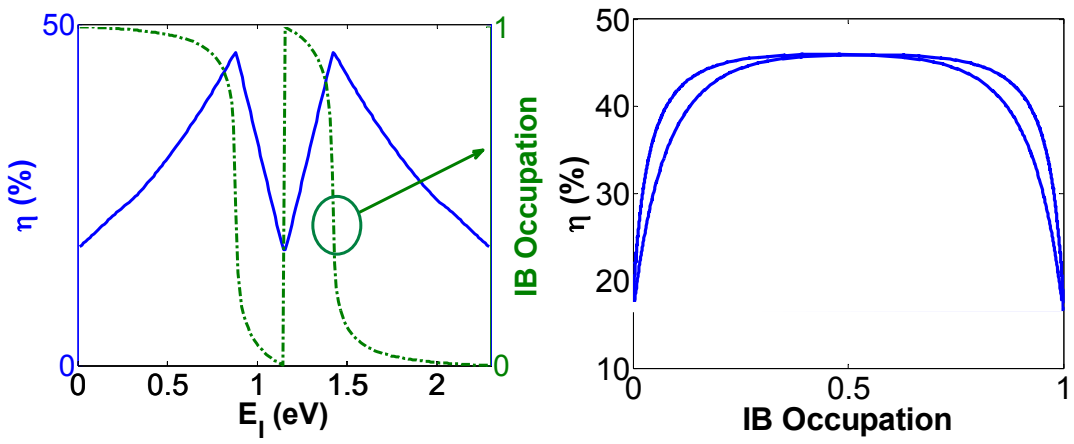

Figure 3.7 Efficiency dependence on intermediate band characteristics as shown by (a) efficiency versus intermediate band energy level (E_I) and (b) efficiency versus IB occupation. E_G = 2.3 eV, $\mu_n = \mu_h$ = 100 cm^2/Vs, W= 10 μm, τ_{tot} = 1 μs, $\alpha_{VC} = 10^4$ cm^{-1}, and $\alpha_{IC0} = \alpha_{VI0} = 10^4$ cm^{-1}.

The density of electronic states in the IB (N_I) will impact both optical absorption properties and carrier recombination processes. A quantitative understanding of these relationships is necessary for an accurate IBSC model. First order approximations of the influence of N_I on IBSC performance may be obtained by assuming values for optical absorption cross section and capture coefficient and evaluating trends with respect to conversion efficiency as described in section 3.3.1. Plots of calculated efficiency versus N_I are shown in Figure 3.8 and Figure 3.9 for varying values of carrier lifetime, absorber width, optical absorption cross section, and capture coefficient. For a given set of material parameters, an optimal value for N_I can be found.

Increasing the optical absorption cross section σ_{opt} shifts the optimal N_I to lower values, due to increased optical absorption via the IB. Increasing capture coefficient C also results in a shift of the optimal N_I to lower values, but also results in reduced conversion efficiency due to faster relaxation of photogenerated carriers. For higher carrier capture, such as $C = 10^{-8}$ cm^{3}s^{-1} curve, the benefit of the IB is lost and the efficiency of the IBSC is reduced to a value below a single junction without an IB. Large values for capture coefficient C represent correspondingly small values in carrier lifetime. Experimental data for $\alpha(N_I)$ and $\tau_{tot}(N_I)$ may alternatively be used in these calculations, and would provide a more accurate method of evaluating the optimal N_I for a specific

material system proposed for IBSC. The determination of optimal N_I in this work is another unique outcome of the CTR model that has not been previously examined, and can guide the future design of IBSC given the establishment of IB physical parameters.

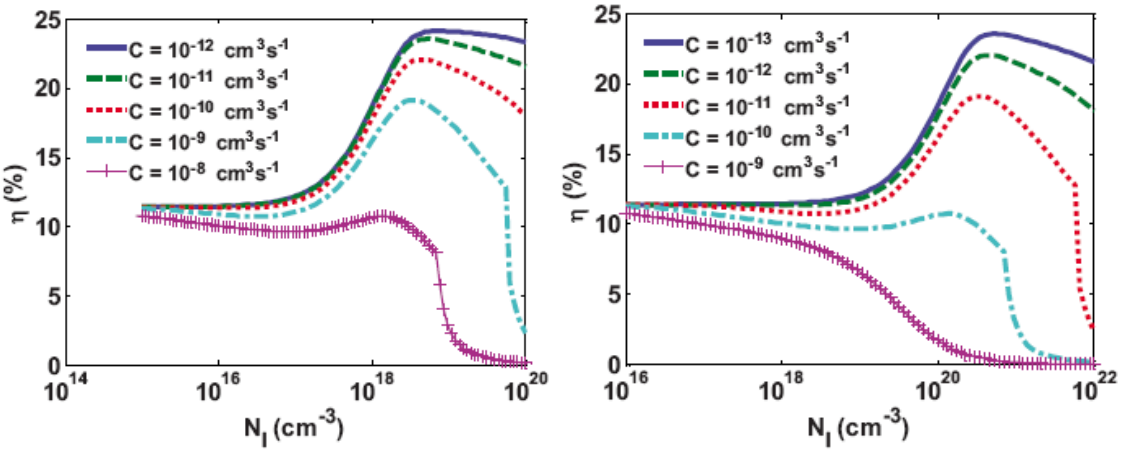

Figure 3.8 Efficiency versus density of intermediate band states (N_I) for a device with a base width of W= 1 μm, and $\alpha_{VC} = 10^4$ cm^{-1}, $E_G = 2.3$ eV, $E_I = 1.8$ eV, $\mu_n = \mu_h = 100$ cm^2/Vs, $\alpha_{IC0} = \alpha_{VI0} = 10^3$ cm^{-1} with values of optical cross section of (left) $\sigma_{opt} = 10^{-14}$ cm^2 and (right) $\sigma_{opt} = 10^{-16}$ cm^2.

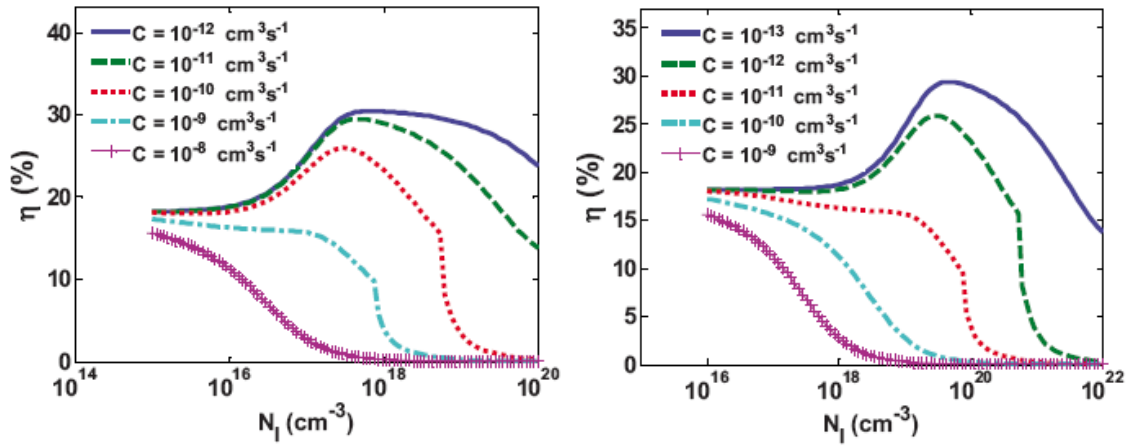

Figure 3.9 Efficiency versus density of intermediate band states (N_I) for a device with base width of W= 10 μm, $\alpha_{VC} = 10^4$ cm^{-1}, $E_G = 2.3$ eV, $E_I = 1.8$ eV, $\mu_n = \mu_h = 100$ cm^2/Vs, $\alpha_{IC0} = \alpha_{VI0} = 10^4$ cm^{-1}. (a) $\sigma_{opt} = 10^{-14}$ cm^2. (b) $\sigma_{opt} = 10^{-16}$ cm^2.

The IBSC device structure under study will have a strong dependence on carrier transport, where photogenerated carriers in the depletion/lightly-doped region will need to drift to the n- and p-contacts prior to recombination. The carrier mobility will therefore be a crucial parameter for this device. The dependence of conversion efficiency on carrier mobility for a ZnTeO IBSC is shown in Figure 3.10 Efficiency versus carrier mobility comparing intermediate band solar cells with baseline solar cells without an intermediate band.. Solar cell conversion efficiency increases with mobility, and then approaches the ideal case where mobility is high enough for perfect charge collection. In the case of a 10 μm thick absorber region, the conversion efficiency can be much lower than the ideal case, where high mobility values would be necessary to ensure reasonable charge collection. This behavior implies the existence of an optimal base width, where shorter devices are beneficial in alleviating recombination loss while longer devices are preferred for higher optical absorbance.

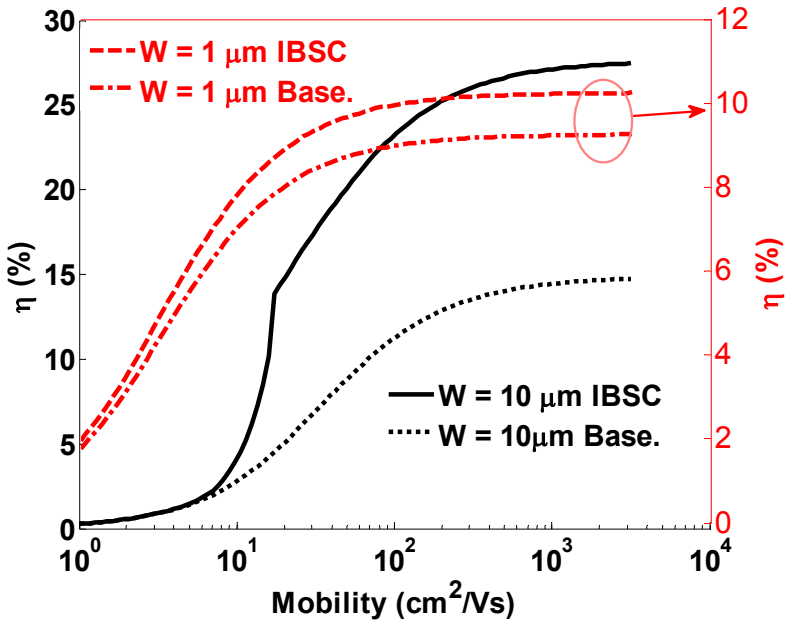

Figure 3.10 Efficiency versus carrier mobility comparing intermediate band solar cells with baseline solar cells without an intermediate band. Material and device parameters are $\alpha_{VC} = 10^4$ cm^{-1}, $E_G = 2.3$ eV, $E_I = 1.8$ eV. For $W = 1$ μm , $\alpha_{IC0} = \alpha_{VI0} = 10^3$ cm^{-1}, τ_{tot}=1 ns. For $W = 10$ μm, $\alpha_{IC0} = \alpha_{VI0} = 10^4$ cm^{-1}, τ_{tot}=10 ns.

The influence of charge collection on conversion efficiency is further illustrated by varying carrier lifetime, as shown in Figure 3.11. A kink is observed for W =10 μm curves, and its origin is still under investigation. One possible explanation is that for larger mobility, most carriers are efficiently collected and thus increasing mobility only leads to incremental increase in efficiency. In this regime, the efficiency value saturates according to optical absorption. For smaller mobility, the recombination loss is severe, and the efficiency decreases exponentially due to inefficient charge collection. The observed kink is believed to represent a crossover point associated with efficiency limited by charge collection to efficiency limited by optical absorption. The kink is not observed for shorter devices since the charge collection is not problematic, where the decease of efficiency with mobility is not as steep as W =10 μm devices. The efficiency decreases significantly with carrier lifetime, where perfect charge collection does not occur for sufficiently thick absorption width and small recombination lifetime τ_{tot}. In a realistic IBSC device, it will be difficult to obtain both full optical absorption (long base width) and perfect charge collection (high carrier lifetime and mobility where the drift length is much longer than base width). The CTR model presented provides a means of identifying and quantifying the optimal base width for an IBSC upon the establishment of physical material and device parameters.

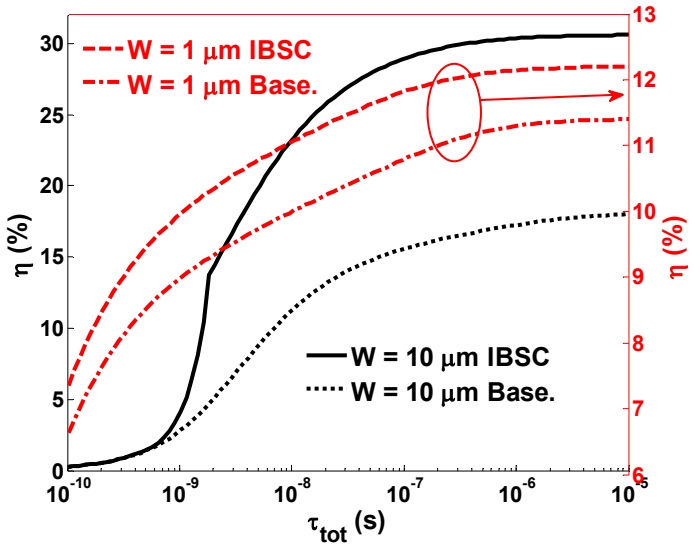

Figure 3.11 Efficiency versus total recombination lifetime comparing intermediate band solar cells with baseline solar cells without an intermediate band. Material and device

parameters are $\alpha_{VC} = 10^4$ cm^{-1}, $E_G = 2.3$ eV, $E_I = 1.8$ eV, $\mu_n = \mu_h = 100$ cm^2/Vs. For $W = 1$ μm , $\alpha_{IC0} = \alpha_{VI0} = 10^3$ cm^{-1}. For $W = 10$ μm, $\alpha_{IC0} = \alpha_{VI0} = 10^4$ cm^{-1}.

The dependence of power conversion efficiency on base width for ZnTeO (E_G = 2.3 eV, E_I = 1.8 eV) is shown in Figure 3.12 Efficiency versus base width comparing the CTR model of this work to an ideal IBSC solar cell and a baseline solar cell without an intermediate band. comparing an ideal IBSC (Luque's model [20] without CTR), a baseline ZnTe cell without IB using the CTR model, and a ZnTeO IBSC with IB using the CTR model. For the ideal IBSC, perfect charge collection is assumed, where the efficiency will increase with increasing base width W, saturating at a maximum efficiency for complete optical absorption at large W [60]. An optimal base width W is found for finite carrier mobility (CTR) associated with the tradeoff between charge collection efficiency and optical absorption. The difference between the ideal IBSC model and CTR model becomes more pronounced at large basewidth where the effect of charge collection is no longer negligible. For the prototypical IBSC in this work, the optimal base width is in the range of W~2.9 μm for $\tau_{tot} = 2$ ns and W~3.9 μm for τ_{tot}=10ns, as shown in Figure 3.12. It should be noted that the presence of a back reflector and light trapping effect could reduce the optimal base width to about half of these values. The peak conversion efficiency for Luque's model is 32.76 %. The peak conversion efficiency for IBSC using CTR model are 26.87 % and 23.29 % when total recombination life time are 10 ns and 2 ns respectively, and the peak conversion efficiency for baseline cell is 14.39 % for τ_{tot} = 10 ns and 12.34 % for τ_{tot} = 2ns.

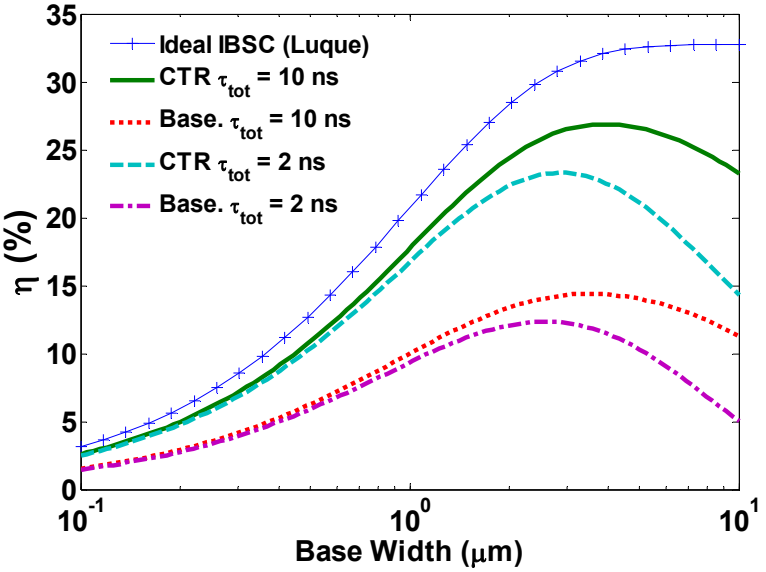

Figure 3.12 Efficiency versus base width comparing the CTR model of this work to an ideal IBSC solar cell and a baseline solar cell without an intermediate band. Material and device parameters are $\alpha_{VC} = 10^4$ cm^{-1}, $E_G = 2.3$ eV, $E_I = 1.8$ eV, $\mu_n = \mu_h = 100$ cm^2/Vs, and $\alpha_{IC0} = \alpha_{VI0} = 10^4$ cm^{-1}.

3.4 Conclusion

Carrier transport and recombinationh model (CTR) is presented to assess the effect of charge transport and collection in IBSC based on electron and hole continuity equations and IB filling factor. Calculations using this model indicate that power conversion efficiency can be much smaller than the ideal case where infinite mobility and full absorption are assumed, and provide quantitative data on the influence of these parameters. The design of IBSC devices is therefore facilitated by the CTR model allowing one to determine optimal device parameters for a given IB material. The CTR model has also identified a lifetime-dependent optimal energetic position for the intermediate band (E_I), which originates near $E_G/3$ from the band edge for large lifetime and shifts toward the conduction bandedge with decreased carrier lifetime to compensate for carrier recombination. Similarly, the CTR has been used to identify the optimal density of IB states N_I associated with the tradeoff between optical absorption and carrier lifetime. The effect of carrier transport on solar cell efficiency was determined with

varying parameters for mobility and carrier lifetime. The modeled dependence of conversion efficiency on carrier transport provides a means of determining the optimal base width W, provided material parameters of the intermediate band material (μ, τ_{tot}, α, E_G, E_I). ZnTeO is used as a prototypical IBSC example using the CTR model, where the peak conversion efficiency decreases from the theoretical, detailed balance limit value of 32.76 % to 26.87 % for a value of τ_{tot}=10ns in the CTR model, and further decreases to 23.29 % for τ_{tot}=2 ns. Comparing the conversion efficiency at optimal base width, the improvement of a ZnTeO IBSC over a baseline cell without IB is an efficiency increase from 14.39 % to 26.87 % for τ_{tot}=10 ns and from 12.34 % to 23.29 % for τ_{tot}=2 ns.

Chapter IV Spectrally Decoupled Devices

4.1 Background

Spectral overlap between different absorption processes is a fundamental problem for solar cells based on multi-photon processes, often referred to as intermediate band solar cells (IBSC) [20, 21, 23, 37, 58-68, 73, 80-83] or impurity photovoltaics (IPV) [27, 28, 84, 85]. Ideally, the incident solar photons are absorbed by the appropriate highest threshold process to minimize thermalization of photoexcited carriers. In this approach, two subbandgap photons excite an electron from the valence band (VB) to conduction band (CB) via intermediate levels and contribute to one electron–hole pair. In common semiconductor materials, there is a high density of states beyond the band edge, enabling higher energy photons to participate in lower energy optical transitions leading to undesired energy loss via carrier thermalization (Figure 4.1 (a))The resulting spectral overlap between optical transitions can span an energy range of several eV, where the efficiency of the solar cell can drop to a value below a standard solar cell without intermediate electron states [60]. The prevention of undesired optical transitions in select spatial regions in the device would reduce or eliminate problems related to spectral overlap. In this study, the influence of varied occupation of intermediate electron states is examined as a means of spatially separating sub-bandgap optical transitions. This approach is shown in (Figure 4.1(b)), where the intentional high/low occupation provides a means of preventing optical transitions into/out of the intermediate states. This approach relies on charge carrier transport via the intermediate band to transfer electrons between spatially separated absorption bands. The conversion efficiency of these structures is examined as a function of spectral overlap and compared to conventional IBSC structures and triple-junction solar cells.

4.2 The Solar Cell Model

The detailed balance approach is a self-consistent thermodynamic argument that provides an estimate on the highest efficiency that can be achieved by photovoltaic solar cells. Although the detailed balance approach does not solve the complete set of partial differential equations as described in drift-diffusion model in previous section, it can provide meaningful theoretical estimate on the upper bound of conversion efficiency achievable by a particular scheme. This study follows the prior models and associated assumptions [20, 59-62, 64-66], with the modification of a spatially dependent optical absorption coefficient based on intermediate band occupation for analysis in one dimension. Spatially dependent generation and recombination processes are then evaluated to determine integrated values of current density and corresponding conversion efficiency.

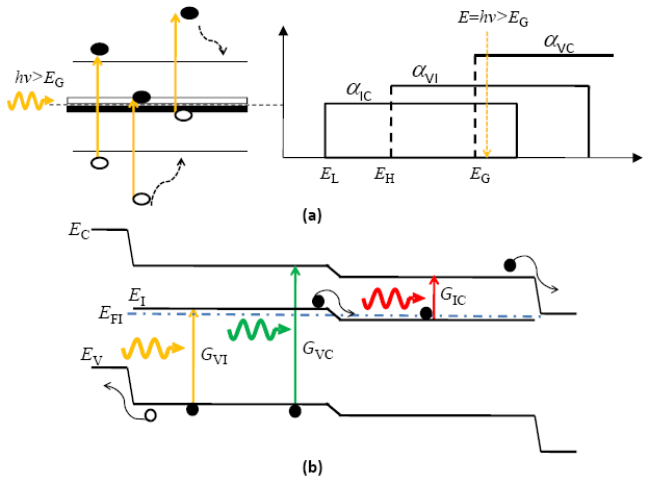

Figure 4.1 (a) illustration of spectral overlap and associated thermalization (left figure, dashed black arrows). (b) illustration of entire device structure of low-high state filling cells.

The derivation for solar cell efficiency based on intermediate band electron state occupation starts from the photon number, which may be represented by

$$\frac{d\nu}{dx} = -\alpha_{VC}(\nu-\nu_{CV}) - \alpha_{IC}(\nu-\nu_{CI}) - \alpha_{VI}(\nu-\nu_{IV}) \quad 4.1$$

$$\begin{aligned}\alpha_{\mathrm{VC}} &= \alpha_{\mathrm{VC0}} \\ \alpha_{\mathrm{IC}} &= \alpha_{\mathrm{IC0}}\zeta \\ \alpha_{\mathrm{VI}} &= \alpha_{\mathrm{VI0}}(1-\zeta)\end{aligned} \tag{4.2}$$

where α_{VC}, α_{IC}, α_{VI} are the absorption coefficient for VB to CB, IB to CB and VB to IB transitions respectively, ζ is the Asbeck factor characterizing intermediate state occupation. The assumption of the "half-filled" condition in the original derivation [20, 59-62, 66] corresponds to $\zeta = 0.5$ in this analysis. The values of ν_{XY} (X, Y = C, I , or V) are given by

$$\nu_{\mathrm{XY}} = \frac{1}{1+\exp\left(\frac{E_{\mathrm{XY}}-\mu_{\mathrm{XY}}}{kT}\right)} \tag{4.3}$$

where E is energy and $\mu_{\mathrm{XY}} = E_{\mathrm{FX}}$-$E_{\mathrm{FY}}$ is the separation between quasi-Fermi levels. It should be noted that $\mu_{\mathrm{CV}} = E_{\mathrm{FC}}$-$E_{\mathrm{FV}} = V_{\mathrm{A}}$ is the applied bias of the diode.

The photon number given in Eq.4.1 holds for the entire base region, which may be solved piecewise for the case of spatially varying absorption coefficient. The photon number at a particular location in the base region can be expressed as

$$\begin{aligned}\nu(x) = &\frac{\alpha_{\mathrm{VC}}\nu_{\mathrm{CV}} + \alpha_{\mathrm{IC}}\nu_{\mathrm{CI}} + \alpha_{\mathrm{VI}}\nu_{\mathrm{IV}}}{\alpha_{\mathrm{VC}} + \alpha_{\mathrm{IC}} + \alpha_{\mathrm{VI}}} \\ &\times\left[1-\exp^{-(\alpha_{\mathrm{VC}}+\alpha_{\mathrm{IC}}+\alpha_{\mathrm{VI}})\times(x-x_0)}\right] \\ &+\nu(x_0)\exp^{-(\alpha_{\mathrm{VC}}+\alpha_{\mathrm{IC}}+\alpha_{\mathrm{VI}})\times(x-x_0)}\end{aligned} \tag{4.4}$$

where x_0 is the boundary of the particular piecewise section of the base region. The net electron and hole generation-recombination rate can be calculated by spatial integration

$$\begin{aligned}&(G-R)_e(x) = \\ &\int_{E,\Omega}\alpha_{VC}(\nu-\nu_{CV})+\alpha_{IC}(\nu-\nu_{CI})\frac{2E^2}{h^3c^2}dEd\Omega \\ &(G-R)_h(x) = \\ &\int_{E,\Omega}\alpha_{VC}(\nu-\nu_{CV})+\alpha_{VI}(\nu-\nu_{IV})\frac{2E^2}{h^3c^2}dEd\Omega\end{aligned} \tag{4.5}$$

where $h = 6.626\times10^{-34}$ Js is Plank's constant, $c=3\times10^{8}$ m/s is the speed of light, and Ω is the solid angle. The total electron or hole current density due to generation-recombination (dominant mechanism for ideal case) can be calculated by integrating over the total basewidth W

$$J_{e,h} = \int_0^w (G-R)_{e,h}(x)dx \qquad 4.6$$

The current density is a function of the quasi-Fermi level separation μ_{CI} , μ_{IV} , and $\mu_{CV} = V_A$, where μ_{CI} and μ_{IV} can be solved by given the relation $\mu_{CI}+\mu_{IV} = \mu_{CV} = V_A$ and requirement that electron and hole current density must be balanced to maintain charge neutrality and particle conservation in the entire base region. The current density is then solved for a given applied bias V_A, where the efficiency is defined as:

$$\eta = \frac{J_{sc}\times V_{oc}\times FF}{P_{sun}} \qquad 4.7$$

where J_{sc} is the short circuit current density, V_{oc} is the open circuit voltage, $FF= J_mV_m/J_{sc}V_{oc}$ is the fill factor, J_m and V_m are the current density and voltage at the operating point where the power output from the solar cell is maximum, and P_{sun} is the incident solar power density.

In this study, the bandgap energy and intermediate band position are assigned values of E_G = 1.95 eV and E_I = 1.24 eV, respectively, based on the optimal values obtained from 0-D detailed balance calculations [58, 60]. Calculations are performed with Solar concentration at either X = 1 (one sun) or 46050 (fully concentrated sunlight) as indicated in figure captions. Values for absorption coefficients α_{VC}, α_{IC}, α_{VI} are chosen to be 10^4 cm^{-1} at the ideal half-filled IB condition, as representative values reported in previously published work [59-62, 81].

Four device structures are studied as shown in Figure 4.2 to compare the influence of spatially varying occupation of intermediate band states on spectral overlap and solar cell conversion efficiency. The first two device structures are (A) uniform absorber with half-filled (HF) IB and (B) absorber with nearly empty IB in half of the device and nearly filled in the other half of the device, assuming efficient carrier transport in the IB between the two regions. Structure (A) serves as a point of reference, while structure (B) is the primary structure under study where a base region with empty IB in one region prevents

IB to CB transitions and filled in one region prevents VB to IB transitions. Structures (C) and (D) are essentially the same as (A) and (B) respectively, but each contains an additional section without IB states to further spatially separate absorption processes. The regions without IB states are beneficial in ensuring solar photons with energy $E > E_G$ are absorbed by the VB to CB transition instead of other low-threshold processes such as the VB to IB transition. (B) is referred to as spectrally decoupled devices (SD) and (D) is referred to as full spectrally decoupled devices. It should be noted that the proposed spatially varying occupation of intermediate band states may be realized in principle by doping and control over impurity/nanostructure placement, providing spectral separation of absorption bands while maintaining a single-junction device structure.

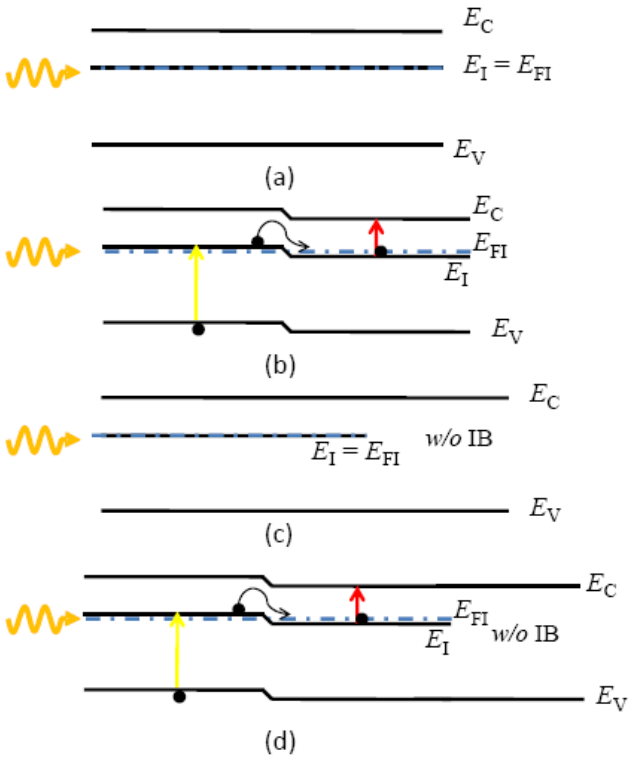

Figure 4.2 (a) HF (b) SD (c) HF+base semiconductor (d) full spectrally decoupled

4.3 Results

The current-voltage characteristics of the device structures are shown in Figure 4.3. The J_{sc} and V_{oc} for the device with half-filled IB demonstrates a clear decrease with spectral overlap E_{ov} while the decrease in J_{sc} and V_{oc} is significantly reduced for the

structure with separate low/high IB occupation regions. In structure C, photons with energy $E_H < E < E_G$ are absorbed in the first section of the device via the VB to IB transition, while photons with energy $E_L < E < E_H$ are not absorbed due to the low density of electrons available in the IB available for absorption. This configuration ensures that photons are absorbed by the highest threshold process. Photo-excited electrons may then transport to the second section of the base region to be subsequently excited to the CB by solar photons with energy $E_L < E < E_H$. For the half-filled IB device B, all photons with energy $E > E_L$ can be absorbed by the IB to CB transition where excess electron energy of $E - E_L$ is lost by phonon emission. Without spectral overlap ($E_{ov} = 0$), the intermediate band devices behave identically, where distinctions become pronounced with increasing spectral overlap.

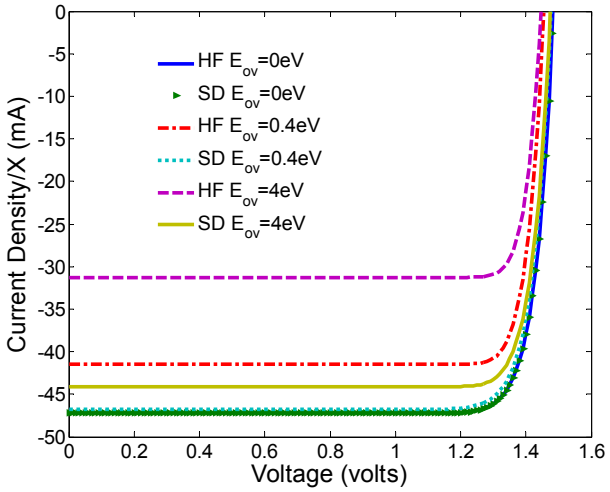

Figure 4.3 *J-V* for spectrally-decoupled cells. $(\zeta_1, \zeta_2) = (0.1,0.9)$. $W = 2$ μm. $X = 1$.

The influence of the spatially varying absorption is illustrated in Figure 4.4, where subbandgap absorption occurs selectively according to electron state occupation.

Increasing spectral overlap results in more pronounced differences in absorption, as shown in Figure 4.5. One clear characteristic is observed in Figure 4.5(a), where there is significant re-emission for the CB to IB transition. The re-emission is due to the spectral overlap, where high energy photons are absorbed by inappropriate low-threshold processes ($E_L < E < E_H$), leading to significant thermalization. The thermalized high-energy photons then recombine through low threshold CB to IB transitions, assumed to

be radiative in this analysis. The recombination rate in the context of detailed balance theory is proportional to exp(-E/kT) and thus the low-threshold CB to IB transition ($E_L < E < E_H$) is the most efficient recombination process. This is consistent with experimental observation where thermal generation-recombination is more severe in small bandgap materials. In the case of the two-region structure (B) (Figure 4.5(b)), the re-emission is suppressed since low-high IB occupation decouples the spectral overlap between α_{IC} and α_{VI}. The efficiency of structure (B) is therefore much closer to the ideal E_{ov}=0 condition even if spectral overlap is present.

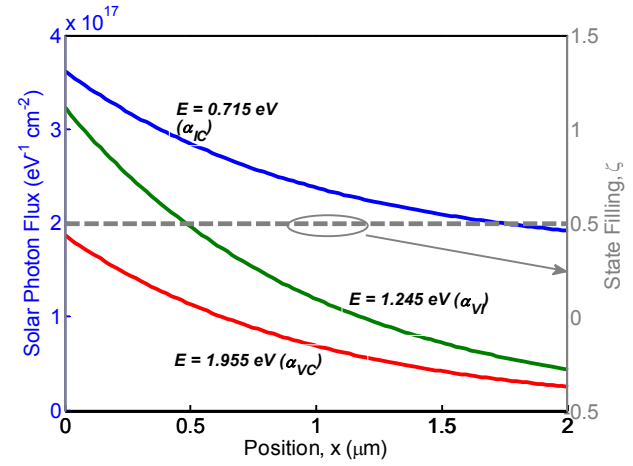

(a)

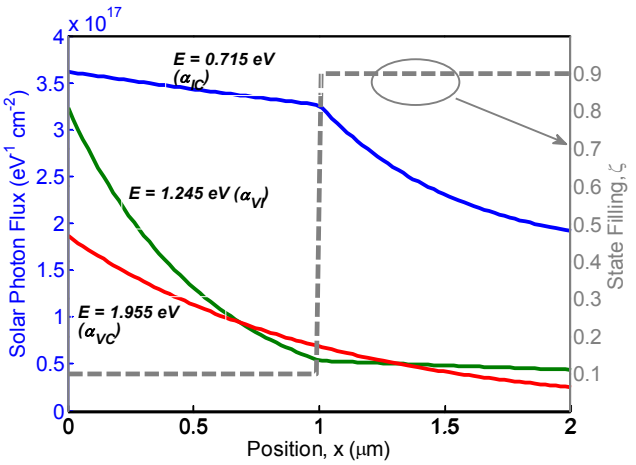

(b)

Figure 4.4 E_{ov} = 0eV, X = 1. (a) a HF device (b) a SD device with (ζ_1, ζ_2) = (0.1,0.9).The photon energy is 0.05 eV above transition threshold.

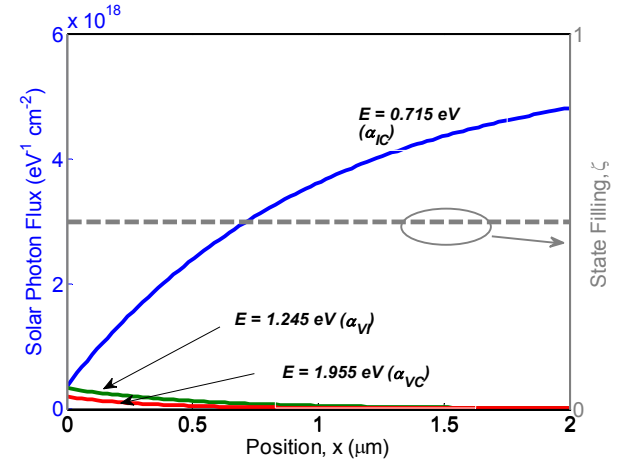

(a)

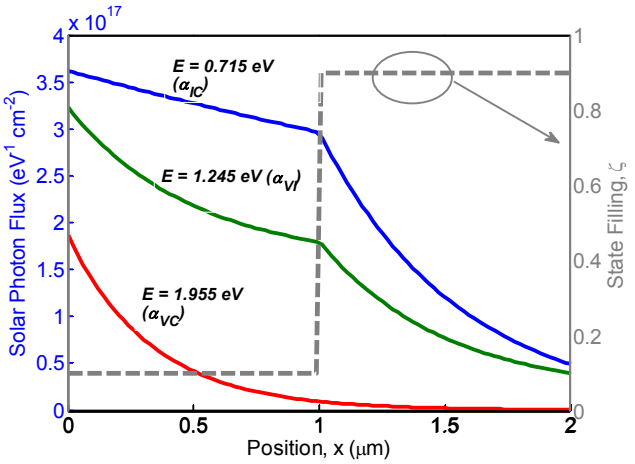

(b)

Figure 4.5 E_{ov} = 4eV, X = 1. (a) a HF device (b) a SD device with (ζ_1, ζ_2) = (0.1,0.9).The photon energy is 0.05 eV above transition threshold.

The dependence of conversion efficiency on spectral overlap (E_{ov}) more clearly illustrates the impact of spatially varying IB population, as shown in Figure 4.6. For no spectral overlap (E_{ov} = 0 eV), conversion efficiency is the same for all IBSC device structures studied since solar photons are absorbed by the highest threshold process. Device structures with a half-filled IB show a rapid decrease with increasing E_{ov} due to thermalization of photo-generated electrons or holes in the CB and VB for optical transitions excited that are not the highest possible energy transitions, similar to calculations reported in previously published work [60]. An anomaly in the figure is that the efficiency of both HF and SD devices increases with E_{ov} for short basewidth due to

more absorption resulting from spectral overlap. The efficiency for device structures with variable intermediate band occupation shows a significantly lower sensitivity to spectral overlap and higher efficiency compared to their HF counterparts.

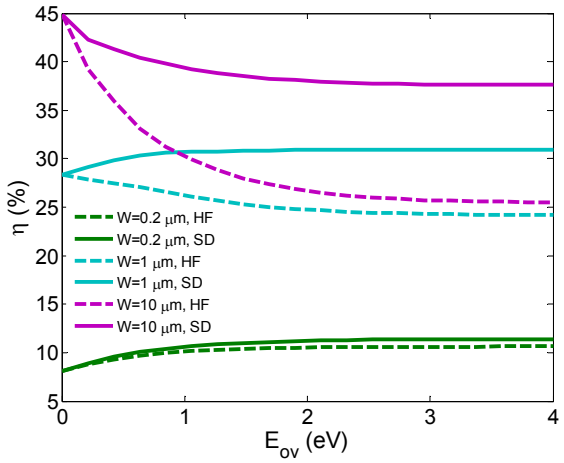

Figure 4.6 η vs E_{ov} for varying W_{tot}. $(\zeta_1, \zeta_2) = (0.1,0.9)$.$X = 1$.

The dependence of efficiency on the occupation level of the IB states is clearly an important factor, as shown in Figure 4.7 for device structure (C). In the analysis, IB occupation is assumed to be symmetric in the two regions such that $\zeta_2 = 1-\zeta_1$. It is clear that the contrast in occupation for the two regions (ζ_1,ζ_2) =(0.1,0.9) is sufficient to achieve high efficiency, where only small improvements are achieved beyond these values. High occupation in the first section of the base region ($\zeta_1 > 0.5$) corresponds to high absorption of the low energy transition nearest the incident surface, resulting in a decrease in efficiency to below the value for the case of a half-occupied IB due to increased thermalization losses. This behavior is similar to the requirement for multi-junction cells where incidence at the large bandgap side is required.

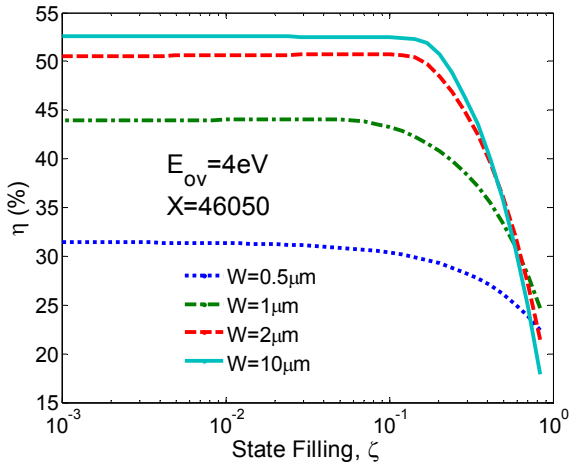

Figure 4.7 η vs ζ. for varying W , E_{ov} = 4eV. X = 46050.

The dependence of conversion efficiency on base width is shown in Figure 4.8 for the various device structures. The full spectrally decouple device (D) is essential to further increasing the efficiency toward the E_{ov}=0 efficiency limit to eliminate the spectral overlap still present between α_{IC} (or α_{VI}) and α_{VC}. In the structure (D), the three regions of the device completely separate/decouple the three absorption bands to minimize thermalization losses. The highest efficiencies calculated in Figure 4.8 are 35.1% for structure (A), 45.0% for structure (B), 52.83% for structure (C), and 61.5% for structure (D) (referred to Figure 4.2). It should be noted that the efficiency is calculated to be 63.2% for the ideal IBSC [20], 63.8 % for the unconstrained triple--junction tandem cell [86], and 63.2 % for the series constrained triple-junction tandem cell [87]. The fully decoupled structure (D) provides a theoretical efficiency limit >60% that approaches the efficiency limit of both the ideal IBSC and triple-junction solar cell. The spectrally decoupled structure essentially provides a "triple-band" structure analogous to a triple-junction solar cell, while maintaining a single-junction device.

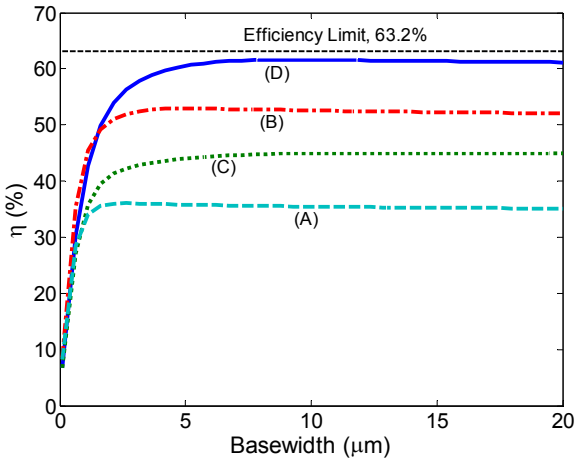

Figure 4.8 η vs W. for varying scheme (ζ_1, ζ_2) = (0.01,0.99) for SD and full spectrally decoupled scheme. E_{ov} = 4eV. X = 46050.

4.4 Practical Implementation of Low-High State Filling

The absorber layer structure with non-uniform intermediate band occupation may be implemented in practice by variable doping levels. The electrostatic potential (ψ) is affected by several different charge contributions:

$$\vec{\nabla}\cdot\varepsilon_r\varepsilon_0\vec{\nabla}\psi = -q\left(N_D^+ - N_A^- - n + p - \zeta N_I\right) \qquad 4.8$$

The Poisson equation for electrostatic potential (ψ) includes the charge density for electrons (n), holes (p), ionized acceptors (N_A^-), ionized donors (N_D^+), and charge in the intermediate band represented by the occupation of states (ζ) and concentration of intermediate band states (N_I), ε_r is relative permittivity and ε_0 = 8.84×10^{-12} F/m is the permittivity in vacuum. In this calculation, N_I = 10^{19} cm^{-3}, ε_r = 10, basewidth W = 2 μm, and the width for p- and n- contact layers are 0.3 μm with heavy doping concentration of 10^{19} cm^{-3}. The IB are assumed to lie at a fixed energy level in the bandgap. Alternative density of states functions with IB states distributed in energy may be similarly defined. The doping profile and resulting occupation of IB states are shown in Figure 4.9, where the n-type doping profile in the base region is varied for three cases of $0.5N_I$ (half-filled), ($0.1N_I$, $0.9N_I$), and ($0.01N_I$, $0.99N_I$). The resulting energy band diagram is shown in Figure 4.10, where only small variation in potential energy results in large variation in IB

occupation as a result of the exponential dependence of occupation on potential according to Fermi-Dirac statistics. The energy band profile is very similar to IB devices with half-filled IB and flat band region in the base region, implying a minimal effect of variable IB occupation of these device structures on carrier transport in the base region.

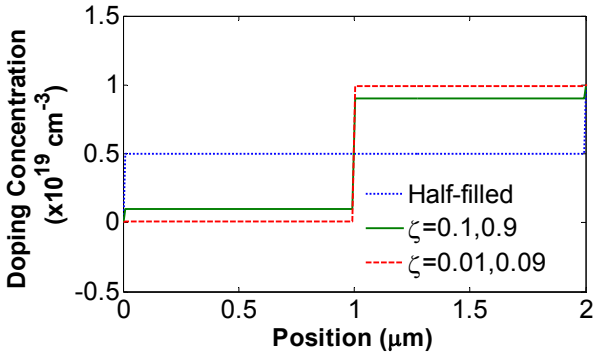

(a)

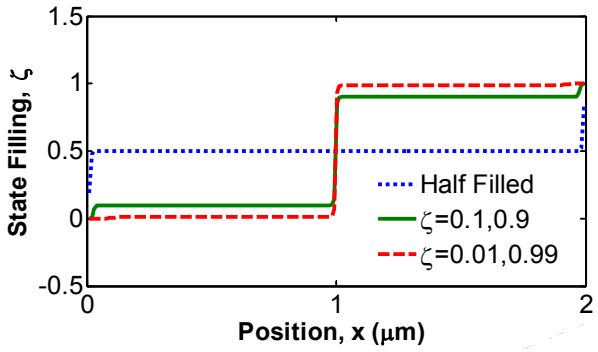

(b)

Figure 4.9 (a) Doping vs position (b) ζ vs position

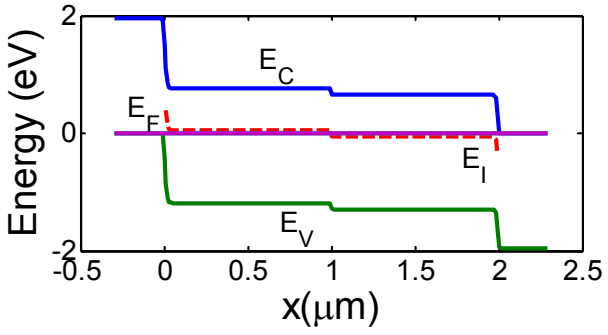

(a)

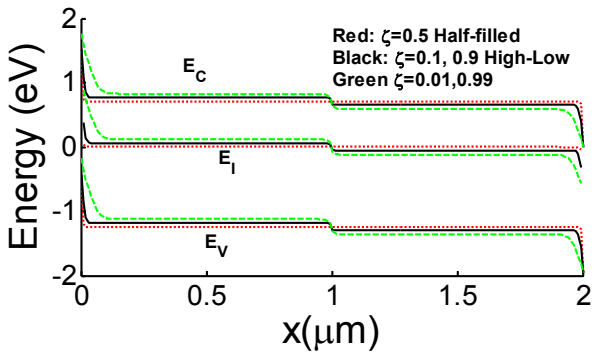

(b)

Figure 4.10 (a) Band diagram of entire device (b) band diagram for varying ζ at base region

4.5 Conclusion

The efficiency of a device spatially decoupling VB-IB and IB-CB absorption by defining a non-uniform occupation of IB states is calculated to be 52.8% for the case of significant spectral overlap between bands. This efficiency is significantly higher than the efficiency of 35.1% calculated for devices with IB states at uniform 50% occupation. A full spectral decoupling scheme for CB-VB, VB-IB, and IB-CB transitions may further increase the conversion efficiency, where a value of 61.5% is calculated for the case of 4 eV spectral overlap, approaching the detailed balance efficiency limit of 63.2 % for IBSC devices with no spectral overlap. The success of this approach is reliant on the ability to spatially vary IB occupation by doping or other mechanisms, and to realize efficient transport via the IB. These two challenges are identified as key areas of future experimental research to enable high-efficiency IBSC devices.

Chapter V The Drift-Diffusion Model of Intermediate Band Solar Cell

5.1 Introduction

Since the original detailed balance 0-D model [20] for intermediate band solar cells (IBSC), further efforts have been published to enhance the understanding of this device, including the effect of intermediate band position and spectral overlap [60, 62], Auger generation [63, 67], thermodynamic consistency of subbandgap photovoltaic [66], quasi-drift-diffusion modeling [61], and equivalent circuit modeling [65]. Thusfar, experimental data has not confirmed the high conversion efficiency expected for the IBSC approach, where both the open circuit voltage (V_{oc}) and short circuit current density (J_{sc}) have been measured to be less than a single junction cell without an intermediate band [21, 23, 82]. Existing 0-D detailed balance models do not provide an adequate framework to explain this experimental behavior, and also do not adequately incorporate physical processes for device design. In previous chapter, a semi-one-dimensional modeling incorporating charier transport and recombination is presented. The results provide insight into the operation of IBSC and make clear the need of a truly 1-D model. The development of a 1-D drift-diffusion model would enable the design, optimization, and interpretation of IBSC by incorporating material and device parameters including generation-recombination, carrier transport, device dimensions, and doping profiles. Conventional drift diffusion models for semiconductors only describe generation-recombination through trap states [27, 28], and do not provide a straightforward means of incorporating electron states corresponding to an intermediate band. Furthermore, convergence for conventional drift-diffusion numerical models becomes highly difficult

when the concentration of IB states becomes larger than the background doping concentration of the host semiconductor material. Conventional simulation normally employs non-radiative Shockley Read Hall formulation while radiative transitions associated with the IB are generally not available in commercial and custom semiconductor drift-diffusion software packages.

5.2 The Conventional Drift-Diffusion Model and Impurity Photovoltaic Effect

5.2.1 The Formulation of Conventional Drift Diffusion Model

The conventional drift-diffusion model basically contains three equations governing the electrostatic potential, electron and hole continuity.

$$\vec{\nabla} \cdot \varepsilon_r \varepsilon_0 \vec{\nabla} \psi = q\,(N_{\mathrm{A}}^{-} - N_{\mathrm{D}}^{+} + n - p) \qquad 5.1.a.$$

$$\vec{\nabla} \cdot \vec{J}_{\mathrm{n}} = q(G - R) \qquad 5.1.b.$$

$$\vec{\nabla} \cdot \vec{J}_{\mathrm{p}} = q(G - R) \qquad 5.1.c.$$

The solution process consists of discretization of differential equations into difference equations, and then using the Newton-Raphson technique to iterate the variables until the roots of the equations are found. Fully coupled Newton method or decoupled Gummel iteration can be employed. The former method provides faster convergence and more relaxed constraint on bias stepping, with the shortcomings of significantly higher demand on memory, while the later provides efficient usage of memory demand, with the shortcomings of slow convergence especially at elevated bias.

5.2.2 The Formulation for Impurity Photovoltaic Effect: Modified Shockley-Read-Hall Recombination

The trap charge can be influential to the electrostatic potential, and thus should be included in the Poisson equation explicitly:

$$\vec{\nabla} \cdot \varepsilon_r \varepsilon_0 \vec{\nabla} \psi = q\,(N_{\mathrm{A}}^{-} - N_{\mathrm{D}}^{+} + n - p + n_{\mathrm{t}}) \qquad 5.2$$

ε_{r} is relative permittivity, ε_0 is permittivity in vacuum, q is the fundamental charge, ψ is potential N_{A}^{-} is ionized acceptor concentration, N_{D}^{+} is ionized donor concentration, n is electron concentration, p is hole concentration, and n_{t} is the electron concentration in the trap states. It should be noted that the trap states can be donor-like or acceptor-like. In the first case, the state carries a positive charge when empty and being neutral when filled with an electron. In the second situation, the state carries a negative charge when filled with an electron and being neutral when empty. The Poisson equation in Eq.5.2 is under the assumption of acceptor-like states. For the donor-like states, the equation has to be modified to

$$\vec{\nabla} \cdot \varepsilon_r \varepsilon_0 \vec{\nabla} \psi = q\,(N_{\mathrm{A}}^{-} - N_{\mathrm{D}}^{+} + n - p - (N_t - n_{\mathrm{t}})) \qquad 5.3$$

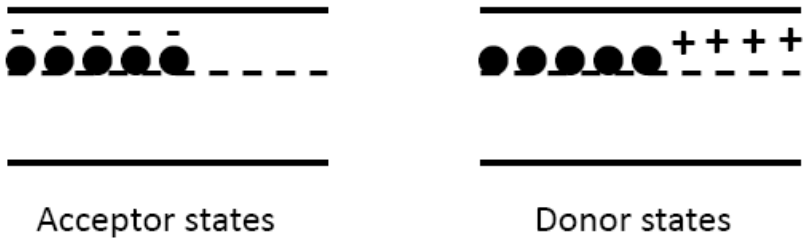

Figure 5.1 Acceptor and donor states

The optical generation from the trap states can be modeled according to the Shockley-Read-Hall (SRH) formulation:

$$\begin{aligned} r_{\mathrm{nt}} &= c_{\mathrm{n}} n (N_{\mathrm{t}} - n_{\mathrm{t}}) - e_{\mathrm{n}} n_{\mathrm{t}} \\ r_{\mathrm{pt}} &= c_{\mathrm{p}} p n_{\mathrm{t}} - e_{\mathrm{p}} n_{\mathrm{t}} (N_{\mathrm{t}} - n_{\mathrm{t}}) \\ g_{\mathrm{nt}} &= e_{\mathrm{n,opt}} n_{\mathrm{t}} \\ g_{\mathrm{pt}} &= e_{\mathrm{p,opt}} (N_{\mathrm{t}} - n_{\mathrm{t}}) \end{aligned} \qquad 5.4.a.$$

$$r_{\mathrm{nt}} - g_{\mathrm{nt}} - r_{\mathrm{pt}} + g_{\mathrm{pt}} = 0 \qquad 5.4.b.$$

Eq 5.4.b states the generation-recombination rate has to balance itself locally, where r_{nt} is thermionic emission rate of electrons, r_{pt} is thermionic emission rate of holes, g_{nt} is the optical generation rate of electrons, and g_{pt} is optical generation rate of holes, C_{n} and C_{p} are capture coefficient for electrons and holes, and e_{n} and e_{p} are emission coefficient for electrons and holes respectively, and N_{t} is the trap concentration.

5.2.3 Result for Impurity Photovoltaic Effect

[27, 28]Band diagram of the p-n junction with uniform distributed trap states show a strong space charge effect. The built-in potential is significantly reduced in the case of trap density equal to or higher than the base doping concentration. The open circuit voltage is thus degraded while the short circuit current is increased due to the additional generation from localized trap states. To contrast V_{oc} reduction, heavy doping in the p- and n- emitters may be used to clamp the built-in potential [27]. The increase in J_{sc} is limited by the density of trap states. Since the trap density cannot be very high, due to the consideration of non-radiative recombination and practical limitation of impurity incorporation, the benefit of the impurity photovoltaic effect is restricted. On the other hand, intermediate band photovoltaics is normally referred to devices where impurity concentration is much higher and the radiative processes dominate. The intermediate band photovoltaics is thus a more promising route toward ultra high efficiency solar cells.

5.3 The Drift-Diffusion Model of Intermediate Band Solar Cell

5.3.1 Background

Since the original detailed balance 0-D model [20], various continued efforts and improvements have been made including the effect of intermediate band position and overlapping [60, 62], investigation of low threshold Auger generation [63, 67], equivalent circuit modeling [65], the thermodynamic consistency of subbandgap photovoltaics [66], quasi-drift-diffusion model [61]. Some attempts have also been made to link between conventional semiconductor device modeling and IBSC theory which somewhat differs from the framework of widely accepted drift-diffusion model for semiconductor devices in which the variable is n, p, ψ, rather than μ_{CI}, μ_{IV} [23, 59]. It is desirable to have a drift-diffusion model to facilitate the device design and optimization, gain deeper insight into the operation of the intermediate band device, and link between conventional semiconductor device modeling and recently proposed IBSC models. To date there has not been any reported experimental work that has confirmed high efficiency for IBSC. Experimental reports show that both the V_{oc} and J_{sc} of the IBSC are lower than the baseline cell, while in some other cases J_{sc} indeed increases though the V_{oc} is significantly

lower than the baseline cell. The 0-D detailed balance model is not convincing since it is an idealized and simplified approach, where it is important to regain the confidence for IB photovoltaics and verify the result of the 0-D model by a more realistic 1-D drift-diffusion model. The 1-D drift-diffusion model also enables the design and optimization by assessing the various physical effects on the device performance, such as non-radiative recombination, doping, and device dimensions.

In the Quasi-Drift-Diffusion model [61], the electron and hole continuity equations are solved while the Poisson equation is neglected in the modeling, where the effect of space charge and its effect on the electrostatic potential are ignored. This also leads to the mathematical relation between the carrier concentration and quasi-Fermi potential, and the boundary conditions have to be modified and deviate from conventional drift diffusion models. The neglect of the Poisson equation also prevents the possibility of full device simulation, which should include *p*- and *n*- emitter and base region. In addition, the diffusion current is assumed to be dominant in the charge collection absorber region, which may only be true under select conditions. The effect of intermediate band filling cannot be shown explicitly in this model, where the assumption of a half filled intermediate band cannot be justified. In the complete drift diffusion model presented in this chapter, it is verified that the half-filled IB can be achieved with compensated base doping. One of another assumption made either proposed along the line of original IBSC theory or used in quasi-drift-diffusion model is that the quasi-Fermi level for the IB (E_{FI}) is pinned at its equilibrium position, and since the half filled IB is assumed, this position coincides with the position of the IB (E_I). This results in a relationship between the electron and hole quasi-Fermi levels and electron and hole concentrations that can be arranged into the form depending on μ_{CI}, μ_{IV}, deviating from widely accepted semiconductor carrier statistics. In our drift-diffusion model, it is shown that with compensated base doping, the pinning of E_{FI} at E_I can be achieved, though this may not be true in all situations.

In 2006, the formulation of a modified SRH recombination theorem was presented to explain the physics of IB photovoltaic devices [23]. The Poisson equation is solved, while the electron and hole continuity equations are ignored with the assumption of flat electron and hole quasi-Fermi level in the base absorber region. The modified SRH

formulation is typically used for impurity photovoltaic cells (IPV) where donor or acceptor-like states are intentionally added to the base semiconductor. The calculation results match authors' group's experimental results quite well, although the results show that the incorporation of IB only degrades the V_{oc} while J_{sc} is nearly the same as baseline cell.

AIthough it is desirable to have states within the fundamental bandgap to increase J_{sc}, this may be accompanied by a decrease in V_{oc} due to reduced built-in potential (V_{bi}) or increased recombination. For the issue of reduced V_{bi}, highly doped material without intermediate band to achieve clamping of V_{oc}. In our drift-diffusion model, it is verified that this structure is indeed capable of clamping V_{oc} at a value as high as the baseline cell without intermediate band. This is of theoretical importance since most experimental work to date shows decreased V_{oc} in comparison to a baseline cell. Our work suggests in principle V_{oc} should be able to be kept as high as baseline cell from the electrostatic potential point of view while the degraded V_{oc} should result from other sources such as non-radiative recombination, coming from excess defects introduced by the incorporation of intermediate band.

In the following model, formulation for radiative transitions along the line of Luque's original paper [20] is used and the result shows that IBSC may lead to high efficiency for optimized device parameters.

5.3.2 The Formulation

The drift diffusion model generally consists of the Poisson equation, electron and hole continuity equations. The various generation-recombination terms include the IB <-> CB, VB <-> CB, VB <-> IB transitions. The charge in the intermediate band will also affect the electrostatic potential and thus the band bending. This is modeled by the last term on the right hand side of the Poisson equation below,

$$\vec{\nabla} \cdot \varepsilon_r \varepsilon_0 \vec{\nabla} \psi = q\,(N_A^- - N_D^+ + n - p - fN_I) \qquad 5.5.a.$$

$$\vec{\nabla} \cdot \vec{J}_n = q\left(G_{VC} + G_{IC} - R_{CV} - R_{CI} - R_{nr}\right) \qquad 5.5.b.$$

$$\vec{\nabla} \cdot \vec{J}_p = q\left(G_{VC} + G_{VI} - R_{CV} - R_{IV} - R_{nr}\right) \qquad 5.5.c.$$

where ψ is electrostatic potential, n and p are electron and hole concentration, f is the filling of the intermediate band, and N_I is the IB density of states. The electron and hole current equations consist of both drift and diffusion components:

$$J_n = -qD_n \frac{dn}{dx} - q\mu_n nF \qquad 5.6.a.$$

$$J_p = -qD_p \frac{dp}{dx} + q\mu_p pF \qquad 5.6.b.$$

Where F is electric field. Both drift and diffusion components are important and cannot be ignored since in certain circuimstances, large electric fields may exist in the absorber base region where drift is the dominant transport mechanism while in other situations there may be a flat band region where diffusion current is dominant. This also depends on the device length since for longer devices the total depletion of the base region is not achievable. In the quasi-neutral p- and n- emitter layers, only diffusion current needs to be taken into account while drift field dominates near emitter/base interface and sweeps the carriers out of the depletion region. Consequently, for carrier transport over the complex band profile of the entire device, it is not appropriate to ignore any of these two current components. This may become clearer when the simulation result for devices with different base doping schemes are shown in the following sections.

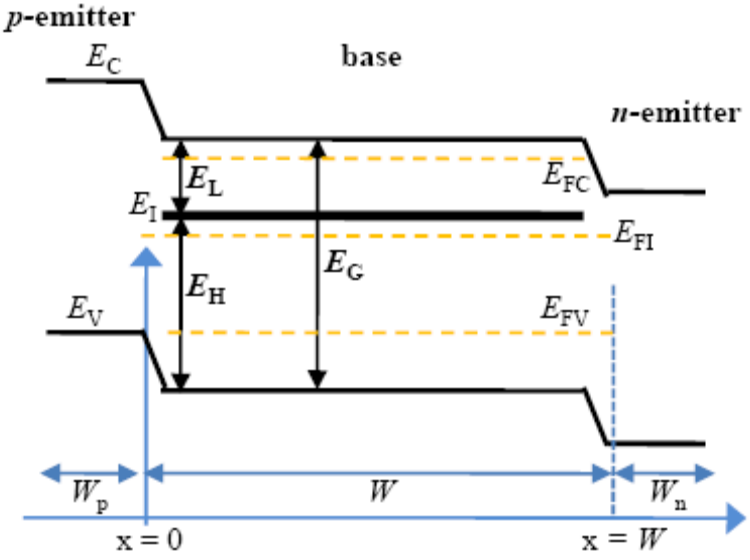

Figure 5.2 Illustration of the prototype intermediate band solar cell device structure and energy band diagram.

The states in the intermediate band also assume Fermi-Dirac statistics [23]:

$$f = \frac{1}{\exp(\frac{E_{\mathrm{I}} - E_{FI}}{kT}) + 1} \qquad 5.7$$

where E_{I} is IB energy position and E_{FI} IB quasi-Fermi level. The three optical transition mechanisms are given by:

$$G_{\mathrm{VC}} = \frac{2\pi}{h^3 c^2} \int_{E_{\mathrm{G}}}^{\infty} \frac{X f_s}{\exp(\frac{E}{kT_{\mathrm{sun}}}) - 1} \alpha_{\mathrm{VC}} exp^{-\alpha_{\mathrm{tot}} x} E^2 dE \qquad 5.8.a.$$

$$G_{\mathrm{IC}} = \frac{2\pi}{h^3 c^2} \int_{E_{\mathrm{L}}}^{E_{\mathrm{H}}} \frac{f_s}{\exp(\frac{E}{kT_{\mathrm{sun}}}) - 1} \alpha_{\mathrm{IC}} exp^{-\alpha_{\mathrm{tot}} x} E^2 dE \qquad 5.8.b.$$

$$G_{\mathrm{VI}} = \frac{2\pi}{h^3 c^2} \int_{E_{\mathrm{H}}}^{E_{\mathrm{G}}} \frac{X f_s}{\exp(\frac{E}{kT_{\mathrm{sun}}}) - 1} \alpha_{\mathrm{VI}} exp^{-\alpha_{\mathrm{tot}} x} E^2 dE \qquad 5.8.c.$$

where E is energy, f_{s} = 1/46050 is the solid angle subtended by the sun, X is solar concentration, α_{IC}, α_{VI}, α_{VC} are absorption coefficients for IB to CB, VB to IB, and VB to CB, respectively, and $\alpha_{\mathrm{tot}} = \alpha_{\mathrm{IC}} + \alpha_{\mathrm{VI}} + \alpha_{\mathrm{VC}}$. Under non-degenerate approximation, the recombination rate from conduction to valence band can be written as:

$$
\begin{aligned}
R_{\mathrm{CV}} &= \frac{2\pi}{h^3 c^2} \int_{E_{\mathrm{G}}}^{\infty} \left(\frac{1}{\exp(\frac{E-\mu_{\mathrm{CV}}}{kT})-1} - \frac{1}{\exp(\frac{E}{kT})-1} \right) \\
&\qquad \times \alpha_{\mathrm{VC}} \exp^{-\alpha_{\mathrm{tot}} x} E^2 dE \\
&= \left(\frac{2\pi}{h^3 c^2} \int_{E_{\mathrm{G}}}^{\infty} \exp(\frac{-E}{kT}) \alpha_{\mathrm{VC}} \exp^{-\alpha_{\mathrm{tot}} x} E^2 dE \right) \\
&\qquad / n_i^2 \times \left(n_i^2 \exp(\frac{\mu_{\mathrm{CV}}}{kT}) - n_i^2 \right) \\
&= B_r \left(n_i^2 \exp(\frac{\mu_{\mathrm{CV}}}{kT}) - n_i^2 \right) \\
&= B_r \left(np - n_i^2 \right)
\end{aligned}
\qquad 5.9
$$

where B_{r} is the radiative band to band recombination coefficient as in conventional semiconductor device modeling [27, 61].

It has been shown that the non-degenerate approximation works well beyond the operation point [59] in the case of 0-D modeling. In our drift-diffusion model result, it actually works far beyond the open circuit condition. In the detail balanced formulation, E actually extends from E_{G} to infinity, though it is illustrative using E_{G} as the worst case study, and at open circuit condition, $V_{\mathrm{A}} = V_{\mathrm{oc}}$, the non-degenerate approximation is still very accurate where the difference between Boltzman and Fermi-Dirac approximation is negligible (= 5.4×10^{-7} %). The approximation can become inaccurate as the bias is increased further, though as far as efficiency calculation is concerned, the validity of the approximation from short circuit condition to operating point is more than satisfactory. The recombination rates associated with the IB are given by

$$
\begin{aligned}
R_{\mathrm{CI}} &= \frac{2\pi}{h^3 c^2} \int_{E_{\mathrm{L}}}^{E_{\mathrm{H}}} \left(\frac{1}{\exp(\frac{E-\mu_{\mathrm{CI}}}{kT})-1} - \frac{1}{\exp(\frac{E}{kT})-1} \right) \\
&\qquad \times \alpha_{\mathrm{IC}} \exp^{-\alpha_{\mathrm{tot}} x} E^2 dE
\end{aligned}
\qquad 5.10.a.
$$

$$R_{\mathrm{IV}} = \frac{2\pi}{h^3 c^2} \int_{E_{\mathrm{H}}}^{E_{\mathrm{G}}} \left(\frac{1}{\exp(\frac{E-\mu_{\mathrm{IV}}}{kT})-1} - \frac{1}{\exp(\frac{E}{kT})-1} \right) \times \alpha_{\mathrm{VI}} \exp^{-\alpha_{\mathrm{tot}} x} E^2 dE \qquad 5.10.b.$$

Notice that the formulation for R_{CI} and R_{IV} are dependent on μ_{CI}, μ_{IV}, and some mathematical manipulation is necessary to transform the variables to n and p:

$$\begin{aligned} R_{\mathrm{CI}} &= \frac{2\pi}{h^3 c^2} \int_{E_{\mathrm{L}}}^{E_{\mathrm{H}}} \left(\frac{1}{\exp(\frac{E-\mu_{\mathrm{CI}}}{kT})-1} - \frac{1}{\exp(\frac{E}{kT})-1} \right) \times \alpha_{\mathrm{IC}} \exp^{-\alpha_{\mathrm{tot}} x} E^2 dE \\ &= R_{\mathrm{CI},0}[\exp(\frac{\mu_{\mathrm{CI}}}{kT})-1] \\ &= R_{\mathrm{CI},0}[\exp(\frac{E_{\mathrm{FC}}-E_{\mathrm{FI}}}{kT})-1] \\ &= R_{\mathrm{CI},0}[\exp(\frac{E_{\mathrm{C}}-E_{\mathrm{FI}}}{kT}) \times n / N_{\mathrm{c}} - 1] \end{aligned} \qquad 5.11.a.$$

$$\begin{aligned} R_{\mathrm{VI}} &= \frac{2\pi}{h^3 c^2} \int_{E_H}^{E_G} \left(\frac{1}{\exp(\frac{E-\mu_{\mathrm{IV}}}{kT})-1} - \frac{1}{\exp(\frac{E}{kT})-1} \right) \times \alpha_{\mathrm{VI}} \exp^{-\alpha_{\mathrm{tot}} x} E^2 dE \\ &= R_{\mathrm{VI},0}[\exp(\frac{E_{\mathrm{FI}}-E_{\mathrm{V}}}{kT})-1] \\ &= R_{\mathrm{VI},0}[\exp(\frac{E_{\mathrm{FI}}-E_{\mathrm{FV}}}{kT})-1] \\ &= R_{\mathrm{VI},0}[\exp(\frac{E_{\mathrm{FI}}-E_{\mathrm{V}}}{kT}) \times p / N_{\mathrm{v}} - 1] \end{aligned} \qquad 5.11.b.$$

Where E_{c} is conduction band energy and E_{v} is valence band energy. E_{FC} and E_{FV} are electron and hole quasi-Fermi levels. N_{c} and N_{v} are electron and hole effective density of states. The Boltzman statistics are used in the above derivation where the electron and hole concentrations and quasi-Fermi levels assume the following relation

$$n = N_C \exp(\frac{E_{FC} - E_C}{kT}) \tag{5.12.a.}$$

$$p = N_V \exp(\frac{E_V - E_{FV}}{kT}) \tag{5.12.b.}$$

It is worth noting that this differs from the proposed formulation in earlier papers [59-61], where the assumption of pinning of E_{FI} at equilibrium position is made in order to make the IBSC drift diffusion model consistent with the conventional one.

$$\begin{aligned} n &= N_C \exp(\frac{E_{FC} - E_C}{kT}) \\ &= \left[N_C \exp(\frac{E_{FI} - E_C}{kT}) \right] \exp(\frac{E_{FC} - E_{FI}}{kT}) \\ &= n_0 \exp(\frac{E_{FC} - E_{FI}}{kT}) = n_0 \exp(\frac{\mu_{CI}}{kT}) \end{aligned} \tag{5.13.a.}$$

$$\begin{aligned} p &= N_V \exp(\frac{E_V - E_{FV}}{kT}) \\ &= \left[N_V \exp(\frac{E_V - E_{FI}}{kT}) \right] \exp(\frac{E_{FI} - E_{FV}}{kT}) \\ &= p_0 \exp(\frac{E_{FI} - E_{FV}}{kT}) = p_0 \exp(\frac{\mu_{IV}}{kT}) \end{aligned} \tag{5.13.b.}$$

In the derivation of Eq. 5.13.a and Eq. 5.13.b, E_{FI} is assumed to be constant in order to factor out n_0 and p_0. The generation and recombination via intermediate band has to balance according to

$$R_{VI}(E_{FI,}p,x) - G_{IV}(x) = R_{CI}(E_{FI},n,x) - G_{IC}(x) \tag{5.14}$$

Notice the above equation implies that the intermediate band carrier transport is ignored [23]. In this model, we assume that the intermediate band current is negligible compared to conduction and valence band current [23]. Eq. 5.14 together with three equations (Poisson, electron and hole continuity equations) coming from conventional semiconductor device modeling are sovled using coupled Newton's method.

Finally, the SRH recombination is assumed to be the dominant non-radiative recombination mechanism in the semiconductor:

$$R_{\mathrm{SRH}} = \frac{np - n_{\mathrm{i}}^2}{\tau_{\mathrm{p}}(n + n_1) + \tau_{\mathrm{n}}(p + p_1)}$$
$$n_1 = n_{\mathrm{i}} \exp\left(\frac{E_{\mathrm{t}} - E_{\mathrm{i}}}{kT}\right) \qquad 5.15$$
$$p_1 = n_{\mathrm{i}} \exp\left(\frac{E_{\mathrm{i}} - E_{\mathrm{t}}}{kT}\right)$$

where n_{i} is intrinsic carrier concentration, E_{t} is the trap energy position, and E_{i} is intrinsic Fermi energy. The electron and hole lifetimes are assumed to be equal here for simplicity, where the trap level E_{t} is assumed to coincide with intrinsic Fermi level E_{i} as in conventional silicon device simulations where the traps are assumed to be near mid-gap. This can be regarded as a worst case assessment for the effect of non-radiative recombination on the efficiency since the SRH is most efficient when $E_{\mathrm{t}} = E_{\mathrm{i}}$. Figure 5.3 illustrates the solution process of drift-diffusion model.

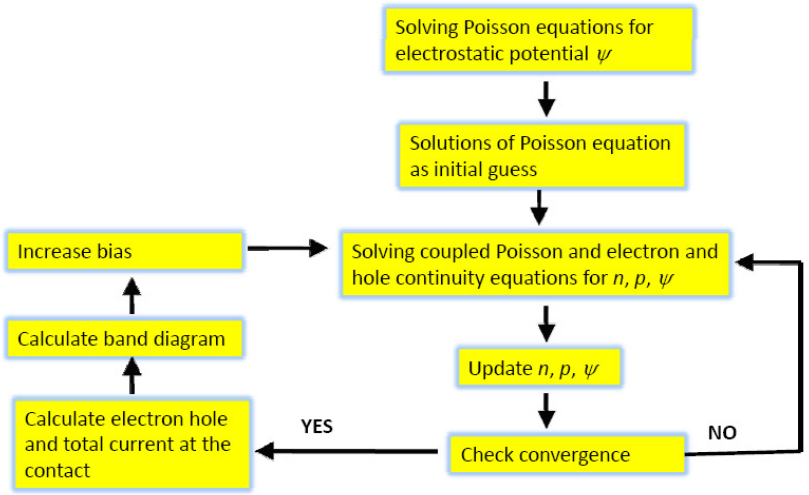

Figure 5.3 Illustration of the solution process

Other recombination mechanisms can be easily incorporated into the model without difficulty since the formulation depends on ψ, n, and p rather than μ_{CI} and μ_{IV}. Ohmic contact are assumed for boundary conditions, where the carrier concentration is at the equilibrium value. The parameters used in our simulation are summarized in the Table 5-1. The E_{G} = 1.95 eV and E_{I} = 1.24 eV is chosen according to the optimal value from 0-D detail balanced calculation [60].

Table 5-1 Simulation parameters

Band gap Energy E_G	1.95 eV
IB Energy position E_I	1.24 eV
Mobility μ_n, μ_p	100 cm^2/Vs
IB density of states N_I	10^{18} cm^{-3}
p-emitter doping N_A	10^{18} cm^{-3}
n-emitter doping N_D	10^{18} cm^{-3}
Effective density of states N_C, N_V	10^{19} cm^{-3}
Solar concentration X	1
Lattice temperature T	300 K
Solar temperature T_s	5963 K
Relative permittivity ε_r	10
p- and n- emitter width W_p, W_n	0.3 μm
Absorption coefficient α_{VC}, α_{IC}, α_{VI}	10^4 cm^{-1}

5.3.3 Lightly Doped Case

Initial simulations were conducted for an IBSC with uniform absorber layer n-type doping of $N_D=10^{14}$ cm^{-3} and base width of W=1 μm. The calculated band diagram for this device is shown in Figure 5.4 and the generation and recombination rates are shown in Figure 5.5. The band diagram deviates from a conventional *p-i-n* (or similar *p-π-n*, *p-υ -n*) device where the energy band profile variation is nearly linear in the *i* (π, υ) region. The nonlinear profile for the IBSC is a result of the spatial variation of charge in the intermediate band, and illustrates a primary shortcoming of 0-D models and quasi-1-D models where linear potential profiles are assumed. The calculated quasi-Fermi level E_{FI} is significantly below E_I, with a corresponding low occupation of the IB. The assumption of a half-filled IB [20, 59, 61] will therefore not hold unless there is another mechanism for electron capture/escape such as field emission [58, 68]. Consequently, the high-efficiency predicted by the 0-D models would not be realized in this device configuration.

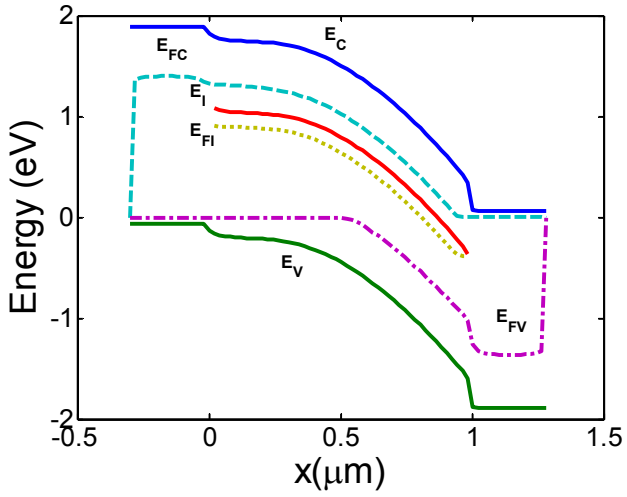

Figure 5.4 Calculated energy band diagram for a lightly doped base (W = 1 μm, N_D=10^{14}cm^{-3}).

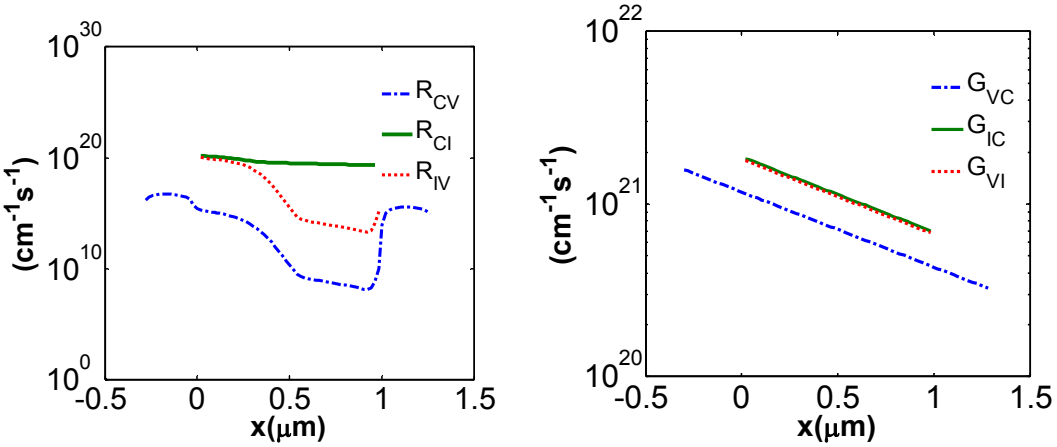

Figure 5.5 Recombination (left) and generation (right) rate

The *J-V* curve shows degraded filled factor deviating from ideal box-shaped characteristics, resulting from strong space charge effect in the intermediate band. The current-voltage (*J-V*) characteristics of this device under varying SRH lifetime are shown in Figure 5.6. The finite slope near the short circuit condition is due to an increase in recombination rate with bias and reduced carrier collection due to the reduction in electric field with increasing forward bias. The fill factor and resulting conversion efficiency (η) decrease with decreasing τ_{SRH}, as shown in the inset of Figure 5.6. The

decreased V_{oc} is the result of increased diode dark current due to non-radiative recombination. Thusfar, experimental results have shown a decrease in V_{oc} for the case of IBSC, while results for J_{sc} have been variable[21, 23, 24, 65, 80, 82]. The results of Figure 5.6 suggest that the reduction in V_{oc} may be associated with increased SRH process associated with the material with impurity sites. In the extreme case of high SRH recombination, J_{sc} for IBSC may be reduced below the value of a control sample without IB.

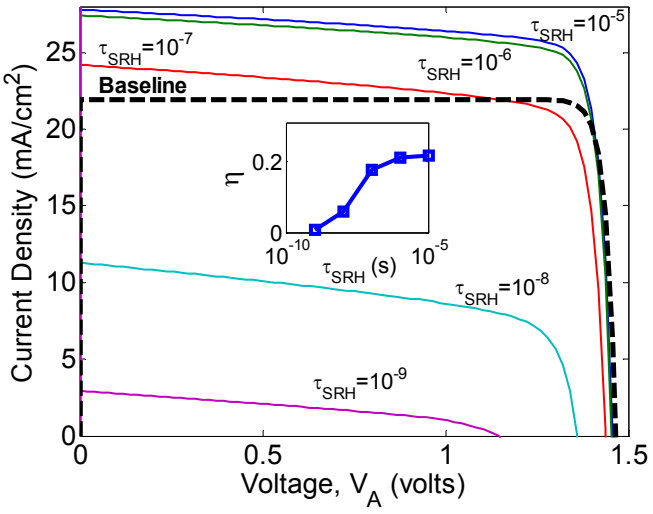

(a)

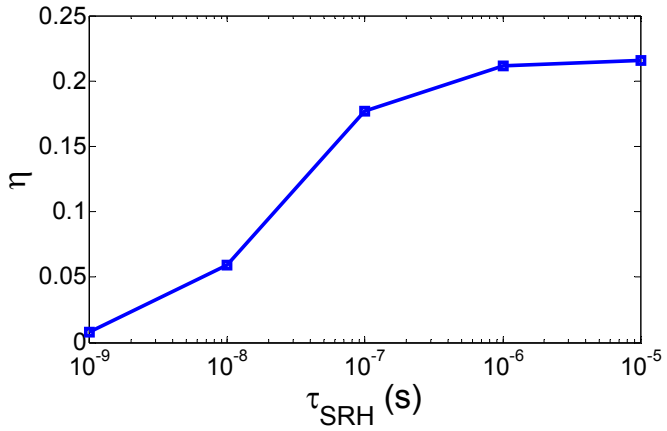

(b)

Figure 5.6 (a) Current-voltage characteristics for varying τ_{SRH} and (b) resulting conversion efficiency (W = 5μm, N_D (base)=10^{14}cm^{-3}). The baseline is *p-i-n* type device without intermediate levels (IL) and SRH.

Solar cell conversion efficiency will depend on base width (W), where there is a clear tradeoff related to maximizing optical absorption (large base width W) and maximizing carrier collection (small base width W). This tradeoff is typically deemed to be limited by SRH recombination. In these simulations, however, an optimal W is also found for the case of no SRH recombination. The J-V characteristics and conversion efficiency dependence on W for the case of no SRH are shown in Figure 5.7. The decrease in efficiency for large W is the result of increased recombination rates via the intermediate levels in the base region. The recombination processes via the IL will depend on carrier populations in the IL, where increasing W will increase filling of impurity states and increase recombination rate. This result emphasizes the importance of the 1-D drift diffusion model, where filling of impurity states and recombination rates have a significant dependence on space charge characteristics of the device.

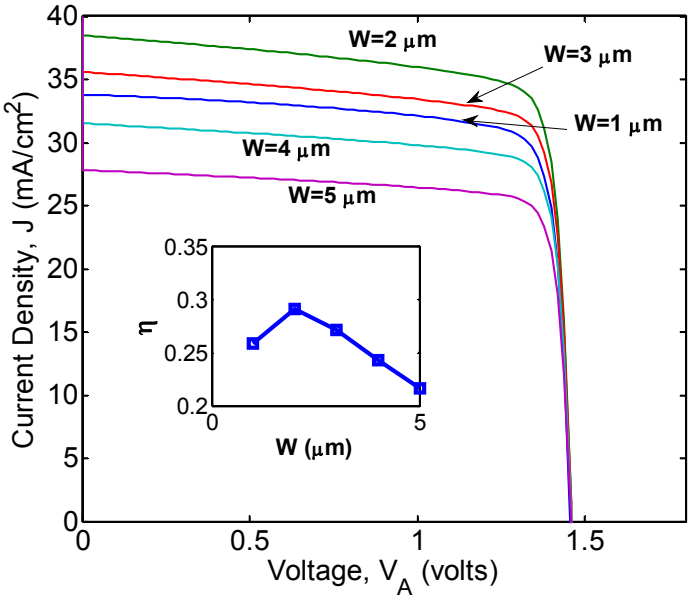

(a)

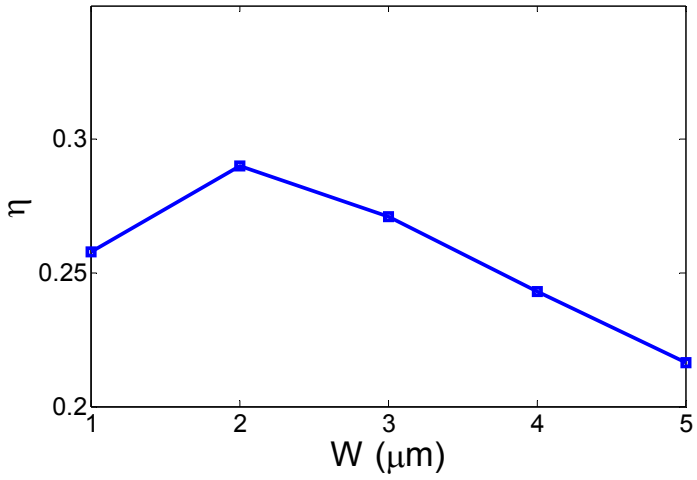

(b)

Figure 5.7 (a) Current-Voltage characteristics for varying base width (no SRH recombination) and (b) resulting conversion efficiency (N_D (base) = 10^{14}cm^{-3}).

5.3.4 Compensated Base Doping

From section 5.3.3, it is clear that it is desirable to improve the state filling at intermediate band. Nonetheless, half-filled intermediate band also comes with strong space charge effects. For acceptor-like states or equivalently, for the materials with

chemical potential below intermediate band at 0 K, the half-filled states carry negative charges. On the other hand, for donor-like states or equivalently, for the materials with chemical potential above intermediate band, the half-emptied states carry positive charges. Consequently, In order to achieve the half-filled condition, the remedy has to be proposed to compensate the strong effect of space charge in the intermediate band. Here the use of base doping is proposed as a way to compensate the space charge effect brought about by the carriers in the intermediate states.

The following figure shows the occupation of IB for different base doping. The doping is n-type from $1x10^{17}$ cm^{-3} to $9x10^{17}$ cm^{-3} and the concentration of impurity incorporation (N_I) is $1x10^{18}$ cm^{-3}. it is clear that when the base doping is half of N_I, the state filling of IB is clamped at 50%.

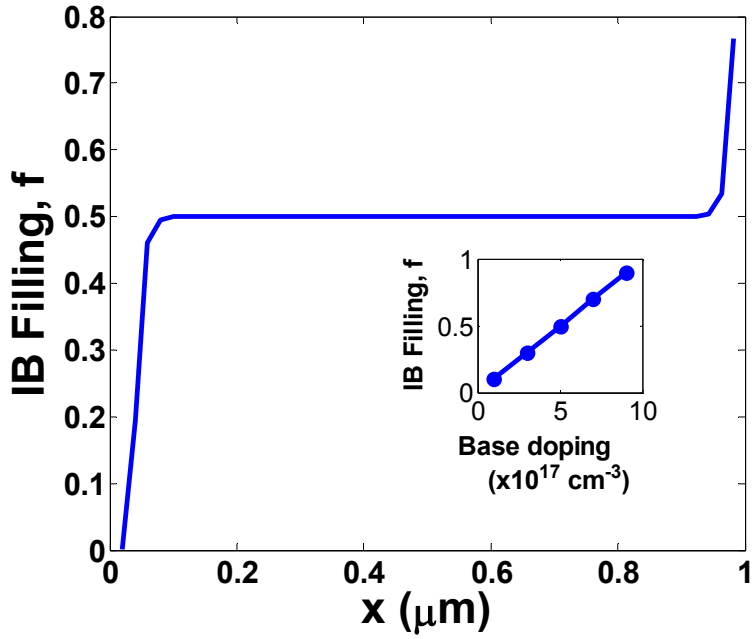

Figure 5.8 Spatial depenedence of IB fill factor f for the case of $N_D=5\times10^{17}cm^{-3}$ and (inset) dependence on base doping.

The resulting band diagram looks very similar to Luque's "hand-drawn" band diagram, and the idea of compensated base doping may have already been intended though there have not been any direct results shown since no drift-diffusion model has been available for IBSC. From the equilibrium band diagram, there is a flat band region,

and the intermediate band Fermi level (E_{FI}) is pinned at E_I. This results in half-filled condition for a majority of the base region. At the base/emitter interface, the occupation of the intermediate band is emptied or completely filled in order to support the field necessary for the formation of the depletion region. The carrier transport at the flat band region is dominated by diffusion where diffusion length has to be much longer than the base width to maintain satisfactory charge collection. Nonetheless, the fact that a depletion region exists at both sides of the base region somewhat alleviates this problem. This also reflects the importance of the drift-diffusion model since the carrier transport and recombination on the complex band profile can only be accurately described by a 1-D numerical model.

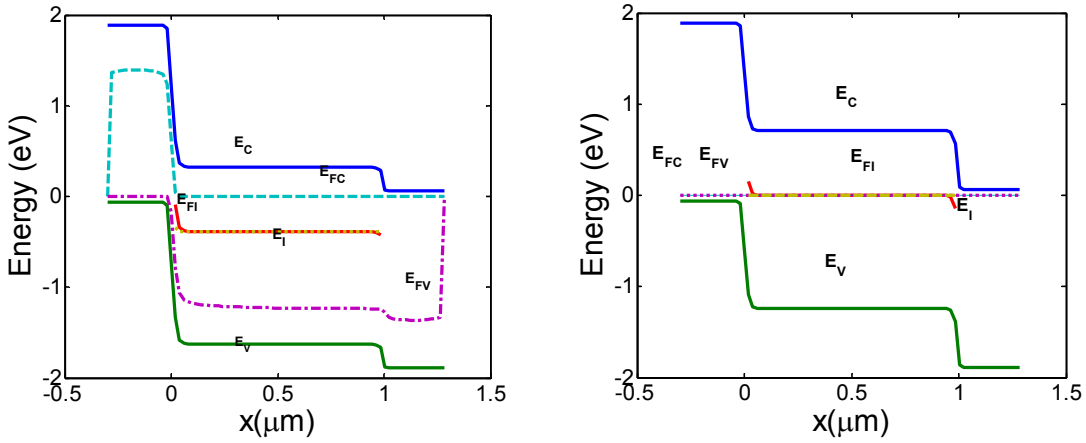

Figure 5.9 Calculated energy band diagram for the case of compensated base doping with W = 1 μm, N_I=1x10^{18} cm^{-3} and N_D=5x10^{17} cm^{-3}.

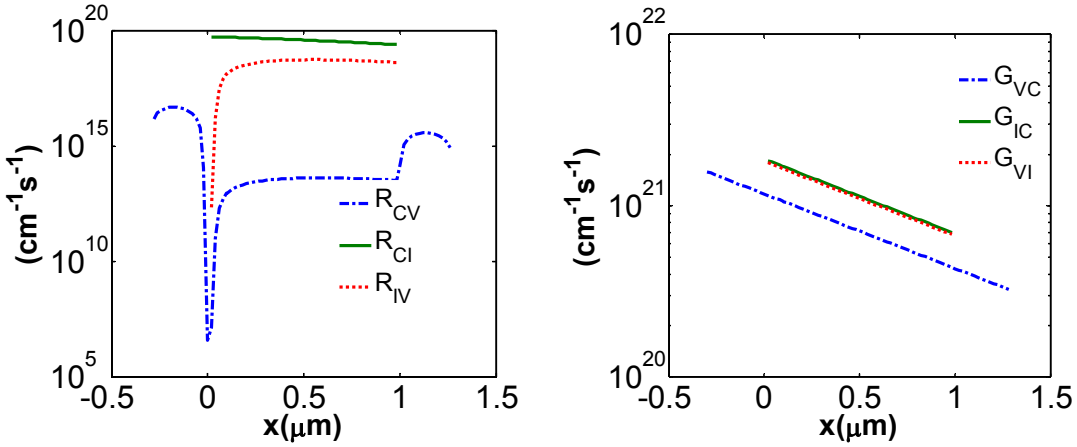

Figure 5.10 Recombination (left) and generation (right) rate

From Figure 5.11, it is clear that the compensated base doping clamps the IB occupation at 0.5 even at biased condition (for all of the biasing condition of interest. i.e. from J_{sc} to V_{oc}). This is important for the operation of solar cell device since the photocurrent has to be sustained at roughly the same value even at elevated bias in order to achieve high efficiency. This issue is specific to intermediate band photovoltaic device since for conventional baseline cell the optical generation does not depend on the state-filling for there are abundant empty states and filled states in the CB and VB, respectively.

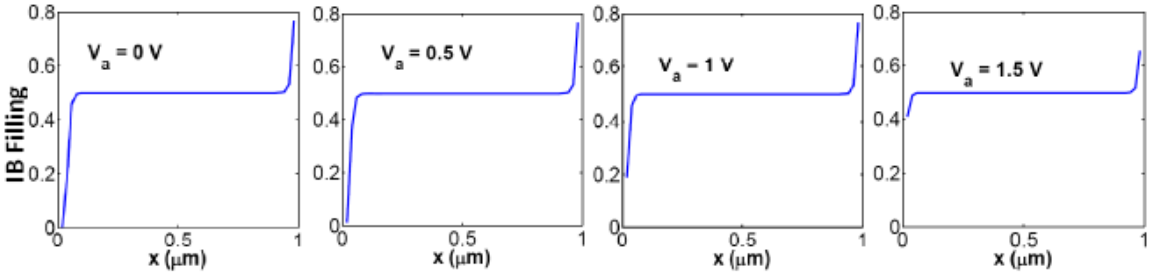

Figure 5.11 IB occupation v.s. bias

The Luque's assumption in the original 0-dimensional IBSC model (PRL 1997) can be achieved by compensated base doping, which includes: (1) Half-filled IB (2) E_{FI} is pinned at E_I (E_{FI} has its equilibrium position) (3) E_{FI}, E_{FC}, E_{FV} are flat in absorber base region. The fact that E_{FI} is pinned at E_I is the prerequisite for Eq. 5.13.a and Eq. 5.13.b to be true. The fact that E_{FI}, E_{FC}, E_{FV} are flat in absorber base region validates 0-D modeling since the spatial dependence of the physical quantities can be ignored. This is also the assumption made in Ref. [20]. This result implies that the predicted high efficiency using 0-D analytical or semi-analytical model may only be achievable in some idealized cases, such as compensated base doping or efficient thermionic field. The 1-D numerical drift-diffusion model is important since it reveals the true scenario for a specific situation, material system, or device structure.

In Figure 5.12, Luque and Luque baseline are *J-V* calculated using detailed balance model while DD base doping, DD no base doping and DD baseline are *J-V* calculated using drift-diffusion model presented in this chapter. The baseline cell is devices with no intermediate band present. It is clear that the IBSC with compensated base doping can achieve nearly the same efficiency predicted by ideal IBSC theory (efficiency limit of 0-D model). In addition, the compensated base doping fixes the decreased FF caused by the

charge in the intermediate band, which is clear by comparing to the case of intrinsic or lightly doped base. The V_{oc} of IBSC and baseline cell are nearly identical, indicating the increased photocurrent might not be accompanied by decreased V_{oc}. This strengthens the confidence for intermediate-band photovoltaics since while most experimental work shows decreased V_{oc}, the theoretical study here shows that V_{oc} can actually be maintained by using a highly doped emitter without intermediate band. As a result, from the point of view electrostatics, carrier transport, generation and recombination, the increased J_{sc} does not have to be accompanied by degraded V_{oc} in principle. The observed degradation may result from other sources such as excessive defect states introduced by imperfect process technology during impurity or quantum dot incorporation.

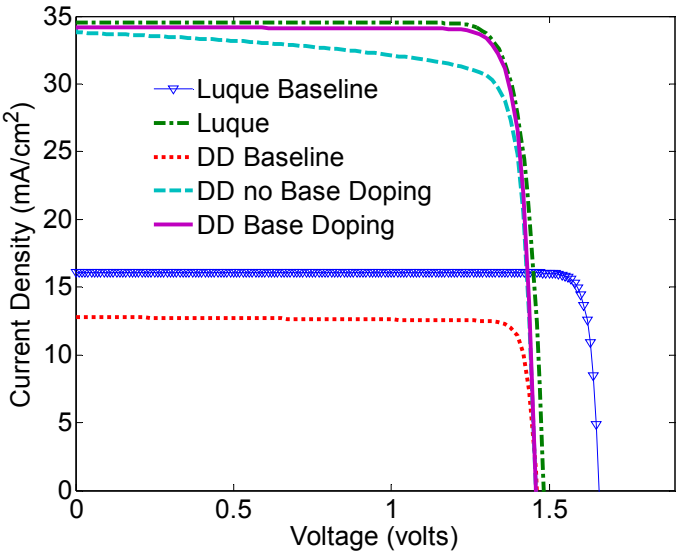

(a)

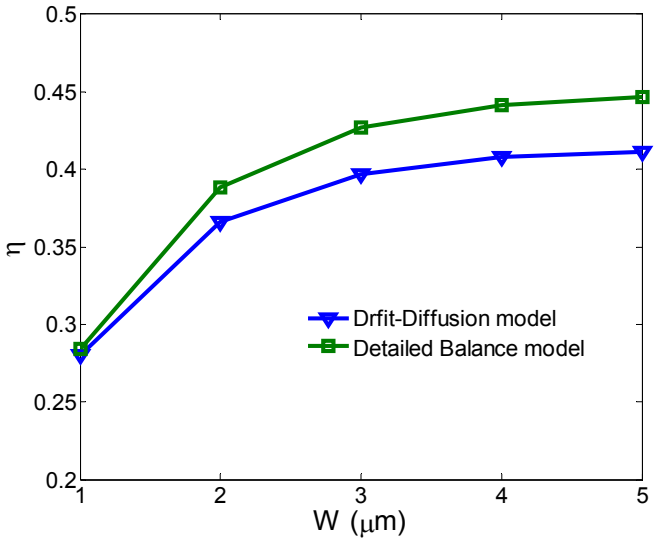

(b)

Figure 5.12 (a) *J-V* curves and (b) efficiency comparing detailed balance 0-D model and drift-diffusion 1-D model. E_G=1.95 eV, E_I=1.24 eV, N_D (base) =5×10^{17}cm^{-3} for drift-diffusion model.

The higher V_{oc} of the baseline cell calculated with Luque's 0-D model [20] is primarily due to the neglect of minority carrier injection current, which is significant since the p- and n- emitter should be kept thin. The Drift-diffusion model provides a more

realistic picture of device operation. The same V_{oc} for IBSC calculated with DD and Luque's 0-D model indicates that when IB exists, the recombination current via IB is the primarily component for diode dark current. The fact that $J_{r,IB} > J_{diff} >> J_{r,BB}$ near the open circuit condition can be verified. The estimation is based on the following equations:

$$J_{r,CI} = q\int_0^W R_{CI}\,dx$$
$$J_{r,IV} = q\int_0^W R_{IV}\,dx,\ J_{r,CV} = q\int_0^W R_{CV}\,dx \qquad 5.16$$

$$J_{diff} = \left(\frac{qD_n n_i^2}{W_p N_A} + \frac{qD_p n_i^2}{W_n N_D}\right)\times\left(\exp(\frac{qV_A}{kT}) - 1\right) \qquad 5.17$$

At $V_A = V_{oc} = 1.457$ V, $J_{r,CI} = 19.49$ mA/cm^2, $J_{r,IV} = 18.94$ mA/cm^2, $J_{r,CV} = 0.0044$ mA/cm^2, $J_{diff} = 13.9$ mA/cm^2.

The *J-V* characteristics and conversion efficiency for varying SRH lifetime and base width are repeated for the case of compensated base doping

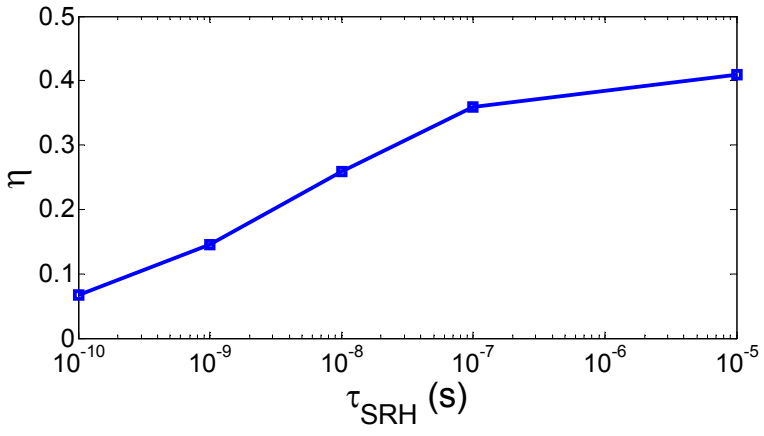

(

(b)

Figure 5.13 and Figure 5.14). An increase in conversion efficiency is calculated for the compensated base doping design in comparison to lightly-doped absorber layers. The occupation of intermediate states is increased from nearly empty to *f*~0.5 through compensated base doping. The resulting fill factor is improved from 0.811 to 0.871 (W=1 μm), and the maximum efficiency for large W is increased from 29.0% to 41.1%. Compensated base doping clamps the quasi-Fermi level E_{FI} at the E_I regardless of bias condition, preventing the depletion of the IL that would occur for the lightly-doped base

design. Similar to prior IBSC model formulations [59-62, 68], the effect of IL occupation on the optical absorption coefficient is not incorporated in this model. The incorporation of IL occupation is expected to provide even lower efficiency values for the case of a lightly doped base, where low occupation in the impurity states would provide small values for absorption between the IL and CB (α_{IC}). The dependence of calculated efficiency on base width for the case of no SRH recombination in the compensated base doping design is shown in Figure 5.14. The compensated base doping design eliminates any constraint on maximum W, in contrast to Figure 5.7. The doping in this design serves to fix the occupation of IL near f=0.5, providing a fixed recombination rate that would otherwise vary with IL occupation due to space charge characteristics. The efficiency in Figure 5.14 is η = 28.05% (W = 1 μm) and 41.12% (W = 5 μm), very close to the detailed balance limit of η =28.36% (W = 1 μm) and 44.57% (W = 5 μm) [20]. This indicates transport between impurity states is not essential for high efficiency subbandgap absorbing solar cells once half-filled band and suppressed non-radiative recombination is achieved. One of the outcomes of the simulations for the compensated base doping scheme is an increase in the solar cell fill factor, where a more "box-like" J-V curve is observed in relation to the lightly doped device structure. This result is consistent with recent experimental results, where a δ-doping scheme matched to the density of quantum dots has resulted in a "box-like" J-V curves [23, 65, 82],. On the contrary, IBSC consisting of quantum dots embedded in a *p-i-n* device structure have demonstrated reduced fill factors in comparison to baseline control samples [21, 80], similar to the case of an subbandgap absorbing solar cell with lightly doped base and increased SRH recombination presented in this work.

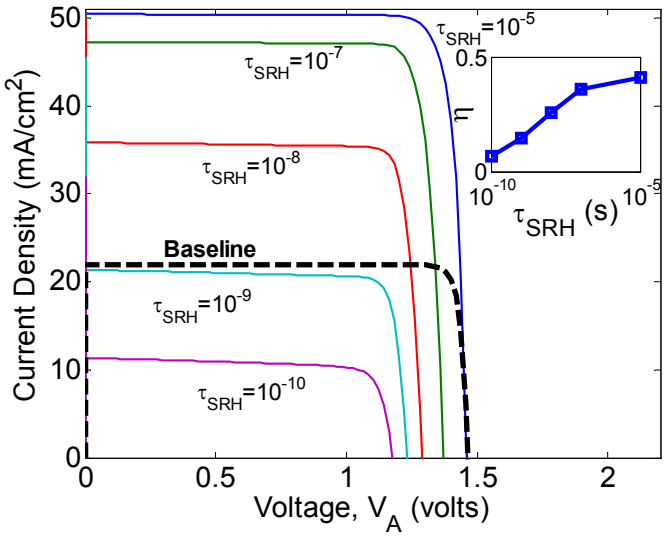

(a)

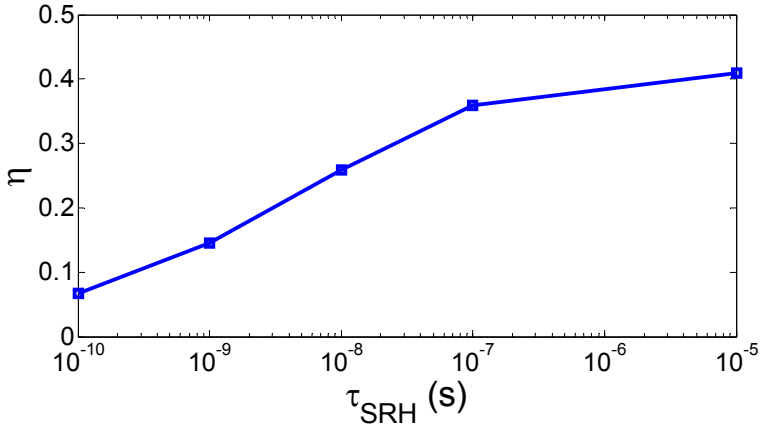

(b)

Figure 5.13 (a) Current-voltage characteristics for varying τ_{SRH} and (b) resulting conversion efficiency (W = 5 μm, N_D (base) =5×10^{17}cm^{-3}). The baseline is *p-i-n* type device without intermediate levels (IL) and SRH

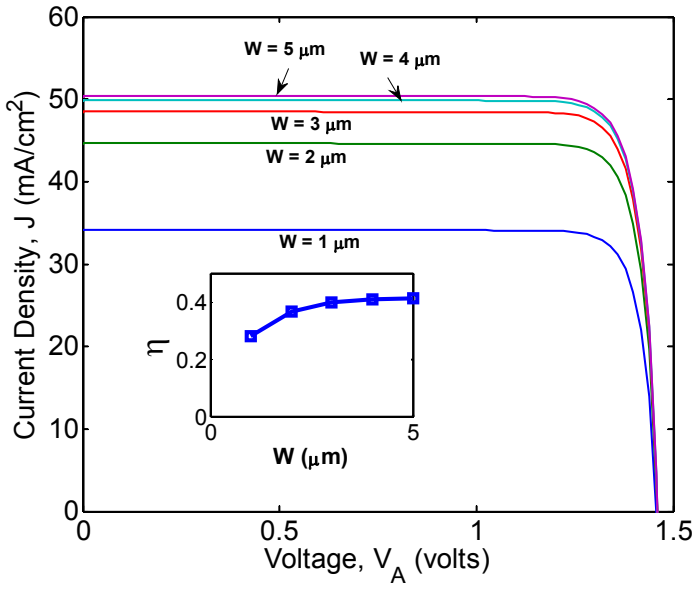

(a)

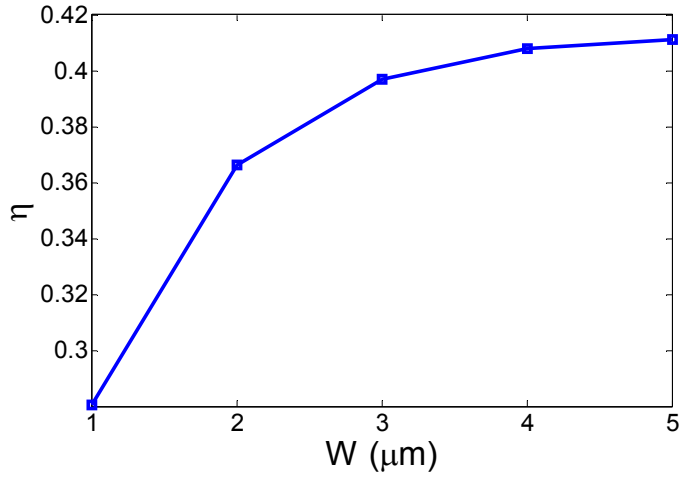

(b)

Figure 5.14 (a) Current-Voltage characteristics for varying base width (no SRH recombination) and (b) resulting conversion efficiency (N_D (base) =5×10^{17}cm^{-3})

5.4 Conclusion

A one-dimensional IBSC drift-diffusion model is presented. The results are consistent with prior 0-D models verifying the ability to achieve high efficiency in the case of low non-radiative recombination and good electronic transport properties. The drift-diffusion

model has identified that space-charge effects are significant for IBSC with lightly-doped regions, where devices would have low occupation of IB states and corresponding low conversion efficiencies. A doping compensation scheme is proposed to clamp the IB quasi-Fermi level at the IB position to reduce space-charge effects and to maximize optical generation. The compensated base doping scheme also eliminates the intrinsic dependence of efficiency on base doping due to space-charge effects and increases the maximum achievable efficiency to >40%, near the values predicted for 0-D IBSC devices. The 1-D drift diffusion model facilitates the future design of IBSC and related devices using the established framework of solving carrier continuity and electrostatic equations.

Chapter VI Analysis of Experimental Work on Intermediate Band Solar Cells

6.1 Introduction

Chapters 3-5 focus on theoretical aspects of intermediate band devices where predictions are made on the efficiency achievable by subbandgap photovoltaic devices. Experimental effort has been made in our group with ZnTe:O although the efficiency achieved is still far below the predicted high efficiency. The goal of this chapter is to provide competent analysis of experimental data and help to understand the physical reasons for the observed low efficiency. The material growth and device fabrication is done by Dr. Weiming Wang in author's group and the time resolved photoluminescence is measured by Dr. Wyatt Metzger at the National Renewable Energy Lab. Some of the material parameters are not currently available, where further experimental work is required. For example, the optical absorption coefficient for subbangap states should depend on state occupation though it is difficult to measure absorption coefficient with uniform state occupation given the complex spatial dependence on illumination. The emphasis of this chapter is to apply IBSC models presented on this thesis to recent experimental work on ZnTe:O devices.

6.2 ZnTe:O Material System

Wide bandgap semiconductors based on ZnO, ZnTe, and related II-VI compound semiconductors are attractive for several device applications including light emitters and detectors operating in the visible/ultraviolet spectral region, and transparent electronics. Research and development efforts on alloys related to ZnO have predominantly focused

on the mixed cation materials CdZnO, MgZnO, and BeZnO. Mixed anion alloys related to ZnO such as ZnO(S,Se,Te) may also provide the ability to tune semiconductor bandgap energy in the visible and ultraviolet spectral region, but are less understood. ZnTe has a direct bandgap at 2.29eV, corresponding to the green optical wavelength, and has been investigated in great detail for application to ZnSe-based visible light emitters, CdZnTe x-ray detectors, and ZnTe buffer layers for HgCdTe infrared detectors. ZnTe has shown the ability for controllable p-type doping by nitrogen [88-91], with hole concentrations of up to 10^{20} cm^{-3}. The source of the unique p-type nature for this wide-bandgap material is believed to be the native defect structure, where defects lie within the valence band rather than within the bandgap [92]. The unique p-type behavior of ZnTe, a notorious problem for ZnO and many wide-bandgap semiconductors, and possibility for tunable bandgap energy in the visible spectral region make alloys of ZnTeO a potentially attractive material for optoelectronic devices.

Comparing to oxygen doping in CdTe, where oxygen acts as a shallow acceptor [93], doping or alloying of ZnTe with oxygen is believed to result in a "highly mismatched alloy" where Te and O atoms possess a very different electronegativity. In the extreme of low oxygen concentration, a substitutional impurity of O_{Te} in ZnTe results in a defect level 0.4eV from the conduction band and a strong radiative transition at 1.9eV [94, 95]. This strong radiative transition in ZnTe:O has in fact been used as red light emission diode [96], and also a phosphorescent material for x-ray detectors, where long radiative lifetimes of > 1 μs have been reported [97]. Higher oxygen content in ZnTe is predicted to introduce a narrow electronic band in the material, as explained by a band anticrossing model [33]. Experiments and calculations have suggested the presence of such an intermediate band in ZnTeO and the quaternary ZnMnTeO [33]. Bandgap reduction in ZnTe with the introduction of oxygen has also been reported by other research groups recently [98, 99], providing further evidence of an intermediate band in this alloy. In this work, the synthesis of ZnTeO thin films by pulsed laser deposition and molecular beam epitaxy is investigated to further examine the possible formation of an intermediate band or alloy system spanning the visible/UV spectral region.

6.3 ZnTe:O Growth and Photoluminescence Spectrum

ZnTe:O samples were grown by molecular beam epitaxy using solid source effusion cells for Zn and Te, and an RF plasma source for oxygen and nitrogen incorporation. Samples were grown on n^+-GaAs (100) substrates for material characterization and solar cell device structures. Nitrogen was used to achieve p-type ZnTe for the diode structure. An oxygen flow rate of 1 sccm was used, where a concentration of $1x10^{19}$ cm^{-3} is estimated based on the assumption of a similar incorporation rate for oxygen and nitrogen. Solar cell devices were fabricated using photolithography, metallization and liftoff, and wet chemical etching. Current-voltage characteristics were measured using a Keithley 4200 semiconductor parametric test system. Solar cell optical measurements were taken using a grating spectrometer for spectral response and a solar simulator for efficiency measurements.

A room-temperature photoluminescence spectrum for ZnTe:O grown on GaAs is shown in Figure 6.1, indicated both a bandedge response for ZnTe at 2.3 eV and a strong sub-bandgap response related to oxygen doping in the range of 1.6-2.0 eV. In a majority of the ZnTe:O samples, the spectrum is dominated by defect emission, where the spectrum in Figure 6.1 was chosen in order to illustrate both defect and ZnTe bandedge emission. In comparison, the photoluminescence spectrum for an undoped ZnTe sample shows a sharper bandedge transition, and a much weaker defect emission. The presence of defect emission in the undoped ZnTe sample is believed to be due to residual oxygen present in the growth chamber. The strong radiative emission due to oxygen in ZnTe is consistent with previous detailed studies [94-96]. The strong emission for the oxygen defect in ZnTe denotes a highly radiative transition, and is therefore a highly desirable characteristic for the IB solar cell. Complementary optical absorption spectra inferred from transmission measurements have been reported previously for samples deposited on sapphire under varying oxygen partial pressure [100]. A sharp bandedge response is observed for ZnTe without oxygen, while increasing sub-bandgap optical absorption is observed with increasing oxygen. The sub-bandgap optical absorption is consistent with the photoluminescence characteristics, and is similarly attributed to oxygen defects in ZnTe.

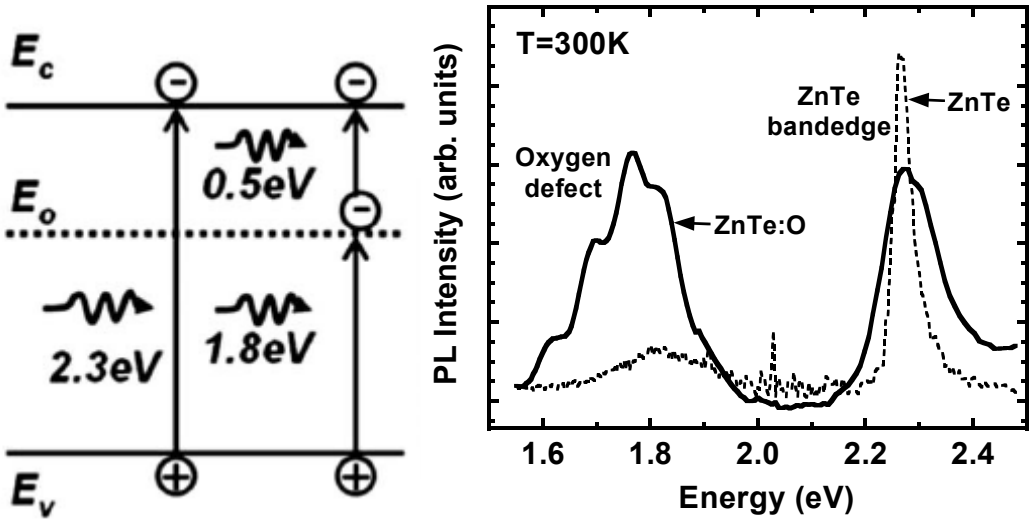

Figure 6.1 (Left) energy band diagram for ZnTe:O with associated optical transitions for intermediate band solar cells and (right) room-temperature photoluminescence spectra of ZnTe:O illustrating emission from both the ZnTe bandedge and oxygen related defect states Acknowledgement: Dr Weiming Wang, the University of Michigan, Ann Arbor.

6.4 ZnTeO Alloy and Absorption Spectrum

In this section, the analytical expressions for absorption cross sections are applied to calculate absorption coefficient for various transitions mechanisms includes band to band transitions and transitions via intermediate band. The results are then compared to experiment.

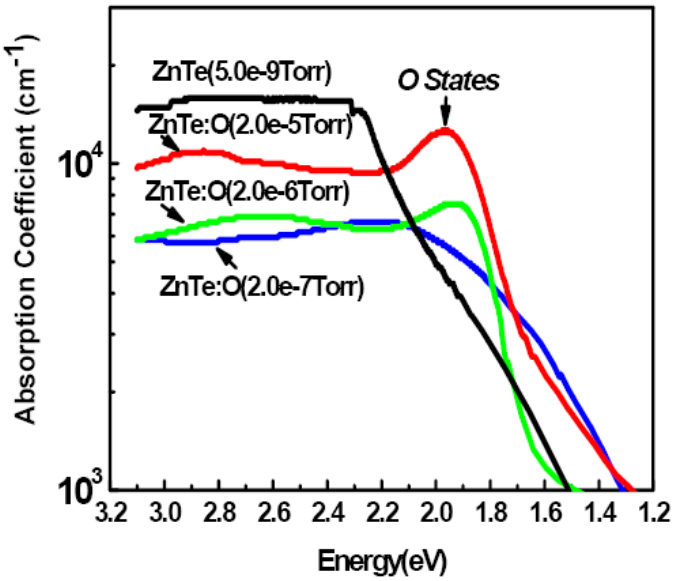

Figure 6.2 Absorption coefficient of ZnTe:O grown by molecular beam epitaxy with different oxygen partial pressure

Band to band optical transitions can be derived from first order time dependent perturbation theory and have the form

$$\begin{aligned}\alpha_{\mathrm{VC}}(h\nu) &= \frac{\pi e^2 \hbar}{m_0^2 c n_{\mathrm{r}} \varepsilon_0} \frac{1}{h\nu} \left|(\vec{a}\cdot\vec{p})_{if}\right|^2 D_{\mathrm{CV}}(h\nu) \\ &= A\frac{(h\nu - E_G)^{1/2}}{h\nu}\end{aligned} \qquad 6.1$$

where D_{CV} is the joint density of states, and $(a\cdot p)_{\mathrm{if}}$ is the momentum matrix element for the transition. Under parabolic band approximation, the absorption spectrum has a square root dependence on energy. The matrix element may be determined from initio band structure calculation. Several groups have performed calculations and experimental measurements for ZnTe absorption coefficicents [101-104] though the value of matrix element is not revealed in literature. In addition, the matrix element for ZnTeO is generally unavailable, and the absorption spectrum for ZnTeO deviates from ZnTe due to oxygen incorporation, and thus using ZnTe matrix element is not accurate due to the fact that incorporation of high concentration oxygen atoms can alter the band structure and thus the absorption of VB-CB transitions [100]. Here we choose to extract the matrix

element from experiment optical transmission measurement by plotting $\alpha \times h\nu$ v.s. $h\nu$-E_G [105, 106], where the value will be utilized later to calculate subbandgap transitions.

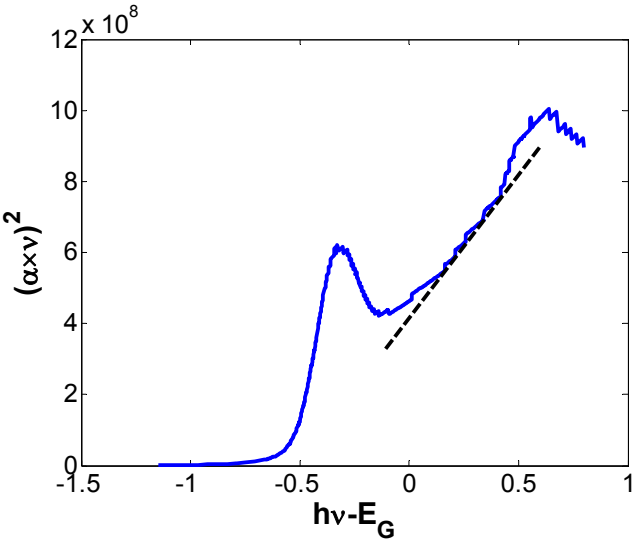

Figure 6.3 Illustration of squart-root dependence of absorption coefficient on energy for ZnTe:O

For valence band to intermediate state transitions, the model proposed by Sundstrom et al. [107-113] is employed here to calculate the optical absorption cross section σ_{opt}:

$$\sigma_{opt}(h\nu) = f\left|G(k)\right|^2 \frac{e^2 \pi M (2m_v)^{3/2}}{m_0 c \varepsilon_0 n_r h^2} (h\nu - E_G + E_I)^{1/2} \qquad 6.2.a.$$

$$f = 2\left|p_{cv}\right|^2 / mh\nu \qquad 6.2.b.$$

$$G(k) = 2(2\pi\alpha)^{1/2} / (\alpha^2 + k^2) \qquad 6.2.c.$$

$$\alpha^2 = 2m_c E_I / \hbar^2 \qquad 6.2.d.$$

where ε_0 is permittivity in vacuum, c is the speed of light, e is elementary charge, h is Plank's constant, m_0 is free electron mass, M is the number of conduction band minima (valence band maxima). The dipole moment p_{CV} can be extracted from α_{VC} by plotting $\alpha \times h\nu$ v.s. $h\nu$-E_G. The matrix element p_{CV} for valence band to conduction band transition is related to the matrix element p_{VI} for valence band to intermediate state transition [107, 108]:

$$p_{VI}(k) = V^{-1/2} G(k) p_{VC}(k) \qquad 6.3$$

where V is the volume of the crystal. In the derivation for σ_{opt}, the parabolic band approximation is employed for the density of states function [102]. Lucovsky wavefunction [109] is assumed at intermediate states (final states) and the wavefunction at initial states is the superposition of plane waves.

The absorption coefficient for intermediate to conduction band transition, α_{IC}, is not available from experimental measurement due to low state filling for oxygen state under equilibrium. This results from the fact that undoped ZnTeO is intrinsically p type due to native acceptors and the Fermi level at equilibrium is closer to the valence band [92]. Therefore, a theoretical model is used here to model the transition from intermediate states to the conduction band. A hydrogenic model has been utilized to calculate the energy levels for dopants in semiconductors though in the case of deep electronic states, the hydrogen atom model is inaccurate since the ion core potential instead of the columbic potential is responsible for the ground state binding energy. The Lucovsky model is in general more suitable to model states deep in the bandgap [109]. A simple delta function is assumed to represent the core potential and Fermi-Golden rule is then applied to calculate transition rates from the intermediate state to conduction band.

$$\sigma_{\text{opt}}(h\nu) = \frac{1}{n_{\text{r}}}\left(\frac{F_{\text{eff}}}{F_0}\right)^2 \frac{16\pi e^2 \hbar}{3m^* c} \frac{(E_{\text{I}})^{\frac{1}{2}} (h\nu - E_{\text{I}})^{\frac{3}{2}}}{(h\nu)^3} \qquad 6.4$$

where c is the speed of light, e is elementary charge, h is Plank's constant, m^* is the free electron mass, F_{eff} is the effective field at impurity site and F_0 is average field in crystal. Effective field ratio F_{eff}/ F_0 may be evaluated by [114]

$$\frac{F_{\text{eff}}}{F_0} = 1 + \frac{n_r^2 - 1}{3} \qquad 6.5$$

and is typically in the range of 1~5.

The absorption coefficient is proportional to optical absorption cross section and state filling, and is calculated by integration over the energy distribution of intermediate states. Gaussian density of state is assumed for oxygen state though other DOS function can also be applied in the same way

$$\alpha_{\mathrm{VI}}(h\nu) = \int \sigma_{\mathrm{opt,\,VI}}(h\nu) D(h\nu)(1-\zeta) d(h\nu) \qquad 6.6.a.$$

$$\alpha_{\mathrm{IC}}(h\nu) = \int \sigma_{\mathrm{opt,\,IC}}(h\nu) D(h\nu)\zeta d(h\nu) \qquad 6.6.b.$$

$$D(h\nu) = \frac{N_{\mathrm{I}}}{\sqrt{2\pi}\sigma_{\mathrm{IB}}} \exp\left(-\frac{1}{2}\frac{(h\nu - E_{\mathrm{I}})^2}{{\sigma_{\mathrm{IB}}}^2}\right) \qquad 6.6.c.$$

where ζ Characterizes state filling, $D(h\nu)$ is the density of states function for intermediate states, and σ_{opt} is optical absorption cross section

The straight line segment for the lower energy portion in $\log(\alpha)$ vs E plot is the bandtail absorption due to the poly-crystalline nature of the ZnTeO film, and can be modeled by Urbach absorption [115]

$$\alpha_{\mathrm{bandtail}}(h\nu) = \alpha_0 \exp(-\beta(h\nu - E_0)/kT) \qquad 6.7$$

where α_0, β, E_0 are fitting parameters. The clear cutoff between bandtail absorption and band to band or intermediate band absorption may be difficult to determine and thus is a fitting parameters, and here E_0 is chosen to be 1.81 eV since in measured spectrum it is clearly a straight line below valence to intermediate band absorption.

Table 6-1 Simulation parameters for ZnTeO absorption spectrum

Band gap Energy E_{G}	2.3 eV
IB Energy position E_{I}	1.85 eV
m_{C}	$0.13m_0$
m_{V}	$0.6m_0$
IB density of states N_{I}	$1.0\mathrm{x}10^{19}$ cm^{-3}
IB bandwidth σ_{IB}	0.05 eV
Refractive index n_r	2.7

The bandgap energy E_{G} and E_{I} can be found in reference [33, 79, 100, 116, 117], m_{C}, m_{V} in reference [118], and refractive index in reference[119] For oxygen-doped ZnTe films grown by MBE, oxygen concentration is too low to be detected by X-ray photoelectron spectroscopy measurement. Assuming similar incorporation rates for

nitrogen and oxygen, the oxygen concentration in ZnTe grown with 2×10^{-5} Torr oxygen partial pressure is estimated to be near 10^{19} cm^{-3}. σ_{IB} may be found in reference [33].

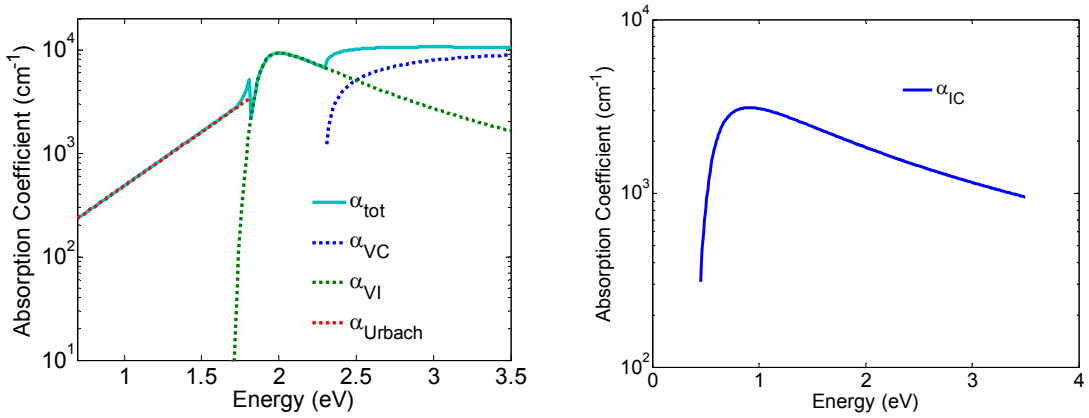

Figure 6.4 Calculated optical absorption coefficient of ZnTeO samples grown by MBE with oxygen plasma

Figure 6.4 shows the calculated absorption spectrums for ZnTe:O. By utilizing analytical expression as described in this section, the absorption coefficient for different absorption mechanism including VB-CB, VB-IB, and IB-CB transtions can now be at least estimated. In Figure 6.4, α_{IC} is shown in a separate plot since ZnTe:O is intrinsically p-type and thus IB-CB transitions might not be observed in measured date. From Figure 6.4 we see that significant spectral overlap presents between absorption spectrums of different transitions. This is not surprising since the density of state of conduction and valence band tends to increase beyond bandedge, and thus there is no appropriate mechanism to cutoff low threshold absorption process for high energy photons. Nonetheless, this can significantly lower the efficiency for intermediate band photovoltaics [60]. In later section, the effect of spectral overlap is going to be incorporated into ZnTe:O diode current-voltage characteristic calculation and the result will be compared to experiment. In Figure 6.5, the theoretical absorption curve for α_{tot} is plotted with measured spectrum. Theoretical and experimental curves basically match each other and a strong absorption peak due to oxygen states is observed.

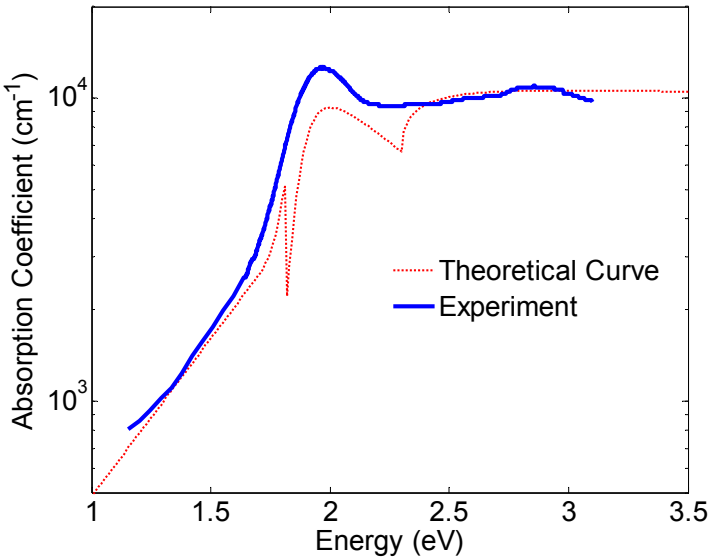

Figure 6.5 Theoretical and experimental absorption coefficient for ZnTeO.

Acknowledgement: Dr. Weiming Wang, the University of Michigan, Ann Arbor.

6.5 Time Resolved Photoluminescence

In this section time resolved photoluminescence (TRPL) for ZnTe:O is measured. The goal is to experimentally measure/approximate carrier recombination lifetimes for band to band and intermediate band transitions. Time-resolved photoluminescence data for the three samples with representative scans at 550 nm and 700 nm shown in Figure 6.6. The emission peaks at 550 nm demonstrate fast decay times for both ZnTe:N and ZnTe:NO, with time constants on the order of 100 ps. The time resolution of the TRPL setup is on the order of tens of picoseconds, similar to the time constants for conduction to valence band transitions, suggesting that the carrier lifetime for electrons in the conduction band is <100 ps. The emission at 700 nm follows a biexponential function with two time constants, where the PL intensity follows the relation $A_o+A_1exp(-t/\tau_1)+A_2exp(-t/\tau_2)$, as shown in Figure 6.6(b). The fast and slow time constants of the 700nm emission may be attributed to surface and bulk recombination processes, respectivetly. For the ZnTe:O sample, long decay times exceeding 1μs are observed at low injection levels. In contrast to the ZnTe:N and ZnTe:NO samples, the decay time constant for bulk recombination in

the ZnTe:O sample exhibits a dependence on injection level, as illustrated in Figure 6.7(a).

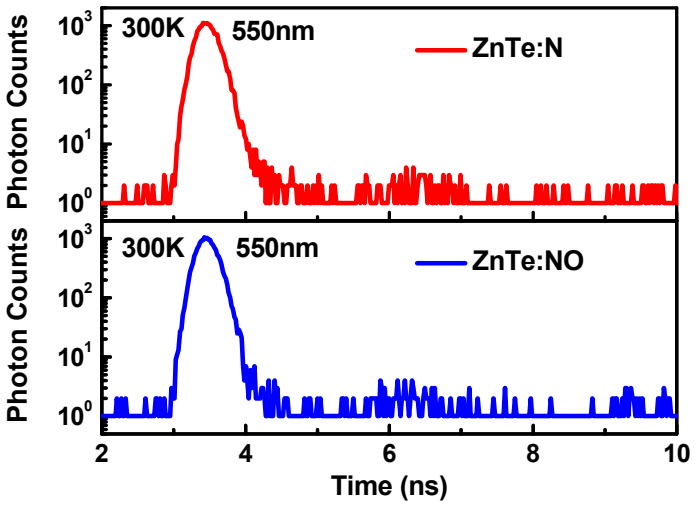

(a)

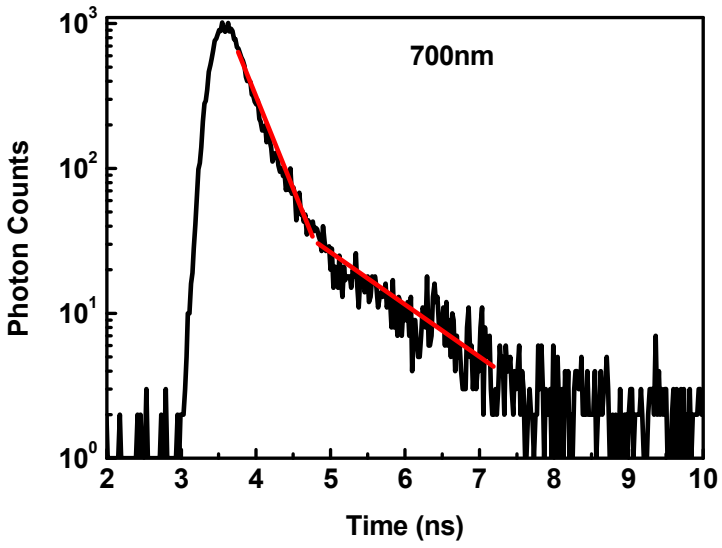

(b)

Figure 6.6 Time-resolved photoluminescence of (a) ZnTe:N and ZnTe:NO at 550nm and (b) ZnTe:NO at 700nm. Acknowledgement: Dr. Wyatt Metzger, National Renewable Energy Laboratory, Golden

The carrier populations in the CB, VB, and IB can be expressed by the following rate equations (in the absence of external generation)

$$\frac{dn}{dt} = -\frac{n}{\tau_{CV}} - \frac{n}{\tau_{CI}} - \frac{n}{\tau_{SRH1}} \qquad 6.8.a.$$

$$\frac{dn_I}{dt} = \frac{n}{\tau_{CI}} - \frac{n_I}{\tau_{IV}} \qquad 6.8.b.$$

where n, p, and n_I are the electron density in the CB, hole density in the VB, and electron concentration in the oxygen states, respectively. Radiative recombination is assumed to be the dominant process for this analysis, with the exception of relaxation of carriers from CB to oxygen states. The carrier lifetimes for various transitions are given by the variables τ_{CV} (CB to VB), τ_{IV} (IB to VB) and τ_{CI} ((CB to IB) and may be expressed by

$$\tau_{CV} = \frac{1}{B_0(p_0 + n_0 + \Delta p)} \cong \frac{1}{B_0 p} \qquad 6.9.a.$$

$$\tau_{IV} = \frac{1}{B_1(p_0 + \Delta p)} \cong \frac{1}{B_1 p} \qquad 6.9.b.$$

$$\tau_{CI} = \frac{1}{v_{th}\sigma_n(N_I - n_I)} \qquad 6.9.c.$$

where B_0 is the radiative recombination coefficient for CB to VB transition in ZnTe, with a value of 7.1×10^{-10} cm^3/sec [120], B_1 is the radiative recombination coefficient extracted from the power dependent TPRL as shown in Figure 6.7(a). The electron and hole concentrations p_0 and n_0 are values under thermal equilibrium, where Δp is the injected hole concentration. The equilibrium electron concentration is neglected in the lifetime expressions due to p-type conductivity in all samples. The value of τ_{CI} is determined using the thermal velocity of electrons at room temperature v_{th} =2.6×10^7cm/s, concentration of oxygen atoms N_I inferred from absorption measurements, and assuming a capture cross section for electrons of σ_n =2×10^{-14} cm^2 [101]. The injected carrier density may be related to the TRPL excitation conditions assuming the the absorption coefficient for ZnTe at 3.1eV of approximately α=1.5×10^4cm^{-1} [121] and a uniform carrier distribution in the ZnTe layer.

The simulated decay time constants for electrons in the IB under varying excitation are shown in Figure 6.7(b) in good agreement with TRPL measurements. The effective carrier lifetime for electrons in the CB based on simulations of the above rate equations is also shown in Figure 6.7(b) for varying injection density, along with the lifetime of electrons in the IB. Based on these simulations, the effective carrier lifetime for CB electrons show the expected increase with increasing excitation density due to an increase in electron population in IB states. The carrier lifetime for IB electrons also show a corresponding decrease with injection density, though is still orders of magnitude higher than the lifetime for CB electrons. The dependence of lifetime for CB and IB electrons may be divided into three regions according to injection density relative to the background hole concentration (10^{15} cm^{-3}) and IB state density (10^{18} cm^{-3}). The effective lifetime of CB electrons may be extended to approximately 1 ns when the IB states are fully occupied, which would greatly improve the ability to extract carriers generated from a multi-photon process in an IBSC device.

Long carrier lifetime (>1μs) is measured for electrons in oxygen states in ZnTe, where lifetime shows an inverse proportionality with hole density. Shorter carrier lifetime is measured for IB states in p-doped ZnTe:NO and ZnTe:N material where hole population is significantly larger. Short lifetime is observed for electrons in the CB, and is attributed to the fast relaxation of carriers from the CB to IB. Rate equation analysis suggests that the effective lifetime of CB electrons also exhibits a dependence on injected carriers, where increase in lifetime is possible when injection is on the order of the IB state density. High injection conditions, such as would be present in solar concentrator cells, would serve to enhance the carrier lifetime for CB electrons and resulting conversion efficiency for intermediate band solar cells based on these materials. Therefore, the lifetime for electrons in intermediate band is approximately 1 μs, and the lifetime for electrons in conduction band is short and shown to be less than 100 ps. The increased injection is proposed as a way to alleviate the short carrier lifetime in the conduction band.

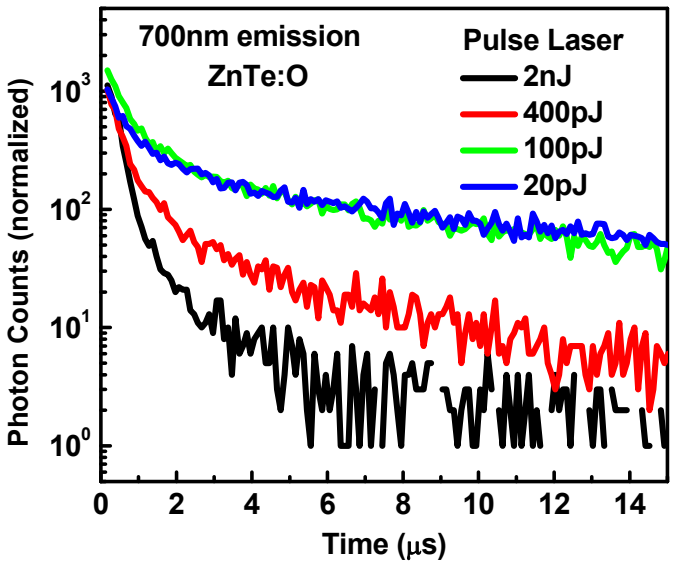

(a)

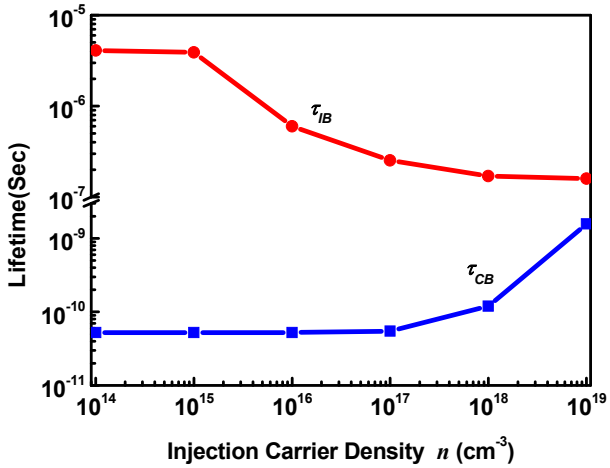

(b)

Figure 6.7 (a) Excitation-dependent time-resolved photoluminescence of ZnTe:O at 700nm and (b) Simulated effective carrier lifetime for electrons at the CB and IB for varying injection. Acknowledgement: Dr. Wyatt Metzger, National Renewable Energy Laboratory and Dr. Weiming Wang, the University of Michigan, Ann Arbor.

6.6 The Current Voltage Characteristic of *n*-GaAs:*p*-ZnTeO Diode

Prototype IBSC devices where fabricated incorporating a ZnTe:O absorber, the structure is illustrated in Figure 6.8, which consists of p^+-ZnTe emitter, p-ZnTe:O absorber, n^+ -GaAs, and n^+-GaAs substrate. The measured current-voltage characteristic is shown in Figure 6.8. The goal in this section is to plug in real material parameters as shown in Table 6-2 and spectral overlapping as evaluated in previous section, and calculate the realistic efficiency that is achievable by ZnTe/ZnTeO material system. Carrier transport and recombination model (CTR) presented in chapter 3 is employed here to calculate the *J-V* for *n*-GaAs/*p*-ZnTeO diode. The calculation in section 6.4 has shown that significant overlap in absorption spectrum is present in ZnTe:O. Notice that spectral overlap decreases efficiency significantly by detailed balance argument [60, 62]. In this scenario, the high energy photons are absorbed by low threshold processes and excess energy is dissipated as heat. Nonetheless, the measurement of spectral overlapping in absorption spectrum is somehow difficult, since experimentally α_{tot} is measured and it is very difficult to distinguish between different absorption mechanism that contribute to α_{tot}. With the analysis present in section 6.4, by utilizing several analytical expressions for localized states to continuum transition, and compared to experimental result, the spectral overlap between different absorption band is estimated and its effect is included in the *J-V* calculation in this section.

Table 6-2 Parameters for p-ZnTeO/n-GaAs diode current voltage characteristics

Band gap Energy E_G	2.3 eV
IB Energy position E_I	1.85 eV
m_C	$0.13m_0$
m_V	$0.6m_0$
IB density of states N_I	$1.0\text{x}10^{19}$ cm^{-3}
IB bandwidth σ_{IB}	0.05 eV
Refractive index n_r	2.7
Mobiltiy μ_n (ZnTe)	300 cm^2/Vs
Mobiltiy μ_p (ZnTe)	100 cm^2/Vs
Mobiltiy μ_n (ZnTeO)	150 cm^2/Vs
Mobiltiy μ_p (ZnTeO)	50 cm^2/Vs
τ_{CV}	1 ns
τ_{CI}	<100 ps
Basewidth W	1 μm
Emitter width W_p(ZnTe)	0.3 μm
Emitter width W_n(GaAs)	substrate
n_i (GaAs)	$2.1\text{x}10^6$ cm^{-3}
L_p (GaAs)	40 μm
D_p (GaAs)	10 cm^2/s

The expression for optical generation is slightly modified in order to take into account to take into account the spectral overlap in our absorption spectrum. The first order effect of spectral overlapping can be modeled by knowing the fact that the fraction of absorbed photons at certain frequency by a particular absorption mechanism, is proportional to the absorption coefficient of that absorption mechanism at that frequency [20, 27, 28, 60, 62]:

$$G_{XY} = \alpha_{XY} I_0 \exp^{-\alpha_{tot} x} \qquad \text{X, Y} = \text{I, V, C} \qquad \text{6.10.a.}$$

$$A_{XY} = \frac{\alpha_{XY}}{\alpha_{tot}} I_0 (1 - \exp^{-\alpha_{tot} W}) \qquad 6.10.b.$$
$$X, Y = I, V, C$$

α_{XY} is absorption coefficient, G_{XY} is generation rate and A_{XY} is absorbance. I, V, and C represent intermediate band (IB), valence band (VB), and conduction band (CB). W is base width, and I_0 is solar irradiance.

The optical generation expression in Eq.6.10.a and 6.10.b is then plugged into carrier transport and recombination model (CTR) in Chapter 3 with real material parameters as shown in Table 6-2, and the entire *J-V* can obtained. Figure 6.8 shows experimental and calculated *J-V* using parameters in Table 6-2.

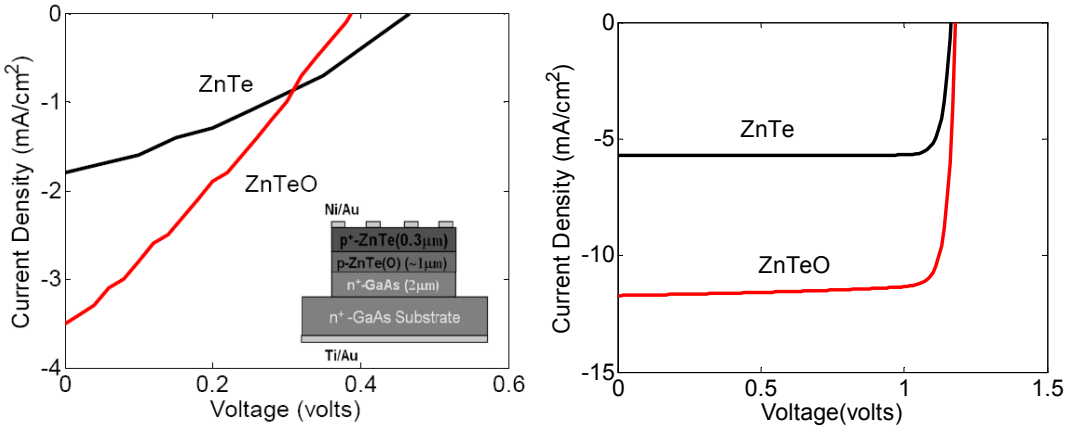

Figure 6.8 (Left) Experimental *J-V* for p-ZnTeO/n-GaAs diode and (right) calculated *J-V* for p-ZnTeO/n-GaAs diode. Acknowledgement: Dr. Weiming Wang, the University of Michigan, Ann Arbor.

Compared to theoretical calculation, the V_{oc} and J_{sc} of measured *J-V* curves are clearly smaller. The physical reason for V_{oc} reduction in experiemnt is still under investigation and is discussed below: GaAs n-emitter basically reduces the V_{oc} to 1.1 volts due to the minority carrier diffusion current. This is consistent with our calculated result. Larger open circuit voltage is expected if large bandgap material is used for n-emitter, such ZnSe. The band to band recombination (τ_{CV}), in ZnTe and ZnTeO is in the range of nano-second, which is not significant compared to minority carrier injection current and thus the V_{oc} should still be maintained > 1 volt. Nonetheless, the time-resolved photo luminescence data for τ_{CV} has not been very clear and further effort might

be made to clarify the physical reason of experimentally measured small V_{oc}. The V_{oc} reduction due to the recombination through oxygen states should not be very severe, due to the recombination current through intermediate sites is proportional to $\exp(V_A/2kT)$ or $\exp(V_A/nkT)$; however, the recombination through oxygen state can be detrimental to J_{sc} especially for the case of long basewidth compared to drift length. This is illustrated in Figure 6.9. Series resistance is on the order of 200 Ω–cm^2 for our devices, primarily resulting from the non-ideal electrode structure where the distance between interdigitated fingers is much larger than the carrier transport length and recombination occurs before carriers can be collected. Nonetheless, series resistance usually reduces J_{sc} and thus is unlikely the reason leading to V_{oc} reduction. From the above discussion, it is inferred that the potential reason for reduced V_{oc} is the interface trap states located at GaAs/ZnTeO interface. The trap charge affects electrostatic potential of the junction and thus the turn-on voltage of the diode, which in turn reduces V_{oc}. Using ZnSe may alleviate this problem since the lattice constant of ZnSe is closer to ZnTe compared to GaAs, as is important for reducing interface trap densities. The fact that calculated series J_{sc} is larger than measurement is mainly due to series resistance, which should be solved after electrode structure is optimized. The lack of box-shaped *J-V* in experimental data is also due to series resistance where the rectification behavior is not pronounced and linear ohmic behavior is observed. Since there are several potential reasons of degraded behavior and the precise physical reasons and parameters are not available, below the *J-V* of different lifetimes, series resistances, and shunt resistances are examined. The circuit model is lumped parameter model standard to solar cell equivalent circuit modeling. The *J-V* for varying lifetime calculation are based on CTR model. The *J-V* for varying series resistance and shunt resistance are superimposed on the calculated result in Figure 6.8. Figure 6.9 shows the effect of varying recombination lifetime.

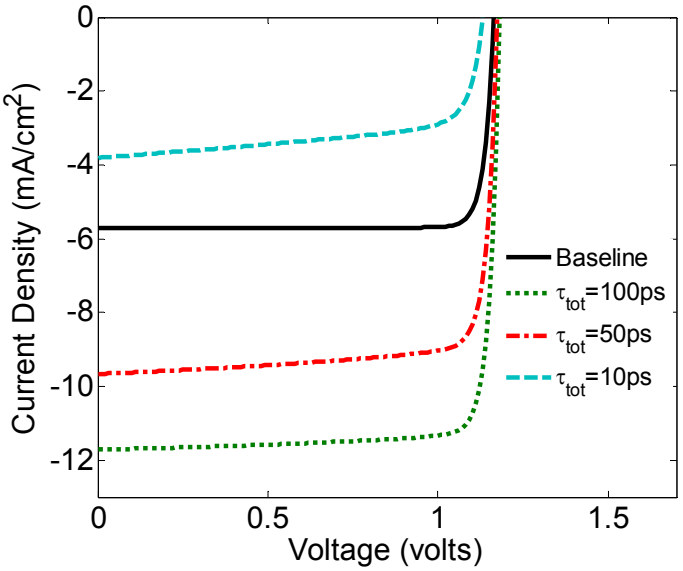

Figure 6.9 Calculated *J-V* for varying recombination lifetime

Figure 6.10 is the simulation of *J-V* including the effect of series and shunt resistance, and Figure 6.12 is simulation where series and shunt resistance is adjusted in order to fit experimental curve.

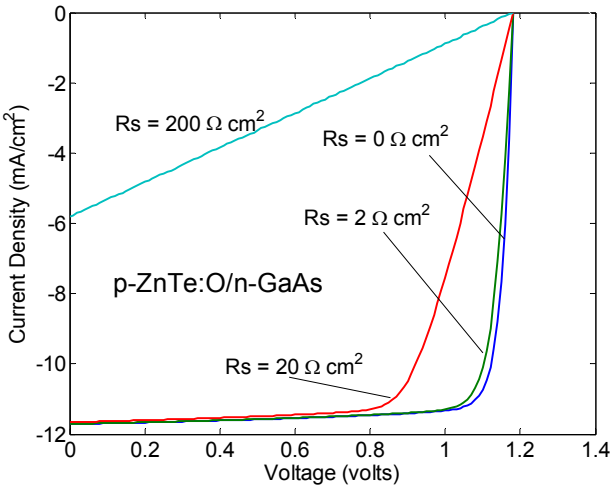

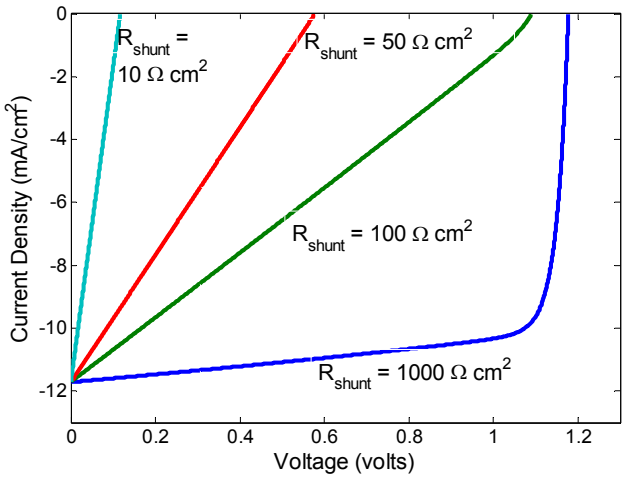

(b)

Figure 6.10 (a) ZnTe:O calculated *J-V* for varying series resistance and (b) varying shunt resistance

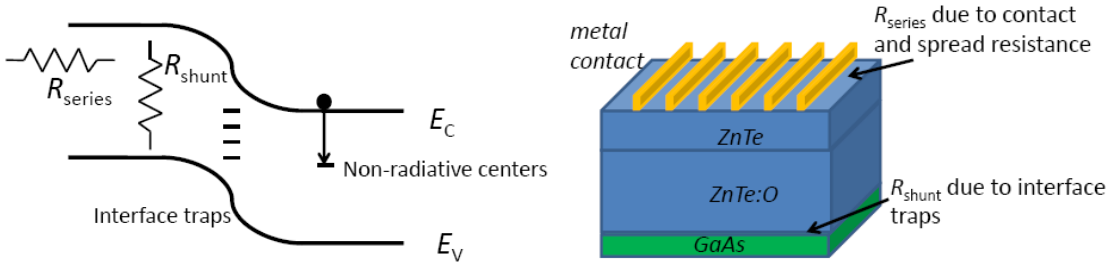

Figure 6.11 Illustrating the non-ideal properties of IBSC

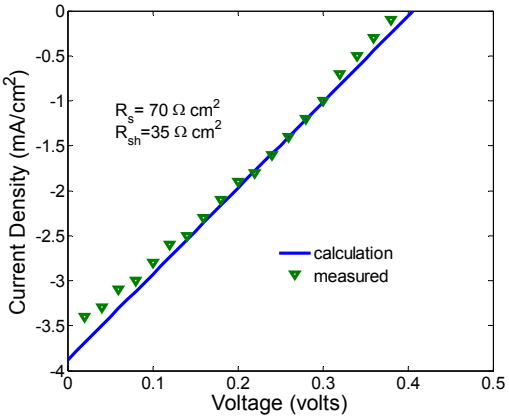

Figure 6.12 Calculated *J-V* with both series and shunt resistance and fit to experimental

data

6.7 Conclusion

Absorption coefficient for ZnTeO alloy is calculated based on Sundstrom et al. [107] and Lucovsky's model [109]. The calculated result is basically in agreement with experimentally measured data where incorporation of oxygen states introduces a peak in absorption spectrum below fundamental bandgap. Time resolved photoluminescence (TRPL) is measured and result shows the CB to IB lifetime depends on injection levels. Calculation based on rate equations analysis suggests the short lifetime from CB to IB might be suppressed by using solar concentrators. p-ZnTeO/n-GaAs *J-V* is then calculated using the absorption coefficient from previous section and the result indiciates the V_{oc} and J_{sc} achievable by ZnTe:O should be larger than currently measured in real devices. The reduction in V_{oc} might be attributed to excessive interface traps between ZnTeO and GaAs where electrostatic potential is affected by trap charges. From time-resolved photoluminescence measurement, it can be inferred that the incorporation of impurity atoms can lead to significant reduction in carrier lifetime in the materials, which is detrimental to the operation of photovoltaic cells. Thus, it is not surprising that the measured current voltage characteristics show small V_{oc} and J_{sc}. Nonetheless, from absorption measurement, it is also clear that in order to achieve noticeable improvement in subbandgap absorption, high concentration of impurity is desired. Therefore, the trade-off between optical absorption and recombination is important consideration as pointed out in our carrier transport and recombination model. In reality, whether the improvement can be made by subbandgap states thus greatly depends on the properties of the particular material such as optical absorption cross section and thermal capture cross section. Since these parameters are primarily determined by the material's bandstructure, a b initio study of intermediate band material is essential in order to find out the true potential of intermediate band photovoltaics.

Chapter VII Future Work

7.1 Intermediate Band Solar Cells

The future direction of intermediate band solar cell should focus on the experimental effort on high efficiency devices. The searching for new and more promising materials with significant subbandgap absorption, high mobility, and suppressed non-radiative processes is crucial for the success of intermediate band devices. This might include alloys and quantum confined structures. The theoretical and modeling effort should focus on explanation of the low efficiencies observed in real devices, revealing the underlying physical reasons, and provides feasible solutions to the problems. In addition, continued effort on theoretical work can predict/propose novel concepts to either exceed current efficiency limits or more practically, suggests new high efficiency cell structures where the gap between concept and experiment is smaller than IBSC.

7.2 Rigorously Coupled Wave Approach and Advanced Concepts in Light Trapping

7.2.1 Incidence with an Angle

Thus far, most studies of optical modeling of solar cells based on wave optics assume normal incidence in the simulation. Nonetheless, the oblique incidence as illustrated in Figure 7.1 is also of great importance as far as the design of solar cell structure is concerned since the sun light can come from any direction depending on the time during a day and latitude. Designing an incidence angle insensitive structure is certainly the goal and it can eliminate the need of expensive solar tracking system currently employed to increase cell efficiency. Nonetheless, before the development of novel structure robust to incidence angle, the effort has to be made in studying rigorous coupled wave analysis

(RCWA) [122-131] . RCWA is the electromagnetic numerical method most suitable for studying oblique incidence on 2-D or 3-D dielectric structure due to its semi-analytical and frequency domain analysis nature and the formulation inherently takes into account the incident and reflected waves propagating in different directions. It is also generally faster than finite difference time domain (FDTD) method and finite element method (FEM), though the limitation of RCWA is that it is more suitable for rectangular shaped structures.

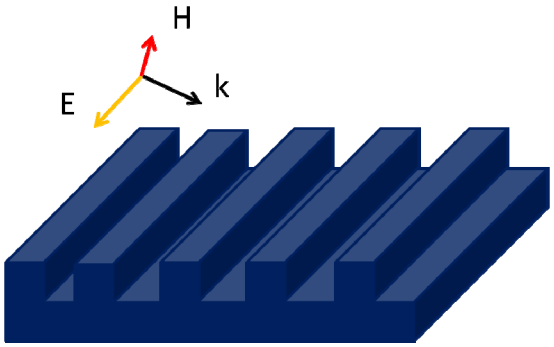

Figure 7.1 Illustration of oblique incidence on grating structures

7.2.2 Photonic Crystals and Air Holes Reflectors

Embedding air holes or nano-crystalline TiO_2 may modify the optical property of ZnO/metal back reflector by index contrasting and thus enhanced light scattering. In the case of photonic crystal, the altering of photonic density of state might increase the absorption or reflection properties at certain wavelengths. This can provide higher reflectivity. This helps increase the absorbance of long wavelength photons in the solar spectrum where light generally penetrates through the entire thin film and reaches back reflectors. The air holes and TiO_2 particles might also provide more scattering at the back side of the devices and thus are beneficial for achieving longer optical path length. The randomness in size and position of these nano-sized particles also benefits achieving truly randomized reflectors which are well-fitted for broad band solar spectrum application.

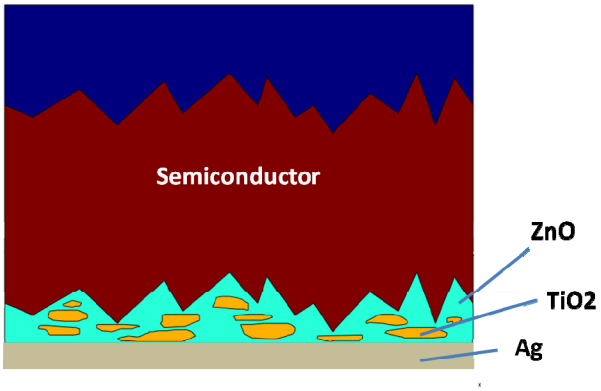

Figure 7.2 The structure of Ag/ZnO reflector with TiO_2 particles

7.2.3 Broad-Band Dielectric Mirror

The subwavelength gratings have been proved capable of realizing several different optical components including filters [132-135] and broad band dielectric mirrors[133, 136-141]. The physical origin of broad band flattop high reflectivity region in spectral response is referred to as guided mode resonance (GMR) where the incoming light is coupled to the leaky modes of the periodic grating structure. The broad band dielectric mirror based on subwavelength gratings (SWG) can potentially replace conventional metal back reflectors due to higher reflectivity. SWG can also be utilized to replace distributed Brag reflectors (DBR) in lasers, LED, detectors, and solar cells since DBR are in general too thick in dimension, especially for infrared application. Scaling the dimension of the SWG reflector structure can change or tune the wavelength of reflection band, which is promising for broad band application. Currently, the reflection band of SWG might not be wide enough for entire solar spectrum, although the target frequency range might be chosen for long wavelength portion of the spectrum where a back reflector is more crucial for complete absorption.

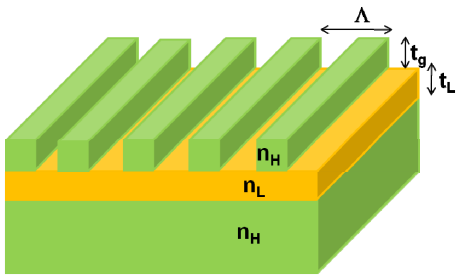

Figure 7.3 The structure of a broad band reflector

7.2.4 Controlled Resonance for Multi-Junction/Multi-Layer Cells

The broad band subwavelength gratings (SWG) reflector might be incorporated into multi-junction or multi-layer cells to further increase conversion efficiency as illustrated in Figure 7.4. The SWGs are inserted into the device structure, and the absorption materials that target at different wavelength are sandwiched between these mirrors. The different wavelength portions in incident solar spectrum are separated into different cells by SWG mirrors and thus all photons are absorbed by appropriate processes and thus thermalization is minimized. If properly designed, the efficiency can potentially exceed conventional tandem cell due to better light management. The SWG reflectors might form Fabry Perot cavity (FP). In this case, the absorbance can increase dramatically. The film thickness required for full absorption might also be reduced by this kind of structure due to better light trapping and resonance behavior, and this is beneficial for lower cost devices. The design and optimization of entire structure is the challenge since all of the dimension/material/device parameters affect each other and thus for the purpose of achieving ultra high efficiency device, significant effort has to be made in iterating in parameters or in understanding the underlying physics to reduce the iteration needed.

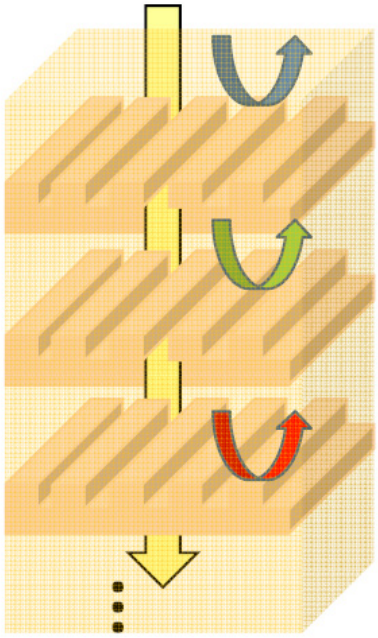

Figure 7.4 Multi-junction or multi-layer cells incorporating subwavelength gratings

Bibliography

[1] Schokley and Queisser, "Detailed balance limit of efficiency of p-n junction solar cell," *J. Appl. Phys.*, vol. 32, pp. 510-519, 1961.

[2] M. A. Green, "Third generation photovoltaics: Ultra-high conversion efficiency at low cost," *Progress in Photovoltaics*, vol. 9, pp. 123, 2000.

[3] R. R. King, D. C. Law, K. M. Edmondson, C. M. Fetzer, G. S. Kinsey, H. Yoon, R. A. Sherif, and N. H. Karam, "40% efficient metamorphic GaInP/GaInAs/Ge multijunction solar cells," *Appl Phys. Lett.*, vol. 90, pp. 183516-1-183546-3, 2007.

[4] M. A. Green, K. Emery, Y. Hishikawa, and W. Warta, "Solar Cell Efficiency Tables (Version 32)," *Prog. Photovolt. Res. Appl.*, vol. 16, pp. 435, 2008.

[5] A. Shah, P. Torres, R. T. arner, N. Wyrsch, and H. Keppner, "Photovoltaic technology: the case for thin-film solar cells," *Science*, vol. 285, pp. 692-698, 1999.

[6] M. A. Green, K. Emery, D. L. King, Y. Hishikawa, and W. Warta, "Solar cell efficiency tables (Version 29)," *Prog. Photovolt. Res. Appl.*, vol. 15, pp. 35 –40, 2007.

[7] H. Stiebig, N. Senoussaoui, C. Zahren, C. Haase, and J. M. r, "Silicon thin-film solar cells with rectangular-shaped grating couplers," *Prog. Photovolt. Res. Appl.*, vol. 14, pp. 13–24, 2006.

[8] J. Springer, A. Poruba, and M. Vanecek, "Improved three-dimensional optical model for thin-film silicon solar cells," *J. Appl. Phys*, vol. 2004, pp. 5329-5337, 2004.

[9] S. S. Hegedus and R. Kaplan, "Analysis of quantum efficiency and optical enhancement in amorphous Si p–i–n solar cells," *Prog. Photovolt. Res. Appl.* , vol. 10, pp. 257–269 2002.

[10] J. Krc, F. Smole, and M. Topic, "Potential of light trapping in microcrystalline silicon solar cells with textured substrates," *Prog. Photovolt. Res. Appl.*, vol. 11, pp. 429–436, 2003.

[11] H. Stiebig, M. Schulte, C. Zahren, C. H. e, B. Rech, and P. Lechner, "Light trapping in thin-film silicon solar cells by nano-textured interfaces," presented at SPIE, 2006.

[12] H. Sai, Y. Kanamori, K. o. Arafune, Y. Ohshita, and M. Yamaguchi, "Light trapping effect of submicron surface textures in crystalline Si Solar Cells," *Prog. Photovolt. Res. Appl.*, vol. 15, pp. 415–423, 2007.

[13] T. Brammer, W. Reetz, N. Senoussaoui, O. Vetterl, O. Kluth, B. Rech, H. Stiebig, and H. Wagner, "Optical properties of silicon-based thin-film solar cells in substrate and superstrate configuration," *Solar Energy Mater. Sol. Cells* vol. 74, pp. 469– 478, 2002.

[14] S.-S. Lo, C.-C. Chen, F. Garwe, and T. Pertch, "Broad-band anti-reflection coupler for a : Si thin-film solar cell," *J. Phys. D: Appl. Phys.* , vol. 40, pp. 754–758 2007.

[15] C. Haase and H. Stiebig, "Thin-film silicon solar cells with efficient periodic light trapping texture," *Appl. Phys. Lett.*, vol. 91, pp. 061116-1–061116-3, 2007.

[16] C. Haase and H. Stiebig, "Optical properties of thin-film silicon solar cells with grating couplers, design and fabrication of submicron grating structures for light trapping in silicon solar cells," *Prog. Photovolt. Res. Appl.* , vol. 14, pp. 629–641, 2006.

[17] M. R.H., Condensed Matter Theory Group, Paul-Scherrer-Institut, Ch-5232 Villigen, Switzerland 2002.

[18] M. T. Gale, B. J. Curtis, H. Kiess, and R. Morf, "Design and fabrication of submicron grating structures for light trapping in silicon solar cells," presented at Proceedings of SPIE, Conference on Optical Materials Technology for Energy Efficiency and Solar Energy Conversion IX, 1990.

[19] N. Senoussaoui, M. Krause, J. Muller, E. Bunte, T. Brammer, and H. Stiebig, "Thin-film solar cells with periodic grating coupler," *Thin Solid Films* vol. 451–452 pp. 397–401, 2004.

[20] A. Luque and A. Martı, "Increasing the Efficiency of Ideal Solar Cells by Photon Induced Transitions at Intermediate Levels," *Phys. Rev. Lett.*, vol. 78, pp. 5014, 1997.

[21] C. D. Cress, S. M. Hubbard, B. J. Landi, R. P. Raffaellea, and D. M. Wilt, "Quantum dot solar cell tolerance to alpha-particle irradiation," *Appl. Phys. Lett.*, vol. 91, pp. 183108, 2007.

[22] N. Usami, A. Amold, K. Fujiwara, K. Nakajima, T. Yokoyama, and Y. Shiraki, "1st IEEE International Conference on Group IV Photonics," Hong Kong, 2004.

[23] A. Luque, "Operation of the intermediate band solar cell under nonideal space charge region conditions and half filling of the intermediate band," *J. Appl. Phys.*, vol. 99, pp. 094503, 2006.

[24] R. Oshima, A. Takata, and Y. Okada, "Strain-compensated InAs/GaNAs quantum dots for use in high-efficiency solar cells," *Appl. Phys. Lett.*, vol. 93, pp. 083111, 2008.

[25] A. Alguno, N. Usami, T. Ujihara, K. Fujiwara, G. Sazaki, K. Nakajima, and Y. Shiraki, "Enhanced quantum efficiency of solar cells with self-assembled Ge dots stacked in multilayer structure," *Appl. Phys. Lett.*, vol. 83, pp. 1258-1260, 2003.

[26] A. J. Nozik, "Quantum dot solar cells," *Physica E*, vol. 14, pp. 115-120, 2002.

[27] M. Schmeits and A. A. Mani, "Impurity photovoltaic effect in c -Si solar cells. A numerical study," *J. Appl. Phys.*, vol. 85, pp. 2207-2212, 1999.

[28] M. J. Keevers and M. A. Green, "Efficiency improvements of silicon solar cells by the Impurity photovoltaic effect," *J. Appl. Phys.*, vol. 75, pp. 4022-4031, 1994.

[29] K. M. Y. W. Walukiewicz, J Wu, J. W. Ager III, W. Shan, M. A. Scrapulla , and O. D. Dubon, and P. Becla, "Mater. Res. Soc. Symp. ," presented at Mater. Res. Soc. Symp., San Francisco, 2005.

[30] J. W. A. III, W. Walukiewicz, and K. M. Yu, "Ultrahigh Efficiency Multiband Solar Cells Final Report for Director's Innovation Initiative Project," Lawrence Berkeley National Laboratory LBNL Report 59768, March 29 2006.

[31] S. Kurtz, S. W. Johnston, J. F. Geisz, D. J. Friedman, and A. J. Ptak, "Effect of Nitrogen Concentration on the Performance of $Ga_{1-x}In_xN_yAs_{1-y}$ Solar Cells," National Renewable Energy Laboratory, Golden, Colorado NREL/CP-520-37361, 2005.

[32] K. M. Yu, W. Walukiewicz, W. Shan, J. Wu, J. W. Beeman, M. A. Scarpulla, O. D. Dubon, and P. Becla, "Synthesis and optical properties of II-O-VI highly mismatched alloys," *J. Appl. Phys.*, vol. 95, pp. 6232-6238, 2004.

[33] K. M. Yu, W.Walukiewicz, J.Wu, W. Shan, J. W. Beeman, M. A. Scarpulla, O. D. Dubon, and P. Becla, "Diluted II-VI Oxide Semiconductors with Multiple Band Gaps," *Phys. Rev. Lett.*, vol. 91, pp. 246403-1-246403-4, 2003.

[34] J. Wu, W. Shan, and W. Walukiewicz, "Band anticrossing in highly mismatched III–V semiconductor alloys," *Semicond. Sci. Technol.*, vol. 17, pp. 860-869, 2002.

[35] O. Anton, D. Pate, C. S. Menoni, J.-Y. Yeh, L. Mawst, J. M. Pika, and N. Tansu, "Conference on Lasers and Electro-Optics," presented at Conference on Lasers and Electro-Optics, San Francisco, 2004.

[36] S. Kurtz, J. F. Geisz, B. M. Keyes, W. K. Metzger, D. J. Friedman, J. M. Olson, A. J. Ptak, R. King, and N. H. Karam, "Effect of growth rate and gallium source on GaAsN," *Appl. Phys. Lett.*, vol. 82, pp. 2634-2636, 2003.

[37] K. M. Yu, W. Walukiewicz, J. W. A. III, D. Bour, R. Farshchi, O. D. Dubon, S. X. Li, I. D. Sharp, and E. E. Haller, "Multiband GaNAsP quaternary alloys," *Appl. Phys. Lett.*, vol. 88, pp. 092110-1-092110-3, 2006.

[38] M. Smith, G. D. Chen, J. Y. Lin, H. X. Jiang, M. A. Khan, and Q. Chen, "Time-resolved photoluminescence studies of InGaN epilayers," *Appl. Phys. Lett.*, vol. 69, pp. 2837-2839, 1996.

[39] V. Shah, H. Schade, M. Vanecek, J. Meier, E. V.-S. ain, N.Wyrsch, U. Kroll, C. Droz, and J. Bailat, "Thin-film silicon solar cell technology," *Prog. Photovolt. Res. Appl.* , vol. 12, pp. 113–142 2004.

[40] S. J. Kang and Y. H. Joung, "Influence of substrate temperature on the optical and piezoelectric properties of ZnO thin films deposited by rf magnetron sputtering," *Appl. Surf. Sci.* , vol. 253, pp. 7330–7335, 2007.

[41] J. M. Khoshman and M. E. Kordesch, "Optical constants and band edge of amorphous zinc oxide thin films," *Thin Solid Films* vol. 515, pp. 7393–7399, 2007.

[42] A. S. Ferlauto, G. M. Ferreira, J. M. Pearce, C. R. Wronski, R. W. Collins, X. Deng, and G. Ganguly, "Analytical model for the optical functions of amorphous semiconductors and its applications for thin film solar cells," *Thin Solid Films* vol. 455 –456 pp. 388–392, 2004.

[43] C. AB, *Comsol Multiphysics RF Module User Guide V 3.3*, 2006.

[44] P. Bhattacharya, *Semiconductor Optoelectronic Devices, 2nd ed.* Upper Saddle River, NJ: Prentice-Hall, 2006.

[45] Synopsys, "Sentaurus Device EMW User Manual V. X-2005.10," 2005, pp. 78-79.

[46] W. Shockley and H. J. Queisser, "Detailed balance limit of efficiency of p-n junction solar cell," *J. Appl. Phys.* , vol. 32, pp. 510, 1961.

[47] C. Henry, "Limiting efficiencies of ideal single and multiple energy gap terrestrial solar cells " *J. Appl. Phys.* , vol. 51, pp. 4494, 1980.

[48] "ASTM G173-03, Standard Tables for Reference Solar Spectral Irradiances: Direct Normal and Hemispherical on 37 Degree Tilted Surface," ASTM International, West Conshohocken, PA 2005.

[49] A. Chipperfield, P. Fleming, H. Pohlheim, and C. Fonseca, *Genetic Algorithm Toolbox User Guide* Sheffield, UK: University of Sheffield, UK, 1994.

[50] S. Preblea, M. Lipson, and H. Lipson, "Two-dimensional photonic crystals designed by evolutionary algorithms," *Appl. Ph ys. Lett.*, vol. 86, pp. 061111-1-061111-3, 2005.
[51] B. Deken, S. Pekarek, and F. Dogan, "Minimization of field enhancement in multilayer capacitors," *Computational Mater. Sci.* , vol. 37, pp. 401–409, 2006.
[52] H. Lipson and J. B. Pollack, "Automatic design and manufacture of robotic lifeforms," *Nature*, vol. 406, pp. 974-977, 2000.
[53] L. Shen, Z. Ye, and S. He, "Design of two-dimensional photonic crystals with large absolute band gaps using a genetic algorithm," *Phy s. Rev. B*, vol. 68, pp. 035109-1-035109-5, 2003.
[54] C. Munuera, J. Zuniga-Perez, J. F. Rommeluere, V. Sallet, R. Triboulet, F. Soria, V. Munoz-Sanjose, and C. Ocal, "Morphology of ZnO grown by MOCVD on sapphire substrates," *J. Cryst. Growth*, vol. 264, pp. 70-78, 2004.
[55] J. M. Elson and J. M. Bennett, "Calculation of the power spectral density from surface profile data," *Appl. Optics*, vol. 34, pp. 201-208, 1995.
[56] *Matlab Signal Processing Toolbox User Guide* Natick, MA: The Mathworks, Inc., 2007.
[57] L. House, *Zygo Applicatoin Notes-MetroPro PSD Analysis*. Batford Mill: Lambda Photometrics Limited.
[58] G. Wei, K.-T. Shiu, N. C. Giebink, and S. R. Forrest, "Thermodynamic limits of quantum photovoltaic cell efficiency," *Appl. Phys. Lett.*, vol. 91, pp. 223507, 2007.
[59] A. Luque and A. Marti, "A Metallic Intermediate Band High Efficiency Solar Cell," *Prog. Photovolt. Res. Appl.*, vol. 9, pp. 73, 2001.
[60] T. S. Navruz and M. Saritas, "Efficiency variation of the intermediate band solar cell due to the overlap between absorption coefficients," *Solar Energy Materials & Solar Cells*, vol. 92, pp. 273, 2008.
[61] A. Martí, L. Cuadra, and A. Luque, "Quasi-Drift Diffusion Model for the Quantum Dot Intermediate Band Solar Cell," *IEEE Tran. Electron Dev.*, vol. 49, pp. 1632, 2002.
[62] L. Cuadra, A. Martí, and A. Luque, "Influence of the Overlap Between the Absorption Coefficients on the Efficiency of the Intermediate Band Solar Cell," *IEEE Tran. Electron Dev.*, vol. 51, pp. 1002, 2004.
[63] M. Leya, J. Boudaden, and Z. T. Kuznicki, "Thermodynamic efficiency of an intermediate band photovoltaic cell with low threshold Auger generation," *J. Appl. Phys.*, vol. 98, pp. 044905-1-044905-5, 2005.
[64] A. S. Brown and M. A. Green, "Intermediate band solar cell with many bands: Ideal performance," *J. Appl. Phys.*, vol. 94, pp. 6150-6158, 2003.
[65] A. Luque, A. Martı´, C. Stanley, N. Lo´pez, L. Cuadra, D. Zhou, J. L. Pearson, and A. McKee, "General equivalent circuit for intermediate band devices: Potentials, currents and electroluminescence," *J. Appl. Phys.*, vol. 96, pp. 903-909, 2004.
[66] A. Luque, A. MartíL, and L. Cuadra, "Thermodynamic Consistency of Sub-Bandgap Absorbing Solar Cell Proposals," *IEEE Tran. Electron Dev.*, vol. 49, pp. 2118-2124, 2001.

[67] A. Luque, A. Martí, and L. Cuadra, "Impact-Ionization-Assisted Intermediate Band Solar Cell," *IEEE Tran. Electron Dev.*, vol. 50, pp. 447-454, 2003.
[68] G. Wei and S. R. Forrest, "Intermediate-Band Solar Cells Employing Quantum Dots Embedded in an Energy Fence Barrier," *Nano Lett.*, vol. 7, pp. 218-222, 2007.
[69] K. Mukai, N. Ohtsuka, and M. Sugawara, "High photoluminescence efficiency of InGaAs/GaAs quantum dots self-formed by atomic layer epitaxy technique," *Appl. Phys. Lett.*, vol. 70, pp. 2416-2418, 1997.
[70] M. Sugawara, K. Mukai, and H. Shoji, "Effect of phonon bottleneck on quantum-dot laser performance," *Appl. Phys. Lett.*, vol. 71, pp. 2791-2793, 1997.
[71] A. D. Andreev and E. P. O'Reilley, "Optical transitions and radiative lifetime in GaN-AlN self-organized quantum dots," *Appl. Phys. Lett.*, vol. 79, pp. 521-523, 2007.
[72] S. Raymond, S. Fafard, P. J. Poole, A. Wojs, P. Hawrylak, S. Charbonneau, D. Leonard, R. Leon, P. M. Petroff, and J. L. Merz, "State filling and time-resolved photoluminescence of excited states in InxGa12xAs/GaAs self-assembled quantum dots," *Phys. Rev. Lett.*, vol. 54, pp. 11548-11554, 1996.
[73] V. Aroutiounian, S. Petrosyan, A. Khachatryan, and K. Touryan, "Quantum dot solar cells," *J. Appl. Phys.*, vol. 89, pp. 2268, 2001.
[74] A. J. Nozik, "Quantum Dot Solar Cells," National Renewable Energy Laboratory, Golden, Colorado NREL/CP-590-31011, 2001.
[75] O. Jania, I. Ferguson, C. Honsberg, and S. Kurtz, "Design and characterization of GaN/InGaN solar cells," *Appl. Phys. Lett.*, vol. 91, pp. 132117-1-132117-3, 2007.
[76] R. S. Candall, "Modeling of thin-film solar cell: Uniform field approximation," *J. Appl. Phys.*, vol. 54, pp. 7176, 1983.
[77] S. S. Hegedus, "Current Voltage Analysis of a-Si and a-SiGe Solar Cells Including Voltage-dependent Photocurrent Collection," *Prog. Photovolt. Res. Appl.*, vol. 5, pp. 151, 1997.
[78] T. Markvart and L. Castaner., *Solar cells: materials, manufacture and operation* Oxford, UK: Oxford: Elsevier Advanced Technology, 2005.
[79] W. Wang, A. Lin, and J. D. Phillips, "Electrical Characteristics and Photoresponse of ZnO/ZnTe Heterojunction Diodes," *J. Electon. Mater.*, vol. 37, pp. 1044, 2008.
[80] R. B. Laghumavarapu, A. Moscho, A. Khoshakhlagh, M. El-Emawy, L. F. Lester, and D. L. Huffakerb, "GaSb/GaAs type II quantum dot solar cells for enhanced infrared spectral response," *Appl. Phys. Lett.*, vol. 90, pp. 173125, 2007.
[81] A. S. Lin, W. Wang, and J. D. Phillips, "Model for intermediate band solar cells incorporating carrier transport and recombination and application to ZnTeO," *J. Appl. Phys.*, vol. 105, pp. 064512, 2009.
[82] A. Marti, N. Lopez, E. Antolín, E. Canovas, A. Luque, C. R. Stanley, C. D. Farmer, and P. Diaz, "Emitter degradation in quantum dot intermediate band solar cells," *Appl. Phys. Lett.*, vol. 90, pp. 233510, 2007.
[83] C. R. Stanley, "Intermediate-Band Solar Cells and the Quantum Dot Approach," Department of Electronics and Electrical Engineering, University of Glasgow,Glasgow, G12 8LT, U.K. 2004.

[84] A. S. Brown and M. A. Green, "Impurity photovoltaic effect: fundamental energy conversion efficiency limit," *J. Appl. Phys.*, vol. 92, pp. 1329-1336, 2002.
[85] M. Wolf, "Limitations and possibilities for Improvement of photovoltaic solar energy converters " *IEEE proc. IRE*, vol. 48, pp. 1246-1263, 1960.
[86] A. D. Vos, "Detailed balance limit of the efficiency of tandem solar cells," *J. Phys. D: Appl. Phys.*, vol. 13, pp. 839-846, 1980.
[87] A. S. Brown and M. A. Green, "Detailed balance limit for the series constrained two terminal tandem solar cell," *Physica E*, vol. 14, pp. 96-100, 2002.
[88] S. O. Ferreira, H. Sitter, W. Faschinger, and G. Brunthaler, "Growth of highly doped p-type ZnTe layers on GaAs using a nitrogen DC plasma cell," *J. Cryst. Growth*, vol. 140, pp. 282, 1994.
[89] C. M. Rouleau, D. H. Lowndes, J. W. McCamy, J. D. Budai, D. B. Poker, D. B. Geohegan, A. A. Puretzky, and S. Zhu, "Growth of highly doped p-type ZnTe films by pulsed laser ablation in molecular nitrogen," *Appl. Phys. Lett.*, vol. 67, pp. 2545, 1995.
[90] J. Han, T. S. Stavrinides, M. Kobayashi, R. L. Gunshor, M. M. Hagerott, and A. V. Nurmikko, "Heavy p-doping of ZnTe by molecular beam epitaxy using a nitrogen plasma source," *Appl. Phys. Lett.*, vol. 62, pp. 840, 1993.
[91] I. W. Tao, M. Jurkovic, and W. I. Wang, "Doping of ZnTe by molecular beam epitaxy," *Appl. Phys. Lett.*, vol. 64, pp. 1848, 1994.
[92] J. D. Dow, R.-D. Hong, S. Klemm, S. Y. Ren, M.-H. Tsai, O. F. Sankey, and R. V. Kasowski, "Proposed explanation of the p-type doping proclivity of ZnTe," *Phys. Rev. B*, vol. 43, pp. 4396, 1991.
[93] K. Akimoto, H.Okuyam, M. Ikeda, and Y. Mori, "Oxygen doping in CdTe, CdS and ZnS," *J. Cryst. Growth, 117, 420-423 (1992)*, vol. 117, pp. 420-423, 1992.
[94] J.J.Hopfield, D. G. Thomas, and R.T.Lynch, "Isoelectronic donors and acceptors," *Phys. Rev. Lett.*, vol. 17, pp. 312–315 1966.
[95] R. E. Deitz, D. G. Thomas, and J. J. Hopfield, ""Mirror" absorption and fluorescence in ZnTe," *Phys. Rev. Lett.*, vol. 8, pp. 391-393, 1962.
[96] J. D. Cuthbert, J. J. Hopfield, and D. G. Thomas, USA Patent 3413506 1966.
[97] Z. T. Kang, H. Menkara, B. K. Wagner, C. J. Summers, R. Durst, Y. Diawara, G. Mednikova, and T. Thorson, "Oxygen-doped ZnTe phosphors for synchrotron X-ray imaging detectors," *J. of Electron. Mater. 35, 1262 (2006).* vol. 35, pp. 1262, 2006.
[98] S. Merita, T. Kramer, B. Mogwitz, B. Franz, A. Polity, and B. K. Meyer, "Oxygen in sputter-deposited ZnTe thin films," *Phys. Status Solidi C*, vol. 3, pp. 960-963, 2006.
[99] Y. Nabetani, T. Okuno, K. Aoki, T. Kato, T. Matsumoto, and T. Hirai, "Epitaxial growth and optical investigations of ZnTeO alloys," *Phys. Status Solidi A*, vol. 203, pp. 2653, 2006.
[100] W. Wang, W. Bowen, S. Lin, S. Spanninga, and J. Phillips, "Optical characteristics of ZnTeO thin films synthesized by pulsed laser deposition and molecular beam epitaxy," *J. Electon. Mater.*, vol. 38, pp. 119, 2009.
[101] J. D. Cuthbert and D. G. Thomas, "Fluorescent decay times of excitons bound to isoelectronic traps in GaP and ZnTe," *Physical Review*, vol. 154, pp. 764-771, 1967.

[102] K. Sato and S. Adachi, "Optical properties of ZnTe," *J. Appl. Phys.*, vol. 73, pp. 926-931, 1993.
[103] R. Markowski and M. Podgorny, "Calculated optical properties of zincblende semiconductors ZnTe, CdTe and HgTe," *J. Phys.: Condens. Matter*, vol. 4, pp. 2505-2515, 1992.
[104] Y. Zhang, B. J. Skromme, and F. S. Turco-Sandroff, "Effects of thermal strain on the optical properties of heteroepitaxial ZnTe," *Phys. Rev. B*, vol. 46, pp. 3872-3885, 1992.
[105] B. Kotlyarchuk and V. Savchuk, "Investigation of ZnTe thin films grown by Pulsed Laser Deposition method," *phys. stat. sol. (b)*, vol. 244, pp. 1714–1719, 2007.
[106] A. E. Rakhshani, "Characterization of ZnTe films electrodeposited from aqueous solution containing NaOH," *Semicond. Sci. Technol.*, vol. 19, pp. 543–547, 2004.
[107] B. O. Sundstrom, L. Huldt, and N. G. Nilsson, "Electron capture coefficient of neutral indium and pair recombination in compensated silicon," *J. Phys. C: Solid State Phys.*, vol. 15, pp. 3359-3370, 1982.
[108] W. Schelteri, W. Hell, R. Helbig, and M. Schulz, "Optical properties of indium-doped silicon reinspected," *J. Phys. C: Solid State Phys.*, vol. 15, pp. 5839-5850, 1982.
[109] G. Lucovsky, "On the photoionization of deep impurity centers in semiconductors," *Solid State Communications*, vol. 3, pp. 299-302, 1965.
[110] D. M. Eagles, "Optical absorption and recombination radiation in semiconductors due to transitions between hydrogen-like acceptor impurity levels and the conduction band," *J. Phys. Ckem. Solids*, vol. 16, pp. 76-83, 1960.
[111] R. Passler, "Photoionization cross-section analysis for a deep trap contributing to current collapse in GaN field-effect transistors," *J. Appl. Phys.*, vol. 96, pp. 715-722, 2004.
[112] W. P. Dumke, "Optical transitions involving impurities in semiconductors," *Physical Review*, vol. 132, pp. 1998-2002, 1963.
[113] A. H. Edwards and W. B. Fowler, "Photoionization of group-III acceptors in silicon," *Physical Review B*, vol. 16, pp. 3613-3617, 1977.
[114] D. L. Dexter, "Solid State Physics," in *Solid State Physics*, vol. 6, D. L. .Dexter, Ed. New York: Academic Press, 1958.
[115] E. Finkman and S. E. Schacham, "The exponential optical absorption babd tail of Hg1-xCdxTe," *J. Appl. Phys.*, vol. 56, pp. 2896-2900, 1984.
[116] W. Wang, A. Lin, J. D. Phillips, and W. K. Metzger, "Generation and recombination rates at ZnTe:O intermediate band states," *Appl Phys. Lett.*, vol. 95, pp. 261107-1-261107-3, 2009.
[117] W. Wang, A. S. Lin, and J. D. Phillips, "Intermediate-band photovoltaic solar cell based on ZnTe:O," *Appl Phys. Lett.*, vol. 95, pp. 011103-1-011103-3, 2009.
[118] N. Amin, K. Sopian, and M. Konagai, "Numerical modeling of CdS/CdTe and CdS/CdTe/ZnTe solar cells as a function of CdTe thickness," *Sol. Ener. Mater. Sol. Cell*, vol. 91, pp. 1202-1208, 2007.
[119] D. T. F. Marple, "Refractive index of ZnSe, ZnTe, and CdTe," *J. Appl. Phys.*, vol. 35, pp. 539-542, 1964.

[120] D. Z. Garbuzov, "Reradiation effects, lifetimes and probabilities of band-to-band transitions in direct A3B5 compounds of GaAs type," *J. Luminescence*, vol. 27, pp. 109, 1982.
[121] W. Wang, A. Lin, and J. Phillips, "Electronic Materials Conference," presented at Electronic Materials Conference, Santa Barbara, 2008.
[122] R. R. Aggrawal, "Diffraction of light by ultrasonic waves," *Proc. Indian Acad. Sci.*, vol. 31, pp. 417-426, 1950.
[123] P. Phariseau, "On the diffraction of light by progressive supersonic waves," *Proc. Indian Acad. Sci. Sect. A*, vol. 44, pp. 165-170, 1965.
[124] W. R. Klein and B. D. Cook, "Unified approach to ultrasonic light diffraction," *IEEE Trans. Sonic Ultrason.*, vol. 14, pp. 123-134, 1967.
[125] H. Kogelnik, "Coupled wave theory for thick hologram gratings," *Bell Syst. Tech. J.*, vol. 48, pp. 1909-1947, 1969.
[126] G. L. Fillmore and R. F. Tynan, "Sensitometric characteristics of hardened dichromated-gelatin films," *J. Opt. Soc. Am.*, vol. 61, pp. 199-203, 1971.
[127] J. A. Kong, "Second-order coupled-mode equations for spatially periodic media," *J. Opt. Soc. Am.*, vol. 67, pp. 825-829, 1977.
[128] R. Magnusson and T. K. Gaylord, "Analysis of multiwave diffraction by thick gratings," *J. Opt. Soc. Am.*, vol. 67, pp. 1165-1170, 1977.
[129] M. G. Moharam and T. K. Gaylord, "Rigorous coupled-wave analysis of planar-grating diffraction," *J. Opt. Soc. Am.*, vol. 71, pp. 811-818, 1981.
[130] M. G. Moharam and T. K. Gaylord, "Rigorous coupled-wave analysis of metallic surface-relief gratings," *J. Opt. Soc. Am. A*, vol. 3, pp. 1780-1787, 1986.
[131] M. Yang and S. Stavrou, "Rigorous coupled-wave analysis of radio wave propagation through periodic building structures," *IEEE Antennas and wireless propagation letter*, vol. 3, pp. 204-207, 2004.
[132] X. M. Zhang, Q. W. Zhao, T. Zhong, A. B. Yu, E. H. Khoo, C. Lu, and A. Q. Liu, "Variable nano-grating for tunable filters," presented at The 14th International Conference on Solid-State Sensors, Actuators and Microsystems, Lyon, France, 2007.
[133] Y. Ding and R. Magnusson, "Resonant leaky-mode spectral-band engineering and device applications," *Optics Express*, vol. 12, pp. 5661-5674, 2004.
[134] S. Tibuleac and R. Magnusson, "Narrow-linewidth bandpass filters with diffractive thin-film layers," *Optics Lett.*, vol. 26, pp. 584-586, 2001.
[135] Z. S. Liu, S. Tibuleac, D. Shin, P. P. Young, and R. Magnusson, "High-efficiency guided-mode resonance filter," *Optics Lett.*, vol. 23, pp. 1556-1558, 1998.
[136] C. F. R. Mateus, M. C. Y. Huang, Yunfei Deng, A. R. Neureuther, and C. J. Chang-Hasnain, "Ultrabroadband mirror using low-index cladded subwavelength grating," *IEEE Photon. Tech. Lett.*, vol. 16, pp. 518-520, 2004.
[137] S. Boutami, B. B. Bakir, H. Hattori, X. Letartre, J.-L. Leclercq, P. Rojo-Romeo, M. Garrigues, C. Seassal, and P. Viktorovitch, "Broadband and compact 2-D photonic crystal reflectors with controllable polarization dependence," *IEEE Photon. Tech. Lett.*, vol. 18, pp. 835-837, 2006.
[138] M. C. Y. Huang, Y. Zhou, and C. J. Chang-Hasnain, "A surface-emitting laser incorporating ahigh-index-contrast subwavelength grating," *Nature Photonics*, vol. 1, pp. 119-122, 2007.

[139] M. C. Y. Huang, Y. Zhou, and C. J. Chang-Hasnain, "A nanoelectromechanical tunable laser," *Nature Photonics*, vol. 2, pp. 180-184, 2008.
[140] R. Magnusson and M. Shokooh-Saremi, "Physical basis for wideband resonant reflectors," *Optics Express*, vol. 16, pp. 2456-3462, 2008.
[141] R. G. Mote, S. F. Yu, W. Zhou, and X. F. Li, "Design and analysis of two-dimensional high index-contrast grating surface-emitting lasers," *Optics Express*, vol. 17, pp. 260-265, 2009.